

NOVEL DEVICE AND METHODS
FOR COMPOSITE MATERIAL
CHARACTERIZATION

by

MICHAEL M. TADROS

Presented to the Faculty of the Graduate School of
The University of Texas at Arlington in Partial Fulfillment
of the Requirements
for the Degree of

DOCTOR OF PHILOSOPHY

THE UNIVERSITY OF TEXAS AT ARLINGTON

May 2015

Copyright © by Michael Tadros 2015

All Rights Reserved



Acknowledgements

First, I would like to thank God for helping me through all the challenges I faced during my time at UTA. I know I could have not made it through without his grace. Thanks also to Fr. Abraam Farah for his wise spiritual and professional guidance.

I would like to acknowledge my committee members. Special thanks go to Dr. Kent Lawrence, Dr. Robert woods, Dr. Seiichi Nomura and Dr. Wen Chan. Professors, you set an unparalleled example for how wise, patient, professional, competent and supportive a professor should be to a student. You are all true role models in your own rights, and working with some of you outside the scope of my PHD has been one of the most enriching experiences in my life. I know I would have not made it through this program without your sound advices and selfless support. Thank you!

I would also like to thank everyone at AMSL lab that supported this work. Mr. Brian Shonkwiler, Dr. Yuri Nikishkov and Dr. Guillaume Seon, thank you all for your experimental and technical support. Also, special thanks go to my colleague and office mate, Ms. Ekaterina Bostaph for her unwavering support over the years. Also, Julia, Sarvenaz, Bastiaan and Md, thanks for the companionship, encouragement and all the interesting and amusing conversations.

I would also like to acknowledge my friends, Mikhail Titov, Gustavo Puerto and Lauren Lindsay. You all are true friends for being there for me in my time of need.

And last, but definitely not least, I would like to thank my family. I would have not achieved anything in my life if it was not for the years of sacrifices and unwavering support from my parents, Samra Philobos and Monir Tadros. And growing up with a patient and wise brother like Mina Tadros, allowed me to have the exceptional support system that is our family.

April 7, 2015

Abstract

NOVEL DEVICE AND METHODS
FOR COMPOSITE MATERIAL
CHARACTERIZATION

Michael Tadros, PhD

The University of Texas at Arlington, 2015

Supervising Professor: Andrew Makeev

Composite materials have several advantages over metallic materials, with their high specific strength and ability to be elastically tailored to create advantageous structural responses. However, the widespread implementation of composite materials in primary structures is limited by our knowledge of how damage mechanisms interact and spread inside composite parts. To date, characterization has been conducted using one of two methods, surface measurements and subsurface measurements. Surface measurements cannot in general capture the failure of multidirectional composite laminates. Subsurface measurements allow for observations of the internal material structure and damage mechanisms inside the composite which might facilitate greater understanding of the multiple failure modes and their interactions inside composite structure especially for aerospace applications.

X-ray computed tomography allows for the investigation of subsurface damage in composite materials by generating a three dimensional representation of the scanned structure. However, as nondestructive measurements using x-rays are based on the density contrast, e.g. small opening of the crack surfaces, the damage might become undetectable if the crack surfaces are closed. Mechanical loading of the composite

structure while x-raying can open otherwise hidden damage and reveal the topology essential for understanding failure modes in composite materials and structures.

In this work, we have developed a system that allows for mechanical testing of realistic-size specimens including those used in the ASTM standards for measuring mechanical properties of composites, while performing in-situ x-ray computed tomography. We will demonstrate the advantages of this system over no-load CT, and over other, similar systems. The new system improves correlation with structural failure prediction models based on finite element analysis [1]. We then used this new system, along with newly developed fixtures to monitor and characterize delamination growth in Double Cantilever Beam specimens (DCB). It is worth noting that delamination is one of the principal failure modes in composites.

Newly developed finite element numerical models that result in improved accuracy in the calculation of the critical strain energy release rates will be presented along with a new method of meshing orthogonal crack front elements for crack fronts that intersect a free surface.

Several DCB tests are conducted, tens of CT scans are performed, and hundreds of finite element models are created and processed in order to characterize, validate and investigate crack growth in DCB specimens. As observed by other researches, crack growth in DCB specimens is curved, and using our models, we show that there is significant difference in the values and distribution of Strain Energy Release Rate (SERR) values across the specimen width between the straight (assumed) crack front and the curved (observed) one.

Table of Contents

Acknowledgements	iii
Abstract	iv
List of Illustrations	ix
List of Tables	xiv
Chapter 1 Outline	1
Chapter 2 Background	3
Non Destructive Testing	3
Micro X-ray Computed Tomography (CT)	4
Micro X-ray CT Considerations	7
Tests for Fracture Toughness	12
Calculation of Fracture Toughness	16
Double Cantilever Beam Test.....	17
The modified Beam Theory	18
Compliance Calibration (CC) Method	20
Critical Strain Energy Release Rate (G_{Ic}).....	21
Fracture Toughness Calculation in FEA.....	22
Virtual Crack Closure Technique (VCCT)	22
J Contour Integral	29
Chapter 3 Literature Survery.....	31
In-situ Experiments with X-ray.....	31
Limitations of Current In-Situ Devices	39
Double Cantilever Beam Testing.....	41
Chapter 4 In-situ X-ray System.....	46
System Design.....	46

System Configurations.....	52
Chapter 5 Validation of Current Models.....	59
Damage Observation.....	59
Validation of Numerical Models	64
Prediction of Damage in OHC Specimens	64
Investigation of Mode-mixity in OHT Specimens	69
Chapter 6 DCB : Part I Mechanical Testing.....	71
Outline	71
Horizontal DCB.....	71
Vertical DCB	75
Test Procedure	78
CT scan Technique	80
Analytical Results	88
Chapter 7 DCB : Part II FEM Modeling.....	90
Horizontal DCB.....	90
Model Mesh	96
Mesh Convergence	96
Mesh across specimen width	101
Verification	104
Effect of accounting for material non-linear Behavior.....	107
FEM Data Reduction	110
Horizontal FEM Model Results	113
Vertical Finite Element Model.....	115
Model Parts and Geometry	117
Loading.....	117

Mesh	118
Curved Crack fronts	118
Straight vs Curved Crack Fronts	128
Chapter 8 Conclusions and Recommendations for Future Work	134
Conclusion	134
Recommendations for Future Work.....	136
In-situ system	136
Vertical DCB fixture	137
FEM models	137
References.....	138
Biographical Information	146

List of Illustrations

Figure 2-1 Sequence of magnified X-ray images of a composite honeycomb [2]	4
Figure 2-2 (a) Fan beam (b) Cone-beam (c) Parallel beam [4]	5
Figure 2-3 X-ray Tomography [9]	6
Figure 2-4 Northstar X-5000 micro CT x-ray tomograph	7
Figure 2-5 X-ray reflection tube [11]	7
Figure 2-6 Inverse Square Attenuation [12]	8
Figure 2-7 Geometric Magnification and Un-sharpness [14]	9
Figure 2-8 Fiber Breaking	10
Figure 2-9 Matrix Cracks	11
Figure 2-10 Delamination	11
Figure 2-11 Different fracture modes	12
Figure 2-12 Double Cantilever Beam Test (DCB), Mode I	13
Figure 2-13 End Notch Flexure, Mode II	13
Figure 2-14 Split Cantilever Beam Test, Mode III	14
Figure 2-15 Edge Crack Torsion (ECT) test, Mode III	14
Figure 2-16 The Arcan test fixture [18]	15
Figure 2-17 Fiber bridging in fiberglass DCB test	15
Figure 2-18 DCB specimen with piano hinges	17
Figure 2-19 DCB specimen loading	18
Figure 2-20 MBT correction factor	20
Figure 2-21 Compliance Calibration slope	21
Figure 2-22 R-curve showing the NL, VIS and 5% points	22
Figure 2-23 VCCT for 8 noded brick element [23]	24

Figure 2-24 VCCT for corner node in a 20 noded element - 3D [23].....	25
Figure 2-25 VCCT for corner node in a 20 noded element - 2D [23].....	26
Figure 2-26 Rotation of forces and displacements for curved cracks [25].....	27
Figure 2-27 Nodal forces using spring elements	28
Figure 2-28 Nodal forces from element contribution.....	29
Figure 2-29 J integral Contour	29
Figure 3-1 Device by Breunig et al a) Schematic and (b) photograph [27].....	31
Figure 3-2 C-scan of ENF failure between angle plies [67]	42
Figure 3-3 curved crack front I DCB specimen after fatigue failure [65]......	42
Figure 4-1 Computer representation, and a picture of the in-situ system.....	46
Figure 4-2 Conceptual drawing for the proposed device [78]	47
Figure 4-3 FEM analysis showing maximum deflection of the Load Cell attachment	50
Figure 4-4 FEM analysis showing maximum deflection of the Top grip attachment	51
Figure 4-5 Aligning the bottom adapter using the dial indicator	53
Figure 4-6 Using a steel rod to align the top and bottom drives	53
Figure 4-7 Torque fluctuations as the machine rotates, specimen I.....	54
Figure 4-8 Torque fluctuations as the machine rotates, specimen II.....	55
Figure 4-9 Torque fluctuations as the machine rotates, specimen I.....	55
Figure 4-10 Torque fluctuations as the machine rotates, specimen II.....	55
Figure 4-11 Illustration of calibration specimen.	56
Figure 4-12 Test machine misalignment types, showing the concentric misalignment and the angular misalignment between machine fixtures [83]......	57
Figure 4-13 Normalized percent bending during a full rotation.....	58
Figure 5-1 Left: no load. Right: 4500 lb tensile load.	60

Figure 5-2 Top: no load showing little damage. Bottom: 4500 lb tensile load showing several matrix cracks.	61
Figure 5-3 Top: no load. Bottom: 4500 lb tensile load showing matrix cracks and fiber breaks.....	62
Figure 5-4 Left: specimen under 4700 lbf, crack opening is 20 μm ; Right: specimen under 6520 lbf, crack opening is 44 μm	63
Figure 5-5 Left: specimen under 4700 lbf, crack opening is 16 μm ; Right: specimen under 6520 lbf, crack opening is 25 μm	64
Figure 5-6 Development of matrix cracks (dark grey) and delaminations (lighter grey) in OHC first sub-surface 45° ply [1].....	65
Figure 5-7 FEM model of an open hole tension specimen	69
Figure 5-8 GI, GII and GIII for one of the crack fronts in OHT specimen at 660 lb load ..	70
Figure 6-1 DCB specimen with piano hinge.....	72
Figure 6-2 DCB specimen Picture and dimensions	73
Figure 6-3 DCB Specimen Loading	73
Figure 6-4 R-curve showing the NL, VIS and 5% points [22]	74
Figure 6-5 Average Fracture Toughness values for S2/E773 Glass-epoxy Composite ...	75
Figure 6-6 Fixture for vertical DCB	76
Figure 6-7 Vertical DCB Force Analysis	77
Figure 6-8 FEM of Combined loading vs normal forces for one of the crack increments.	78
Figure 6-9 Example of measuring specimen deformation using DIC camera and computer software.....	79
Figure 6-10 CT reconstructed volume	82
Figure 6-11 Crack front identification from CT reconstructed volume	83
Figure 6-12 Crack front error sensitivity	85

Figure 6-13 Different crack front measurement technique	86
Figure 6-14 RANSAC curve fit	87
Figure 6-15 RANSAC curve fit for a 5mm crack length	88
Figure 6-16 Comparison between horizontal DCB and Vertical DCB	89
Figure 7-1 FEM DCB model.....	91
Figure 7-2 Collapsed mesh.....	92
Figure 7-3 Top view of elements below crack front and crack front nodes	92
Figure 7-4 Model showing merged nodes.....	94
Figure 7-5 Nodes not merged	95
Figure 7-6 Sample output for orphan mesh, merged model.	95
Figure 7-7 FEM DCB model.....	97
Figure 7-8 Mesh convergence for region I	98
Figure 7-9 Mesh convergence for region II	98
Figure 7-10 Mesh convergence for region III	99
Figure 7-11 Mesh convergence for region IIII	99
Figure 7-12 Mesh convergence for Specimen Thickness.....	100
Figure 7-13 Mesh convergence for Specimen width	100
Figure 7-14 Uniform mesh size across the specimen width	102
Figure 7-15 Mesh with refined bands at the edges.....	103
Figure 7-16 Mesh with linearly variable mesh size across the width.....	104
Figure 7-17 Comparison between J-contour values for the different element types.	107
Figure 7-18 Close-up showing Node Set for Contour #7 in red.....	109
Figure 7-19 VCCT vs J-integral Contours.....	109
Figure 7-20 SERR across specimen width	110
Figure 7-21 Normalized SERR vs Normalized width for different specimen widths.....	111

Figure 7-22 Comparison between FEM and Experimental results	113
Figure 7-23 percent error between FEM and CC	115
Figure 7-24 Vertical FEM model, straight crack front.	116
Figure 7-25 Vertical FEM model, curved crack front.	116
Figure 7-26 Forces and displacements for Orthogonal mesh around crack front [23] ...	120
Figure 7-27 Length-wise morphing process.....	121
Figure 7-28 Orthogonal morphing using a 20 th order polynomial	123
Figure 7-29 Close-up on the morphed elements close to the specimen edge	124
Figure 7-30 Polynomial decay function for orthogonal mesh.....	125
Figure 7-31 SERR for a curved crack front using different levels of orthogonality	126
Figure 7-32 Comparison between (a) morphed mesh with 6 th order polynomial, and (b) morphed mesh with 20 th order polynomial	127
Figure 7-33 Orthogonalized Mesh vs Smith and Raju Method for pre-crack region	128
Figure 7-34 The effect of the curved crack front on the SERR distribution across the specimen width for a 5mm crack length.....	129
Figure 7-35 Strain energy across specimen width for straight (N=0) and curved crack front (N=1.5) by Budzik et al [68]	131

List of Tables

Table 3-1 Current Implementations of In-situ Devices.....	38
Table 5-1 FE-based simulation of matrix cracks and fiber failure developments in OHC specimens [1].....	66
Table 5-2 Comparison between predicted failure in a 12 ply composite laminate, and scans conducted under load [1].	68
Table 7-1 S2-E773 Material Properties [85].....	90
Table 7-2 Mesh Convergence Results.....	101
Table 7-3 Isotropic Material Properties	105
Table 7-4 Verification Model Parameters.....	105
Table 7-5 FEM Element Selection	106
Table 7-6 Dc factor values for different materials	112
Table 7-7 Vertical FEM Rollers Mesh	118
Table 7-8 Sample CT scans and FEA results.....	132

Chapter 1

Outline

This work is structured as follows. *Chapter 2* includes relevant background information that will be built upon in the following sections. It explains why we use *Non Destructive Testing*, and it demonstrates the advantages of *Micro X-ray Computed Tomography (CT)* used in this work. There are several considerations specific to micro x-ray CT that need to be addressed; these will be discussed in the “*Micro X-ray CT Considerations*” section. Then we discuss *Fractures in Composite Materials*. Showcasing current test methods and data reduction techniques used to characterize fractures in composite materials. We will then cover the background necessary to calculate SERR in FEA numerical models using the Virtual Crack Closure Technique and the J contour integral.

Chapter 3 is a comprehensive literature survey of existing in-situ devices and attempts. In the second section of the chapter, the *Limitations of Current In-Situ Devices* are discussed and a basic statistical comparison of all researched attempts is conducted. The state of art of DCB testing is then presented, showing the current state of art in modeling DCB specimens.

Chapter 4 presents the design of the in-situ system designed and built at AMSL at UTA. It discusses the design process, the different components and configurations of the device. Then it lists the different improvements made to the design and how it affects the overall performance.

Chapter 5 investigates the usefulness of the new system by demonstrating the detection of hard-to-detect failures, as well as using it to monitor failure progression in carbon-epoxy open-hole-compression laminates. The system is also used to validate

newly developed numerical model that predicts failure and fatigue life of composite laminates [1].

Chapter 6 explains the experimental test method used to conduct both the horizontal and vertical DCB tests. The X-ray CT technique and the methodology used to identify and measure the crack front from the reconstructed volume is also explained.

Chapter 7 presents the FEA numerical models created for this work. The models for the horizontal and vertical DCB tests are presented explaining the selection process of the different modeling techniques, element types and material properties. Then the results are shown comparing them to those obtained from the experiments.

Chapter 8 takes stock of all the work presented so far, then presents recommendations for future work. As well as future uses to further expand this research.

Chapter 2

Background

Non Destructive Testing

Non-destructive testing (NDT) and non-destructive evaluation (NDE) techniques are preferred over destructive ones for defect detection, as well as structural health monitoring [2]. Many NDT techniques used nowadays for composite materials were originally adapted from ones developed for metals, or medical testing [3]. And while some were convenient enough for use with composites, others had to be introduced to make them more suitable for composite materials testing. Few of the NDT practices used nowadays are; Ultrasonic, Ultrasonic backscatter, acoustic emission, tap test, 2D x-ray, thermography, eddy current, microwaves and low-frequency vibration. Some advanced techniques are x-ray tomography, laser ultrasonic, holography, vibrothermography, D-sight, neutron radiography and synchrotron x-ray. Unfortunately, there are limited methods to monitor sub-ply crack onset and progression under load. Currently most NDT techniques that are aimed at studying composite failure are performed after damage has already occurred, and loads have been removed. But a lot can be learnt, by using analysis that closely resembles real-life composite failures and defects, which entails testing the composite part while damage is starting and progressing through the part. Also, due to the unique structure of composite parts, some defects and failures, only show while the part is loaded. And in turn, we will not be able to fully characterize the damage in an accurate and precise manner. This creates a real need for mechanical tests in-situ NDT. Ones that would not only allow us to see all the types of damage present at a part, but maybe also monitor the coalescence and progression of damage as well.

Micro X-ray Computed Tomography (CT)

X-ray computed tomography (CT) is a relatively new technique, adapted from the medical field [3], and has shown very promising improvements over the past few years. It is one of the very few techniques that can produce a 3D volumetric representation of the part being scanned, at a micron-level volumetric resolution. Which allows for detection of the material structure including manufacturing defects as well as structural damage such as cracks and delaminations in composites.

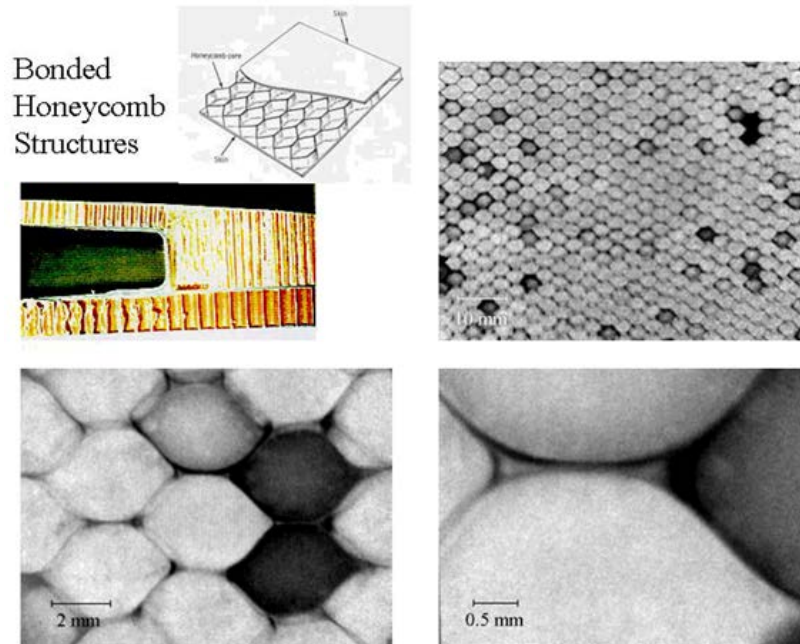


Figure 2-1 Sequence of magnified X-ray images of a composite honeycomb [2]

There are several x-ray sources used for x-ray tomography. Figure 2-2 shows a comparison between different x-ray sources [4]. Fan beams are the main x-ray sources used in hospitals, mainly because of the small x-ray dosage associated with them. However, it is unsuitable for laboratory usage as it will increase scan times significantly. Instead, cone beam x-ray sources are the dominant source for laboratory x-ray. New

micro-focus x-ray tubes offer micrometer level resolution at modern laboratories. Parallel x-ray beams allow for less artifacts during reconstruction, and faster scan times due to their much higher flux. Modern synchrotrons can generate such highly parallel beam, by delivering a very high flux at a small source size. Third generation synchrotrons can produce at least 1000 times larger flux compared to laboratory x-ray tubes. However, the high flux needed to create them, limits their widespread use. Currently, there are 14 Synchrotron Radiation facilities in the world [5]. It is worth noting that most published literature regarding in-situ experiments, took place at the European Synchrotron Research Facility (ESRF) [6].

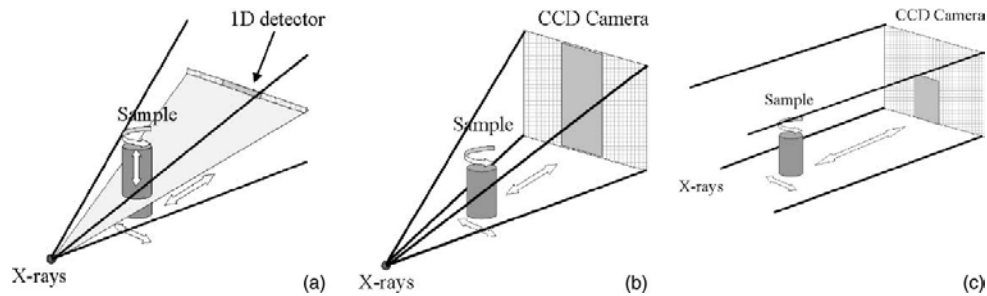


Figure 2-2 (a) Fan beam (b) Cone-beam (c) Parallel beam [4]

A schematic of the concept of work of x-ray tomography is shown in Figure 2-3. The part being scanned is exposed to x-rays, which projects a radon-transformed projection of the part on the x-ray detector. The machine repeats this process several times at specified angles that span 360° degrees (it could span less than 360 degrees in the case of a partial scan). Those scans are stored as high resolution image files on the computer. After all the projections are complete, the reconstruction process takes place. It uses one of the several reconstruction algorithms available to deduce a 3D solid or surface, from all the radon transformations obtained from the x-ray scans acquired earlier

(2D scans). Feldcamp-Davis-Kress (FDK) filtered back-projection reconstruction algorithm [7] is one of the most widely used reconstruction algorithms nowadays for its relative speed. These scans usually have a voxel size which is inversely proportion to the magnification at the time of the scan. After the reconstructed volume is created, it can be further studied for defects or damage. Recent work has been done by Nikishkov et al to facilitate the assessment of the structural integrity of composite parts from their reconstructed volumes using x-ray tomography [8].

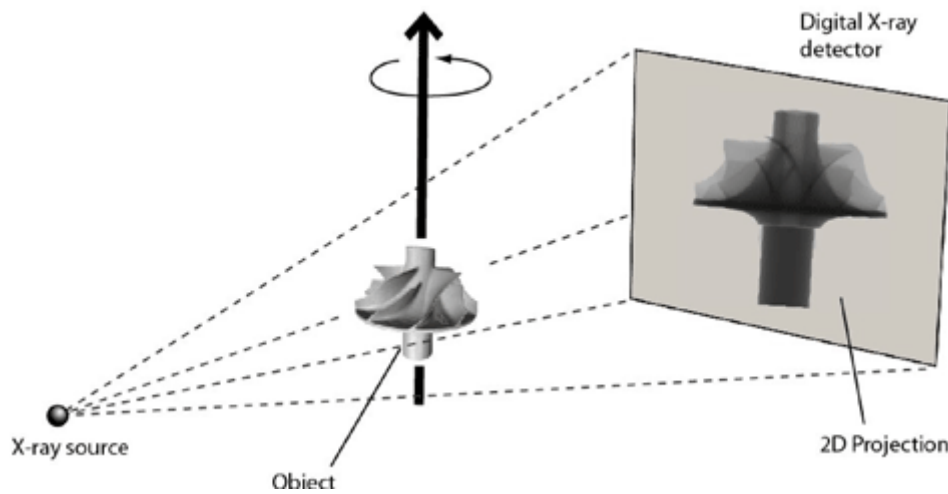


Figure 2-3 X-ray Tomography [9]

For this work, the X-5000 computed tomography machine from Northstar imaging [10] available at the AMSL lab at the University of Texas at Arlington will be used, Figure 2-4. This machine is fitted with an, x-ray worx, micro-focus, reflection cone x-ray tube. A schematic showing the main parts of a reflection x-ray tube is shown in Figure 2-5. The machine can achieve volumetric resolutions of less than 10 microns.



Figure 2-4 Northstar X-5000 micro CT x-ray tomograph

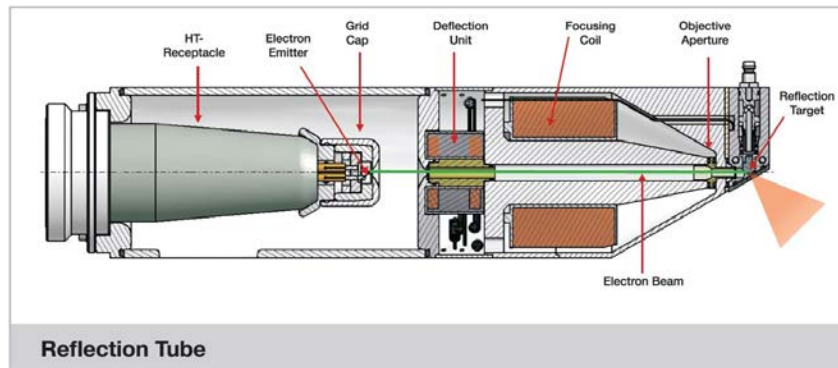


Figure 2-5 X-ray reflection tube [11]

Micro X-ray CT Considerations

There are several considerations associated with x-ray micro tomography. The relevant ones for this work will be discussed here. First, since x-ray beams are a form of radiation, they obey Newton's inverse square attenuation law. This means that x-ray energy attenuates with the inverse square of the distance travelled from the source,

Figure 2-6. And hence, the farther the detector is from the source, the less intense the projected image is, but the more magnified it will be. So Magnification, and image intensity have an inversely proportional relationship.

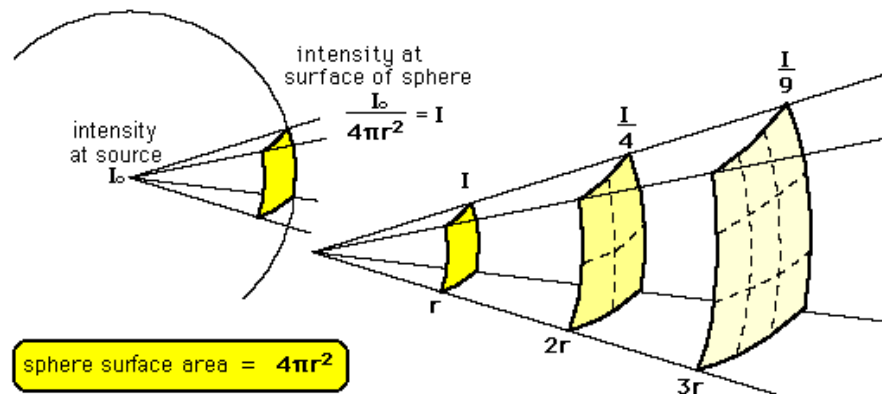


Figure 2-6 Inverse Square Attenuation [12]

Another characteristic of x-rays is the geometric un-sharpness. Geometric un-sharpness is the un-sharpness associated with any image projected by a non-point source. When the projected edges of the scanned object appear blurry or out of focus. X-ray un-sharpness is greatly affected by the size of the x-ray emitter, the source-to-object distance and the object to detector distance, as shown in Figure 2-7. As the emitter size increases, the projected geometric un-sharpness increases. Unfortunately, geometric un-sharpness and magnification are directly proportional. So at higher magnification, there will occur higher geometric un-sharpness. However, this should not be confused with effective un-sharpness at the radiograph level which is almost equal to the focal length for higher magnifications.

For certain micro-focus x-ray tubes, the focal size changes when the power output is higher than a certain threshold. For the micro-focus tube used at AMSL, the

tube defocuses when the output power is equal or higher than 30 Watts. When the tube defocuses, the focal size becomes equal to the power output in microns. For example, for 40 Watt power output, the focal size becomes 40 Microns. Which is a significant difference from the 5-7 micron nominal focal size [13].

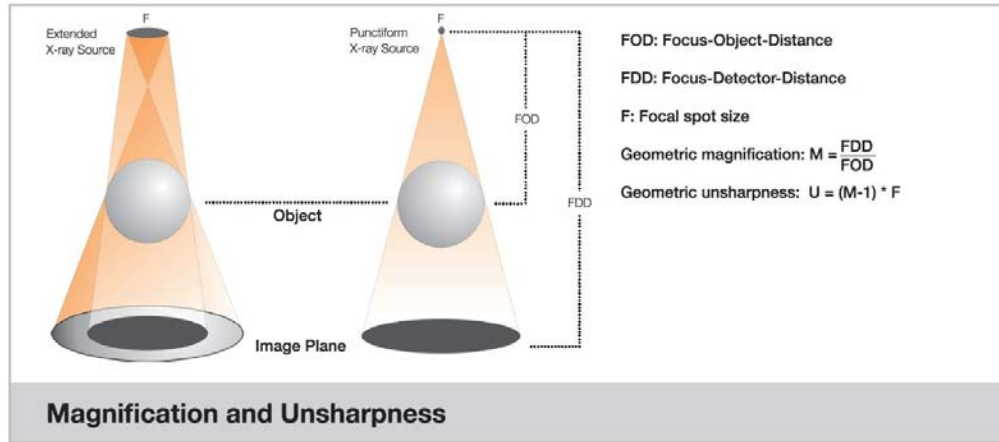


Figure 2-7 Geometric Magnification and Un-sharpness [14]

Ct scan technique is the collection of x-ray tube parameters (Volts and Amps), the Focus to Object Distance (FOD) and Focus to Detector Distance (FDD) parameters (shown above) and x-ray detector parameters (frame rate, pixel binning, etc) that characterize the scan quality and speed, among other metrics. The factors discussed earlier directly affect the design of the CT scan technique for a required scan result (certain scan time, certain magnification or contrast ration). They are also affected by any mechanical limitations the CT scanner system might have and this makes them especially important as the design of any in-situ system, would directly impact the FOD and FDD and in turn limit the allowable scanning techniques for the tested specimens. This means that if the system design/size imposes too many limitations on those parameters, certain material/magnification combinations might not be possible, and

hence render the machine useless for these cases (e.g. monitor micron-level damage inside a specimen that requires higher scan power).

Fractures in Composite Materials

As mentioned before, damage and fractures in composites is different from those in metals or monolithic materials. Damage in composites can fall under one of three main categories. Fiber damage, matrix damage, and interface damage (another form of matrix failure). They usually manifest as fiber breaking, matrix cracks and delaminations (which are interlaminar matrix cracks). Figure 2-8, Figure 2-9 and Figure 2-10 show x-ray reconstructed images demonstrating the different damage mechanisms found in composites.

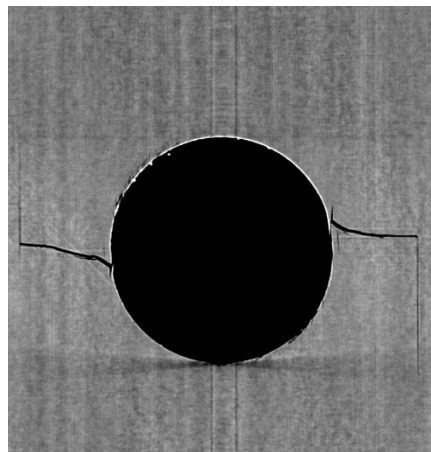


Figure 2-8 Fiber Breaking

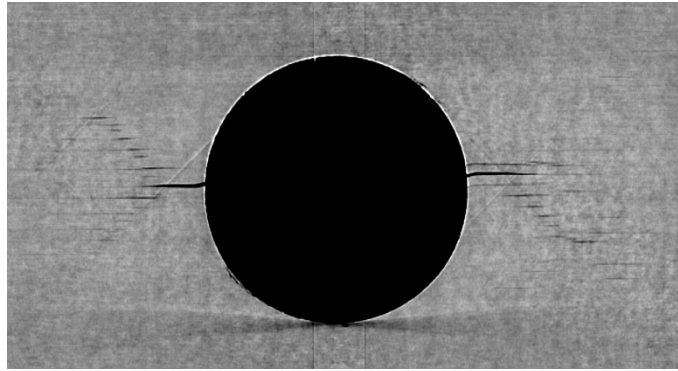


Figure 2-9 Matrix Cracks

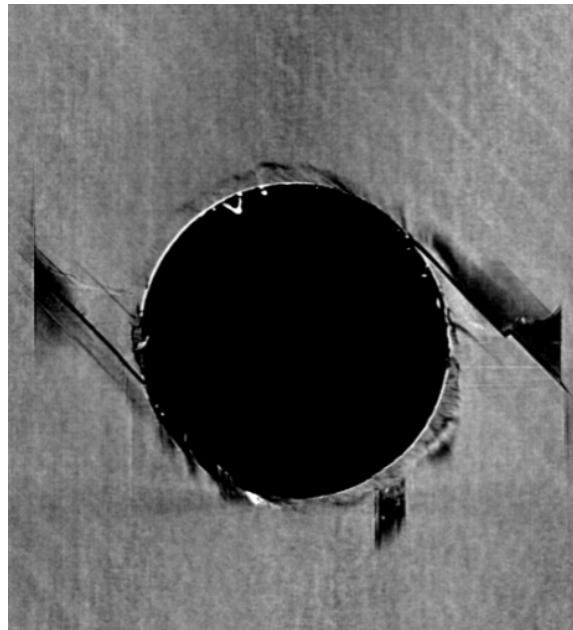


Figure 2-10 Delamination

To date, fractures in composite materials have been characterized using the commonly used principles of superposition of the basic fracture modes [15]. Figure 2-11 shows the different fracture modes for isotropic materials. Mode I is the opening mode, mode II is the sliding shear mode and mode III is the scissoring shear mode. Characterizing fractures in isotropic materials, such as metals, using these modes and

their respective tests is widely accepted because of their consistent and relatively accurate results. Unfortunately this is still not the case in composites because of the scatter in test data available for the same materials using the same tests [16].

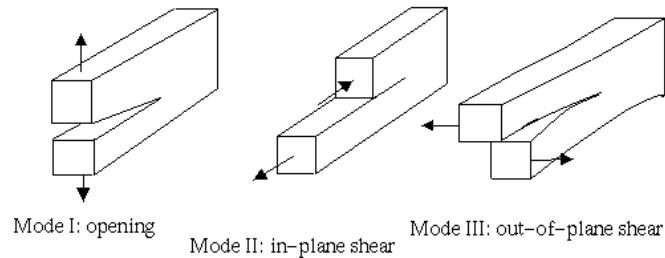


Figure 2-11 Different fracture modes

Current applications to fracture mechanics to composites have been limited to the number of observable damage which usually yields in-accurate results as the damage observed is usually just a fraction of the true damage in the structure. This is due to limitations in current detection techniques, and the fact that most observations are done after loads have been removed. This shows the real need to develop a more practical method that allows for fracture characterization using methods that truly replicate the loading conditions of in-service parts.

Tests for Fracture Toughness

Currently, these critical energy release rates are calculated using tests relying on surface measurement methods. The Double Cantilever Beam (DCB) test, is used to test for mode I cracks. The End Notched Flexure (ENF) test is used to characterize mode II cracks, and the split cantilever beam test is used to characterize mode III cracks. Edge Crack Torsion test is also used to characterize mode III fractures. There are several other tests that have been proposed that allow for measuring the fracture toughness of more

than one mode at once. Like the Arcan test. It allows for testing of mixed mode I and II cracks, while having the ability to vary the ratio of mode mix by changing the loading angle, Figure 2-16. The Mixed Mode Bending test (MMB) and the cracked Lap shear (CLS) tests also allow for measurement of mixed mode I and II fracture toughness for composites. The figures below show some of the tests mentioned above [17].

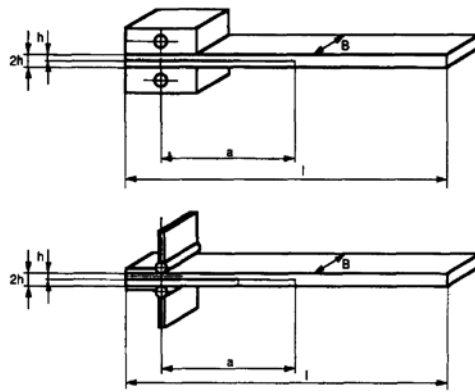


Figure 2-12 Double Cantilever Beam Test (DCB), Mode I

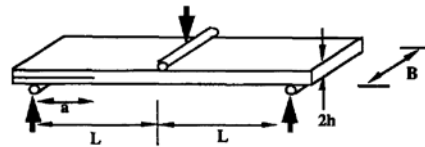


Figure 2-13 End Notch Flexure, Mode II

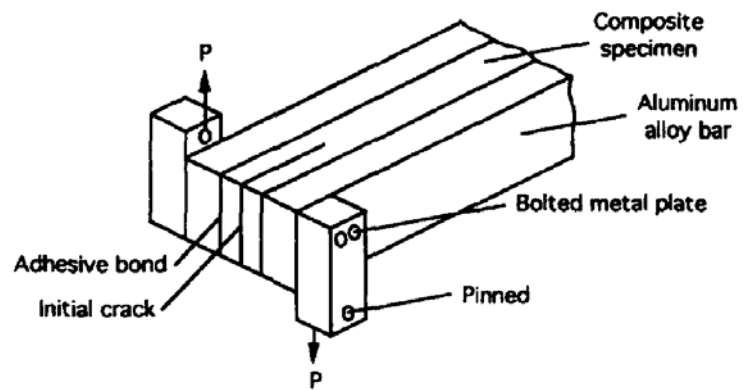


Figure 2-14 Split Cantilever Beam Test, Mode III

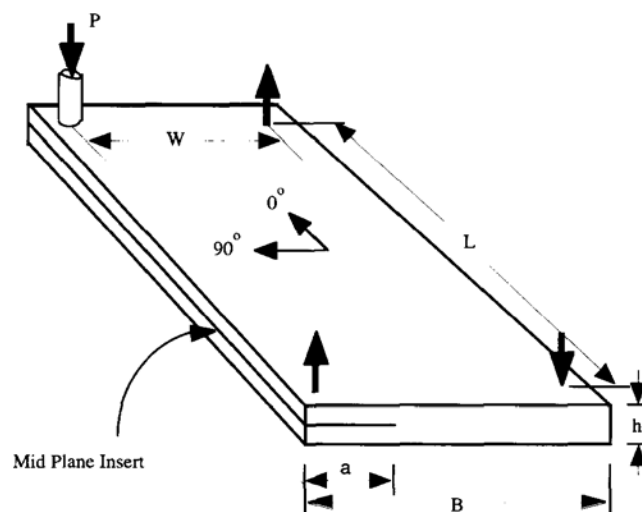


Figure 2-15 Edge Crack Torsion (ECT) test, Mode III

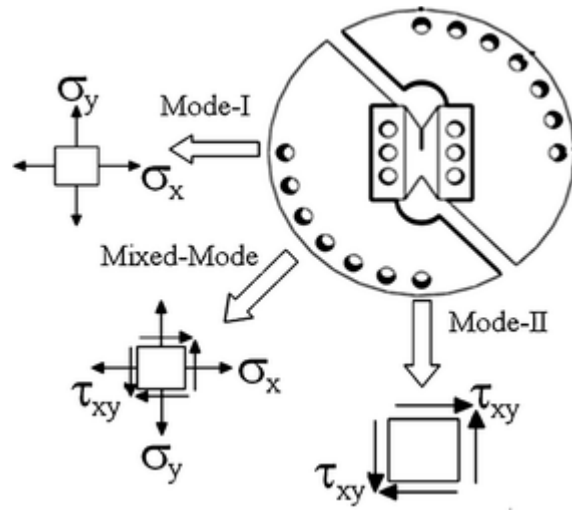


Figure 2-16 The Arcan test fixture [18]

Unfortunately, the methods mentioned above have several artifacts and limitations. Their behavior is still different from what is observed for delaminations for in-service parts. The DCB test for instance, experiences the fiber bridging artifact, which is a phenomenon not observed in composite laminates [17]. Also, all of them rely on the crack extending to the surface of the specimen so it can be observed and measured. This is almost never the case for in-service parts since most fractures develop internally first.

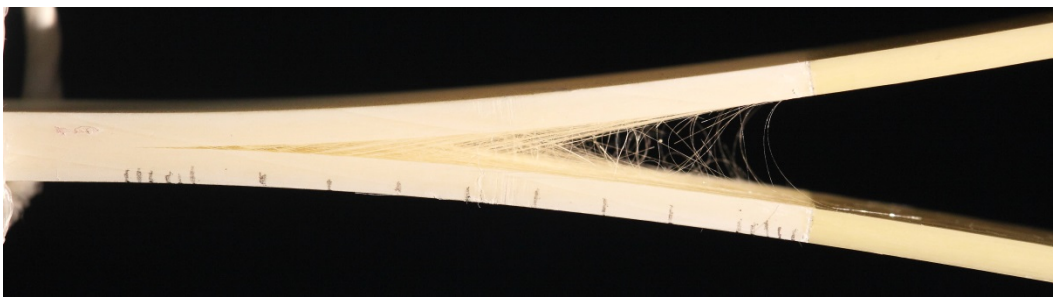


Figure 2-17 Fiber bridging in fiberglass DCB test

Calculation of Fracture Toughness

Fractures are usually characterized by the amount of energy required to grow the crack an extra unit of length, this is called the critical Strain Energy Release Rate, and designated the letter G after the English aeronautical engineer 'A. A. Griffith' who developed fracture mechanics during world war one [19]. Griffith theory depended on the elastic energy and ignored plasticity. In 1957, 'G.R. Irwin' included the effect of plasticity on the energy release rate for crack growth. Later Irwin developed the basis for the Virtual Crack Closure Technique (VCCT). According to him, the work required to extend a crack by an infinitesimal distance Δ , is equal to the work required to close the crack to its original length. This means that the energy release rates for mode I and mode II mechanisms can be expressed as [20]:

$$G_I = \frac{1}{2\Delta} \int_0^{\Delta} \sigma_{22}(x) \delta_2(\Delta - x) dx$$

$$G_{II} = \frac{1}{2\Delta} \int_0^{\Delta} \sigma_{12}(x) \delta_1(\Delta - x) dx$$

The above equations calculate the critical ERR for the respective modes. These values are later used in a modelling environment, to predict fracture propagation in the material. For instance, to predict delamination propagation under mixed mode loading, a delamination criterion must be used. The 'power law' criterion is one of the most widely used criteria for delamination; it is an interaction between the energy release rates. It was found suited to predict fracture of thermoplastic PEEK for $\alpha = 1$. However, it does not accurately capture the behavior of epoxy-matrix composites [21].

$$\left(\frac{G_I}{G_{Ic}}\right)^\alpha + \left(\frac{G_{II}}{G_{IIc}}\right)^\alpha = 1$$

Since this work will be focused on Mode I fractures in DCB specimens, and the calculation of the Strain Energy Release Rates using both analytical as well as numerical methods, in the following sub-sections, we will delve a little deeper into the details of both the experimental and numerical methods used to calculate the energy release rates.

Double Cantilever Beam Test

The double cantilever beam is the standard test for the calculation of mode I critical energy release rate or fracture toughness. Below is a review of two of the used data reduction methods for the calculation of mode I critical fracture toughness in DCB. The Modified Beam Theory (MBT) and the Compliance Calibration (CC) method.

The relevant standard for the DCB test is ASTM D5528-01, Standard Test Method for Mode I Interlaminar Fracture Toughness of Unidirectional Fiber-Reinforced Polymer Matrix Composites [22]. The standard lists the recommended specimen configuration and dimensions. It also has detailed guides for the experimental setup, and the post test data reduction methods.

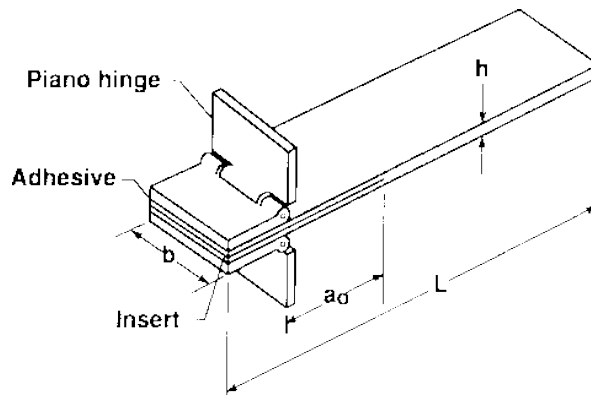


Figure 2-18 DCB specimen with piano hinges

The modified Beam Theory

The Modified Beam theory (MBT) is a variation of the well-known Euler-Bernoulli beam theory. It modifies the theory in a way that accounts for rotations at the crack tip which yields more accurate results than those just calculated from conventional Euler-Bernoulli beam theory. MBT is derived as follows.

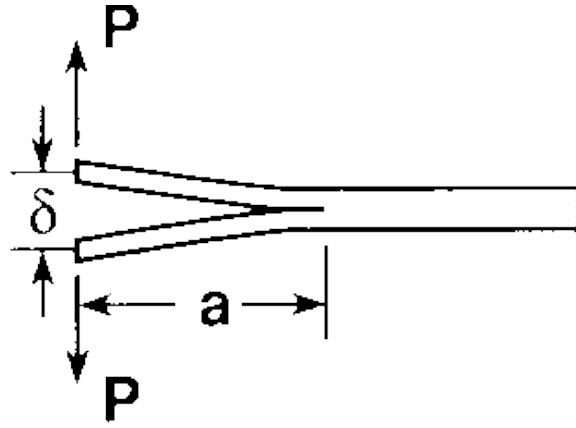


Figure 2-19 DCB specimen loading

For a DCB specimen with crack length 'a' and opening δ , if PE is the potential energy, and p is the applied force, mode I fracture toughness would be given as:

$$G_I = - \left[\frac{\partial PE}{\partial a} \right]_p \quad (1)$$

For prescribed loading p, the potential energy is equal to the Strain Energy minus the work done.

$$PE = SE - p\delta = \frac{1}{2}p\delta - p\delta = -\frac{1}{2}p\delta \quad (2)$$

$$\therefore G_I = \left[\frac{1}{2} \frac{\partial p\delta}{\partial a} \right]_p = \frac{p}{2} \left[\frac{\partial \delta}{\partial a} \right]_p \quad (3)$$

Define the compliance of a body to be:

$$c = \frac{\delta}{p} \quad (3)$$

$$\therefore G_I = \frac{1}{2} p^2 \frac{dc}{da} \quad (4)$$

From beam theory:

$$\frac{\delta}{2} = \frac{Pa^3}{3EI} \quad (5)$$

$$\therefore c = \frac{\delta}{p} = \frac{2a^3}{3EI} \quad (6)$$

Then, for a rectangular cross section of width b and height h , the Fracture toughness per unit width can be found to be:

$$G_I = \frac{p^2 a^2}{bEI} = \frac{12p^2 a^2}{Eb^2 h^3} \quad (7)$$

Also, substituting equation 5 into 7 we get :

$$G_I = \frac{p^2 a^2}{EI} = \frac{3p\delta}{2ba} \quad (8)$$

The above equation represents the fracture toughness calculated according to Beam Theory. But since the fracture toughness based on just beam theory underestimates the value of G_I , the modified beam theory is used instead. The modified beam theory adjusts the known beam theory fracture toughness equation (equation 8) by adding a correcting factor to the crack opening length obtained from the cubic root of the compliance plotted against the crack length. The x-intercept is the factor that is added to the crack length used in the modified beam theory equation (see Figure 2-20)

The modified beam theory is given as:

$$G_I = \frac{3P\delta}{2b(a+\Delta)} \quad (9)$$

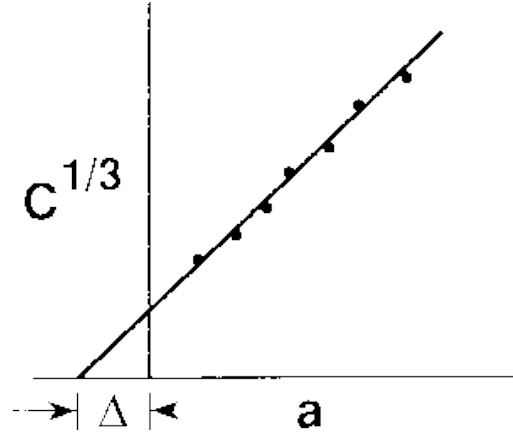


Figure 2-20 MBT correction factor

Compliance Calibration (CC) Method

For the compliance calibration (CC) method, the factor n in the equation below, is the slope of the plot of the logarithm of the compliance, versus the logarithm of the crack length, as shown in Figure 2-21.

$$G_I = \frac{nP\delta}{2ba} \quad (10)$$

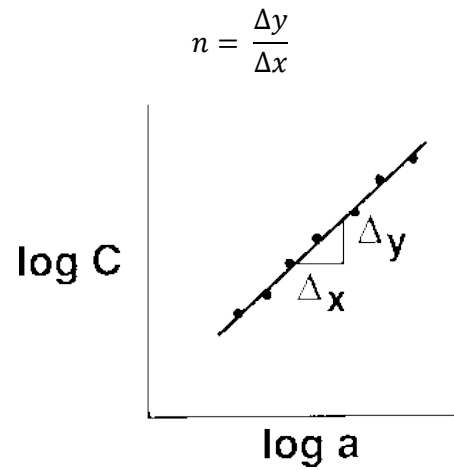


Figure 2-21 Compliance Calibration slope

There is a third data reduction method outlined in the standard which is the modified compliance calibration (MCC) method. It is not used in this work as the two aforementioned data reduction methods were sufficient.

Critical Strain Energy Release Rate (G_{Ic})

Because of the well-known fiber bridging phenomenon in DCB tests of composite materials [22], the critical fracture toughness is taken to be one of three values. The ERR at the non-linearity point, the ERR at the Visual crack point, and the ERR at the 5% point. Because of the micro resin pocket that forms at the teflon insert tip [16]. The mode I fracture toughness in this study is chosen to be the first visual (VIS) crack progression point, after the pre-crack is introduced in the specimen.

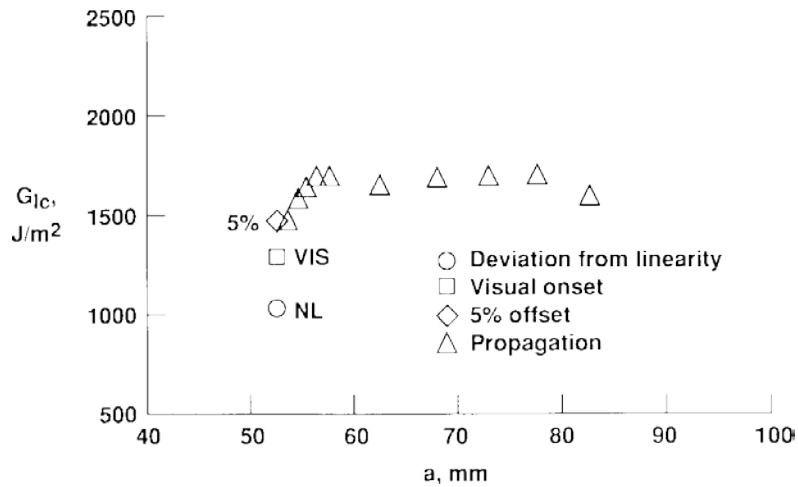


Figure 2-22 R-curve showing the NL, VIS and 5% points

Fracture Toughness Calculation in FEA

The Strain Energy Release rate was calculated in the finite element models using two different methods. The Virtual Crack Closure Technique (VCCT), and the J-integral over 7 contours. An explanation of both methods and how they are implemented in FEA is shown next.

Virtual Crack Closure Technique (VCCT)

The foundation for the Virtual Crack Closure Technique was laid down by Irwin et al in 1957. The main concept is that for a given crack, the energy required to progress that crack by a unit length, is the same as the energy required to close that crack back to its original state. This allows for calculation of strain energy release rates using forces at the crack front, and displacements behind it. In VCCT, for a corner node, in an 8 noded brick element, the fracture toughness for the different fracture modes can be calculated, using the equations below [23], [24]. $\Delta A = \Delta a \cdot b$ is the opening area as shown in Figure

2-23. X_{KI} , Y_{KI} , Z_{KI} are the shear, transverse, and normal force components respectively at node ' n ' in row ' K ' and column ' I '. U, V, W are the nodal displacements in the X, Y, and Z directions respectively.

$$\begin{aligned}
 G_I &= -\frac{1}{2\Delta A} \cdot Z_{Li} \cdot (w_{L\ell} - w_{L\ell^*}) \\
 G_{II} &= -\frac{1}{2\Delta A} \cdot X_{Li} \cdot (u_{L\ell} - u_{L\ell^*}) \\
 G_{III} &= -\frac{1}{2\Delta A} \cdot Y_{Li} \cdot (v_{L\ell} - v_{L\ell^*})
 \end{aligned} \tag{10}$$

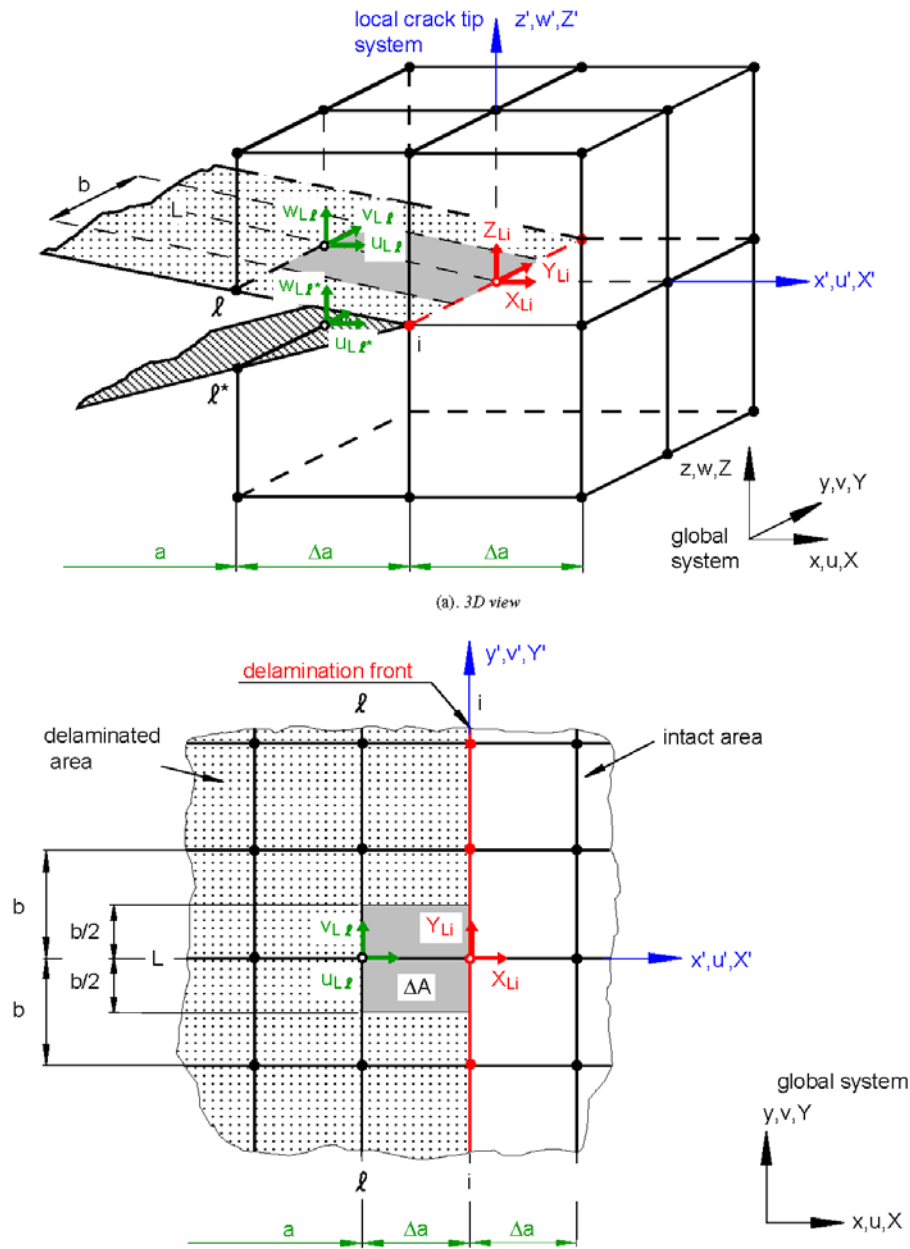


Figure 2-23 VCCT for 8 noded brick element [23]

For a 20 noded, non-linear element, the edge mid-point nodal forces and displacements also contribute to the value of the calculated fracture toughness as per the

elements' shape function. For the corner node in a 20 noded nonlinear brick element, the different mode fracture toughness values are calculated by using equations 11 as shown in Figure 2-24 and Figure 2-25. ΔA is the area the force is acting upon, as shown in the figure. X , Y and Z are the force components in the x , y and z directions respectively. U, V, W are the nodal displacements in the X , Y , and Z directions as well.

$$\begin{aligned}
 G_I &= -\frac{1}{2\Delta A_L} \left[\frac{1}{2} Z_{Ki} (w_{K\ell} - w_{K\ell}^*) + Z_{Li} (w_{L\ell} - w_{L\ell}^*) + Z_{Lj} (w_{Lm} - w_{Lm}^*) + \frac{1}{2} Z_{Mi} (w_{M\ell} - w_{M\ell}^*) \right] \\
 G_{II} &= -\frac{1}{2\Delta A_L} \left[\frac{1}{2} X_{Ki} (u_{K\ell} - u_{K\ell}^*) + X_{Li} (u_{L\ell} - u_{L\ell}^*) + X_{Lj} (u_{Lm} - u_{Lm}^*) + \frac{1}{2} X_{Mi} (u_{M\ell} - u_{M\ell}^*) \right] \\
 G_{III} &= -\frac{1}{2\Delta A_L} \left[\frac{1}{2} Y_{Ki} (v_{K\ell} - v_{K\ell}^*) + Y_{Li} (v_{L\ell} - v_{L\ell}^*) + Y_{Lj} (v_{Lm} - v_{Lm}^*) + \frac{1}{2} Y_{Mi} (v_{M\ell} - v_{M\ell}^*) \right].
 \end{aligned} \tag{11}$$

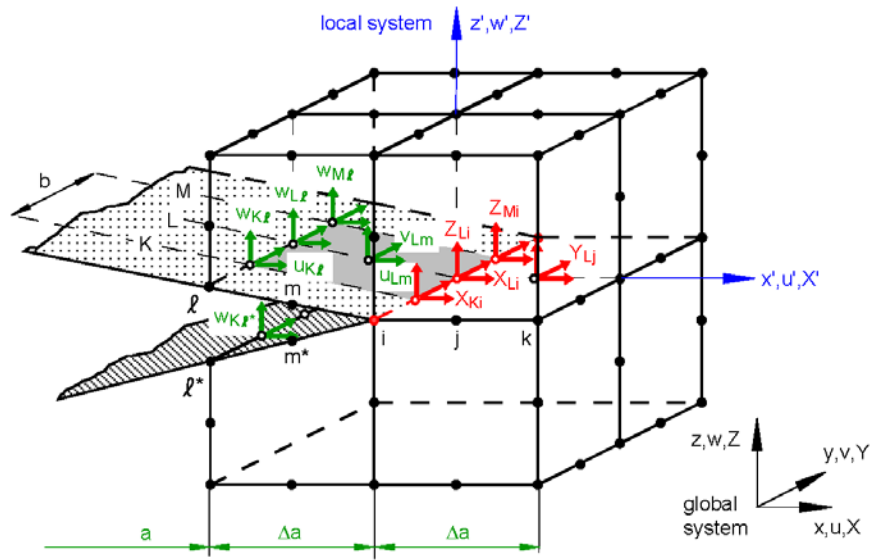


Figure 2-24 VCCT for corner node in a 20 noded element - 3D [23]

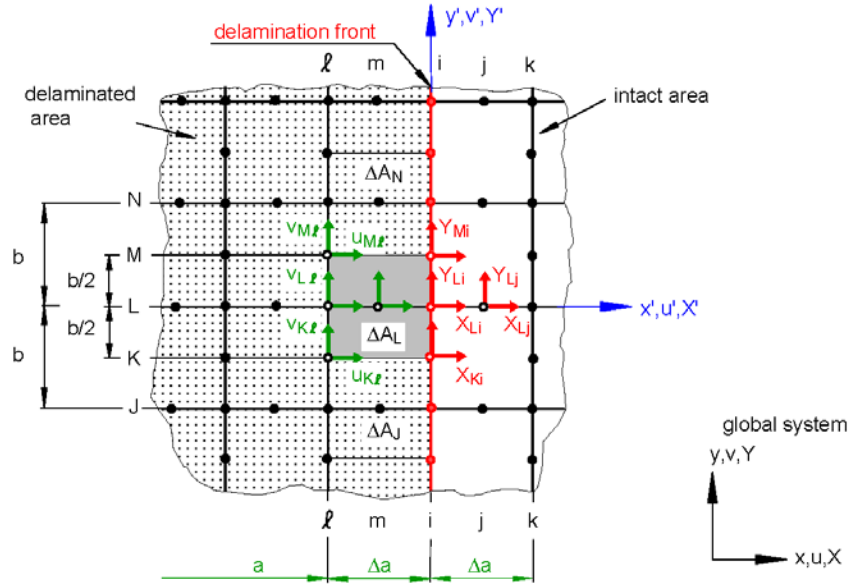
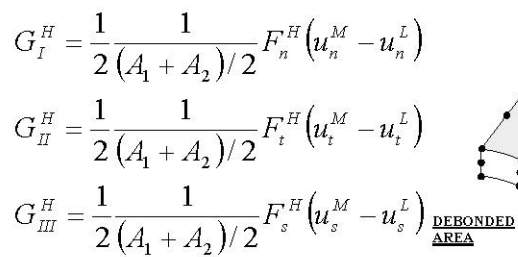


Figure 2-25 VCCT for corner node in a 20 noded element - 2D [23]

For curved crack fronts, the shear forces and corresponding nodal displacements should be transformed in order to properly be able to calculate, and separate, the correct mode II and mode III fracture energies. This can be achieved once the normal vector to the crack front is identified by using dot and cross products with one of the principal axis to form the sine and cosine of the angle of rotation of the vector. A rotation matrix can be easily constructed from those values.



The nodal forces in FEA can be calculated using different methods. One method is using a stiff 1-DOF spring elements to connect the top and bottom nodes that we need forces for (see Figure 2-26). This allows us to retrieve the total force magnitude acting at the node in question without doing much post processing.

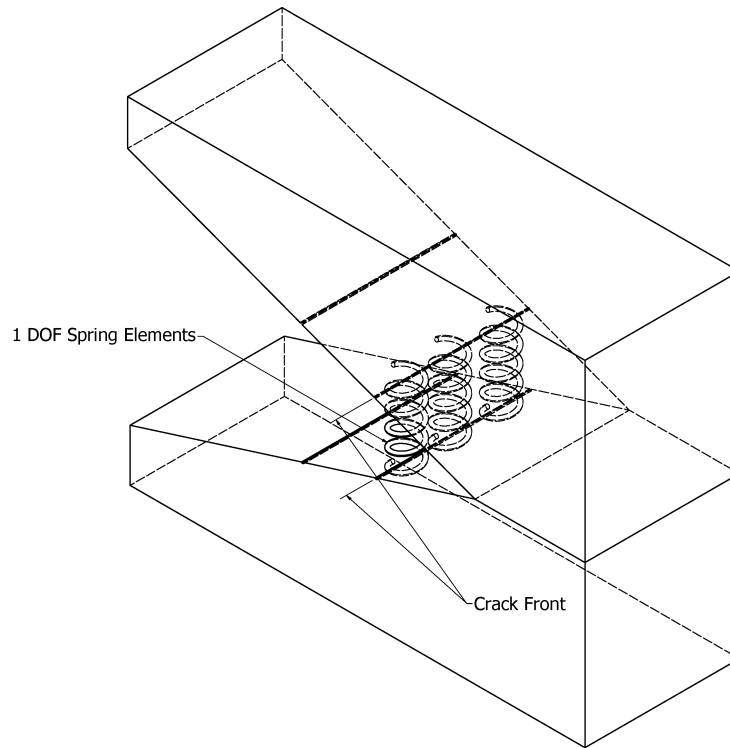


Figure 2-27 Nodal forces using spring elements

Another method is using half the elements connected at the node in question, and normal to the direction of crack growth, to calculate the resulting force. The force is the sum of the force contributions of each of these elements. Element sets can be generated for each node to calculate the forces from the contribution of each element in the set for the required direction. Figure 2-27 shows the normal forces from element contribution for nodes shown using the element contribution method. Nodal forces from element contribution method are used for this work.

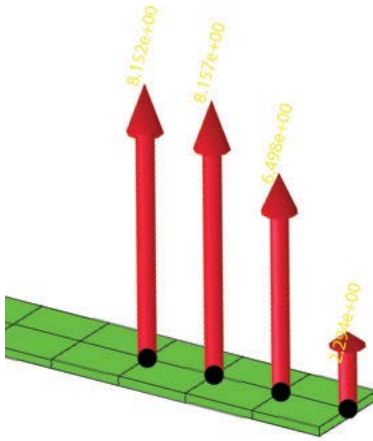


Figure 2-28 Nodal forces from element contribution

J Contour Integral

Another method used to calculate the strain energy release rate is the J Contour integral [15]. The J-Integral was originally derived by Rice. It is a path independent contour integral that evaluates to the strain energy release rate if calculated around the crack front. It is given as:

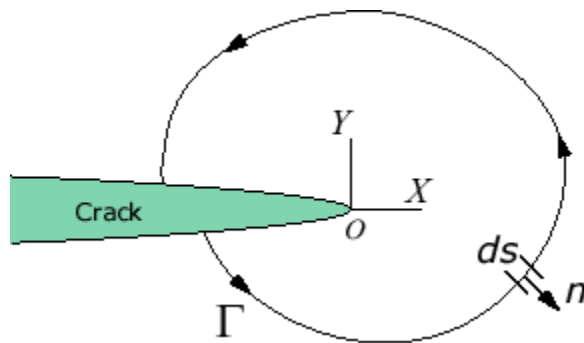


Figure 2-29 J integral Contour

$$J = \int_{\Gamma} w dy - T_i \frac{\partial u_i}{\partial x} ds$$

Where w is the strain energy density, T_i is the traction vector, Γ is an arbitrary contour around the tip of the crack, n is the unit vector normal to Γ ; σ , ϵ , and u are the stress, strain, and displacement fields, respectively.

$$w = \int_0^{\epsilon_{ij}} \sigma_{ij} d\epsilon_{ij}$$

$$T_i = \sigma_{ij} n_j$$

Some commercial finite element packages, like Abaqus, have the built in capability to evaluate the j-contour integral for a set number of nodal contours around the node in question automatically and outputs the energies associated as a history output [26]. This capability is used in their work, in conjunction with the VCCT method.

Chapter 3

Literature Survey

In-situ Experiments with X-ray

The earliest apparatus found for experiments in-situ x-ray tomography was presented by Breunig et al [27] in 1992. The load frame has a polycarbonate support stand-off tube with an outer diameter of 50.4 mm and 2.8 mm wall thickness. The tube can support up to 200kg of force and the maximum length inside the tube is 100 mm. The sample was 38.1 mm long. Loads were applied using a pneumatic actuator. They did report that the thickness of the polycarbonate tube did cause a significant decrease in x-ray photon flux.

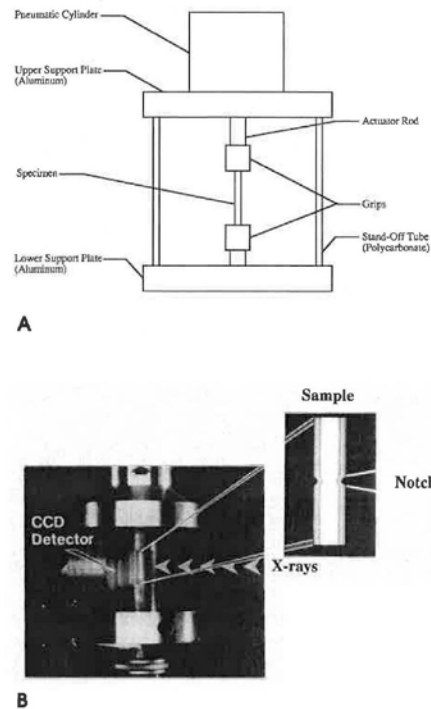


Figure 3-1 Device by Breunig et al a) Schematic and (b) photograph [27]

Later, Guvenilir et al [28] used the apparatus designed by Breunig et al to test crack opening of Aluminum - Lithium alloy (Al-Li 2090 T841). The largest specimen dimension was 38.1 mm, and the maximum applied load was 90 kg. The tests were conducted in a laboratory tomograph, and a reconstructed voxel size of 6.3 μm was achieved.

Then, in 1999, Buffiere et al [29] used an in-situ test apparatus similar in concept to the one developed by Breunig, however, they used a PMMA support tube instead. The tests were conducted at beam line ID19 at ESRF. Specimens made out of AL 6061 alloy reinforced with SiC particles were tested. Samples were small, with a cross section of $1.5 \times 1.5 \text{ mm}^2$, and a gauge length of 4 mm. It is important to note that they noticed a stress drop of less than 10% while the cross head displacement was kept constant.

Buffière et al [30] also used the same in-situ device described in [29] tests were conducted at beam-line ID19 at ESRF. They tested Aluminum based metal matrix composites, reinforced by spherical zirconia based particles. The specimen section being scanned was a $1 \times 1 \text{ mm}$ section. A reconstructed voxel size of 0.7 μm was achieved.

Maire et al [31] also used the same apparatus described in [29] to test two aluminum matrix composites, with two types of reinforcement amounts (1% and 4%). The tests were conducted at beam-line ID19 at ESRF. Largest specimen dimension was 4mm. A reconstructed voxel size of 0.7 μm was achieved.

Swygenhoven et al [32] presented an in-situ device for mechanical testing [33]. The same device is also described in [34]. This device is designed for powder diffraction x-ray scanners. These scanners use fan beams, the specimen is loaded using a single support loading apparatus. Which would make it unsuitable for micro x-ray tomography machines.

Maire et al [35] have investigated damage in metals using in-situ mechanical testing. They used beamline ID19 at ESRF. So it is assumed that they used the same apparatus described in [29]. They did observe plastic relaxation where stress drops while the displacement is kept constant. Continuous in-situ scanning was also demonstrated. Largest specimen dimension was 59.8 mm. There was no mention of the resolution or the voxel size

Bayraktar et al [36] studied the mechanical properties and fracture behavior in Elastomeric Matrix Composites by means of an in-situ x-ray tomography. They used an Exel 2000 model medical x-ray scanner, and for the in-situ tensile loading they used a simple apparatus composed of an electrical Jack and a carbon fiber support tube equipped with a load cell.

Germaneau et al [37] also used a PMMA tube as a support for load application. Experiments were conducted inside a laboratory tomograph. The materials tested were polyurethane and silicone, embedded with polyamide or copper particles. Specimen largest dimension is reported to be 150mm. A voxel size of 60 μm was achieved.

Hulme et al [38] tested spinal end plates using an in-situ apparatus. They used a lead screw with 0.5mm pitch to apply the load and an Ertacetal C [39] as a support tube. Load and displacement were monitored using a miniature load cell (1000lb) and an LVDT. Tests were conducted in a medical micro-CT [40], and a voxel size of 82 μm was achieved.

Maire et al [41] studied the initiation and growth of damage in dual-phase steels using the in-situ apparatus described in [29]. The tests were conducted at beamline ID15 at ESRF. The specimen's largest dimension was 5mm and the reconstructed voxel size was 2 μm .

Barranger et al [42] also used an in-situ device. The concept of operation of the device is not explicitly explained in their work, however, from the figure provided, it is clear they used a clear support tube, so it is similar in concept to other in-situ devices discussed earlier. What is new in this work though is that they used the results from their in-situ scans, with the help of Digital volumetric Correlation techniques, to characterize the fracture mechanics of a single edge notched specimen. Tests were conducted on a polyurethane specimen, with copper particle inclusions for DVC purposes. The specimen's largest dimension was 70mm. the specimen was subject to a load of 36N during tests. All tests took place in a laboratory tomograph, and 45um volumetric resolution was achieved.

In [43], Buffiere et al showcase several in-situ devices for mechanical and thermal testing of materials in-situ x-ray tomography. They show a monotonic tension / compression device designed and built by P. Michaud and C. Touboulic from INSA Lyon. It is similar in concept and design to the one designed by Breunig et al [27] and the one described in [29]. The tension-compression device has a static load cell and grip on the bottom. The top grip is attached to a computer-controlled stepping motor. The load is transferred to the specimen via a Polymethylmethacrylate (PMMA) tube. Loading rates between 10^{-4} and 1 mm/s can be achieved. And the load capacity ranges from 50 to 500 N depending on the load cell used and the support tube (an aluminum one is also available for high energy tests). The apparatus is 30cm high.

Hufenbach et al [44] used an aluminum support tube in their apparatus, their design also relied on accurate alignment of the apparatus due to their adverse effects on the observed failure behavior. They tested two types of materials , classical woven composites, and composites made of bi-axially reinforced weft knitted fabrics. All tests were conducted in a laboratory tomograph. A reconstructed resolution of 25um was

achieved using their current setup. They also claimed that a voxel size of 5um was achievable with certain modifications to the load frame using a smaller support tube.

Réthoré et al [45] used an in-situ fatigue apparatus with a PMMA support tube. Beam line ID19 at the ESRF was used. Cast iron Specimens were tested, the specimen cross section being scanned was $1.6 \times 1.6 \text{ mm}^2$. They used Digital Volume Correlation (DVC) technique to track the progression of cracks in the specimen. They also created an eXtended Finite Element (X-FEM) model for the same specimen and compared both results.

Scott et al [46] used an in-situ screw driven load frame. The apparatus also uses a support tube, unfortunately there was no reference as to what material it is made from, even in their listed reference [47]. tests were conducted at beamline ID19 at ESRF. Aerospace grade, carbon fiber, [90/0]s, specimens were tested. Largest specimen dimension was reported to be 66 mm. A voxel size of 1.4 um was achieved.

Bale et al [48] used a sophisticated test device for loading under high temperature, in-situ x-ray tomography. The device uses its own support system, similar to having a support tube, and is still put on the rotating table to record the various scanned angles. However, because this device has the same concept as others mentioned above, and since high temperature testing is beyond the scope of this work. No further investigation will be performed on the specific components of the device. And the fact that it still uses a support system, and that it is still put on the rotating table will suffice for this literature survey.

Fabrègue et al [49] used the apparatus described in [29] to compare damage evolution in two austenitic steels, the 316L and TWIP. The tests were performed at beam line ID15 at ESRF. The reconstructed voxel size was 1.6 um.

Hosokawa et al [50] also used the apparatus described in [29]. High purity copper laminates with voids were tested. Specimens were 10mm x 30mm. There was no mention of the maximum load used. Tests were conducted at ESRF ID15 beam line.

Landron et al [51] used the apparatus described in [29] to study void coalescence in dual phase steel. Specimens had a 60 mm gage length [52]. Tests were conducted at beamline ID15 at ESRF, and a reconstructed resolution of 1.6 μm was achieved.

Williams et al [53] used the in-situ apparatus that has a PMMA support tube, and loads are applied using a linear stepper motor. The apparatus has lateral and axial alignment mechanisms. 7075-T6 aluminum alloy was tested. The largest specimen dimension was 15 mm. Tests took place at beam-line 2BM at the Advanced Photon Source (APS) at Argonne National Laboratory, and a reconstructed resolution of 1.8 μm was achieved.

Hu et al [54] have conducted in-situ mechanical tests on short carbon fiber / epoxy laminates. Experiments were conducted at beam line BL13W1 at Shanghai Synchrotron radiation Facility (SSRF) [5]. They used a regular Test frame that has a support. And since the support blocks about 50° of the angle of view, they used a special reconstruction technique to reconstruct the whole volume from a partial scan.

Lachambre et al [55] used an in-situ fatigue test apparatus described in [56], to characterize crack initiation and progression in nodular graphite cast iron. The apparatus has an aluminum support tube made from AL 2024 alloy. The tube has a diameter of 16 mm and wall thickness of 1mm. A laboratory tomograph was used for these experiments, and a voxel size of 25 μm was achieved.

BAM, the federal institute of material testing in Germany [57] has a tensile test machine integrated in an X-ray-refraction scanner [58]. No details were given as to the

specifics of the design of the apparatus, or how it functions. But since the x-ray scanner used is a refraction x-ray. It will not be suitable for x-ray tomography.

Commercially, a company called Deben was found to offer a product called CT5000 5KN in-situ tensile stage for μ XCT applications [59]. While the product seems to have its own rotation stage on the bottom. It still employs a support tube made out of vitreous carbon [60]. The machine is reported to apply loads up to a maximum of 5KN (1.1 klf), and a maximum displacement of 10 mm.

Table 3-1 Current Implementations of In-situ Devices

#	Who	Source	Tube Mat.	Max. Dim.	Load	Material	Resolution
1	Breunig et al [27]	Laboratory	Polycarbonate	38.1 mm	449.6 kg	Al-Li alloy 2090	200 um
2	Guvenilir et al [28]	Laboratory	Polycarbonate	38.1 mm	202.3 lbf	Al-Li 2090 T841	6.3 um
3	Buffiere et al [29]	ESRF ID19	PMMA	4 mm	n/a	AL 6061 with SiC reinforcement	0.7 um
4	Buffière et al [30]	ESRF ID19	PMMA	1 mm	n/a	AL based metal Matrix Composite	0.7 um
5	Maire et al [31]	ESRF ID19	PMMA	n/a	n/a	AL based metal Matrix Composite	0.7 um
6	Swygenhoven et al [32]	Powder Diffraction	Single Support	n/a	n/a	n/a	n/a
7	Maire et al [35]	ESRF ID19	PMMA	59.8 mm	n/a	n/a	n/a
8	Bayraktar et al [36]	Medical X-ray scanner	Carbon Fiber	n/a	n/a	Elastomeric Matrix Composites	n/a
9	Germaneau et al [37]	Laboratory	PMMA	150 mm	n/a	polyurethane and silicone composites	60 um
10	Hulme et al [38]	Medical X-ray scanner	Ertacetal C	100 mm	1000 lbf	spinal end plates	82 um
11	Maire et al [41]	ESRF ID15	PMMA	n/a	n/a	DP Steels	2 um
12	Barranger et al [42]	Laboratory	Clear Plastic	70 mm	8 lbf	Polyurethane Composite	45 um
13	Hufenbach et al [44]	Laboratory	Aluminum	n/a	n/a	Composites	25 um
14	Réthoréa et al [45]	ESRF ID19	PMMA	1.6 mm	n/a	Cast Iron	0.7 um
15	Scott et al [46]	ESRF ID19	n/a	66 mm	n/a	Carbon Fiber	1.4 um
16	Bale et al [48]	n/a	n/a	n/a	n/a	n/a	n/a
17	Fabrègue et al [49]	ESRF ID15	PMMA	n/a	n/a	Austenitic Steels	1.6 um
18	Hosokawa et al [50]	ESRF ID15	PMMA	30 mm	n/a	Copper Laminates	n/a
19	Landron et al [51]	ESRF ID15	PMMA	60 mm	n/a	DP Steel	1.6 um
20	Williams et al [53]	APS 2BM	PMMA	15 mm	n/a	7075-T6 AL Alloy	1.8 um
21	Hu et al [54]	SSRF BL13W1	Single Support	n/a	n/a	Carbon Fiber	n/a
22	Lachambre et al [55]	Laboratory	AL 2024	n/a	n/a	Cast Iron	25 um
23	BAM [57]	X-ray refraction	n/a	n/a	n/a	n/a	n/a
24	Deben company [59]	n/a	vitreous carbon [60]	n/a	1,100 lbf	n/a	n/a

Limitations of Current In-Situ Devices

Table 3-1 shows a comparison between all in-situ attempts listed above. From the table, we can see that the maximum specimen dimension scanned was 150 mm, but the average specimen size (after removing the outliers) was 48.1 mm. This is relatively small for a laboratory specimen, and would hardly allow for testing of in-service parts as well. The reconstructed resolution varied largely, mainly because of the sheer difference in flux available between laboratory x-ray sources, and the high flux synchrotron ones. However, for laboratory x-ray source, and also after removing the highest and lowest outliers, tests conducted resulted in an average reconstructed resolution of 47.4 μm . This is a large value considering that they all used micro-focus x-ray sources. It is believed that this is due to the minimum distance imposed by the existence of the support tube. The maximum load capacity was 1,100 lbf. That is very limited for any standard laboratory specimen, and would require for special considerations while fabrication, testing, and analysis of these specimens.

The limitations associated with using a normal test frame for in-situ measurements are clear. The existence of the support structures, be that a single or double supports, enforces a large minimum distance between the x-ray source and the scanned object. Also, since these supports are usually made of some variation of steel metals, it will block most radiation as reported by Hu et al [54]. Which, in turn, enforces the use of specialty reconstruction techniques and algorithms in order to be able to reconstruct the full volume from a partial scan. The weight of the test machine could also be a limiting criterion. Several scanning facilities, be that a laboratory tomograph or a synchrotron source, have turntables with relatively small weight limits, associated with the lighter specimens usually scanned. And since table-top load frames range in weight from around 100 lb for 112 lbf capacity frame [61], to around 700 lb for 10,000 lbf capacity load

frame [62]. These weights could be well beyond the weight limits for most of today's x-ray scanning facilities. Which further limits their use.

There are also several shortcomings associated with in-situ devices employing a support tube to apply loads to the specimen. First, if the support tube has any significant surface roughness, this could result in extra contrast at the radiographs, especially in the case of synchrotron radiation [43]. So the tube has to be carefully polished in order to minimize this effect. Second, the presence of the tube limits the minimum distance between the x-ray source and the object, as mentioned earlier. This would imply a certain level of phase contrast in the reconstructed images, and could also lead to perturbation for subsequent image processing of the 3D data sets. Also, this minimum distance limitation, would limit the geometric magnification that can be achieved using laboratory tomographs. A device with a smaller tube diameter could be used [44], but that would significantly limit the size of the scanned specimen.

Another limitation that would be especially problematic for low-energy, laboratory tomographs, is the fact that the support tube material absorbs some of the beam energy. This in turn, would limit scanning at certain material-magnification combinations. Because, for cone or fan beam x-ray systems, to achieve higher magnifications, you would want the detector to be as far as possible from the source. And since x-rays follow the inverse square rule, and with the support tube absorbing some of the energy emitted by the source, this would leave little room for contrast control at higher magnifications, without increasing the output power. And since some laboratory x-ray tubes experience 'defocusing' when the power crosses a certain threshold, which would in turn increase the geometric un-sharpness. This means that for certain materials, certain magnifications would not be achievable because of the existence of the support tube.

Double Cantilever Beam Testing

Double Cantilever Beam (DCB) has been the standard for Mode I fracture toughness testing for both Metals, and later, composite structures for several decades. The test procedure and data reduction techniques are as discussed in the background section earlier.

It is known that DCB specimens failing under mode I failure exhibit curved crack fronts. This has been observed in DCB specimens failing under static loading by C.T. Sun and Davidson [63], [64], and under fatigue loading by Schön et al [65]. They have observed that the crack develops to a curved front from the onset of fracture. Schön et al detected this by observing the fatigue rings after total failure of the specimen under fatigue loading [65]. This method lacks accuracy and is only indicative of the rough shape of the crack front, not its exact location. It is also limited to fatigue loaded DCB specimens, unlike the ASTM standard test which is statically loaded. The curved crack front was also observed by ex-situ non-destructive testing during an actual test, using ultrasonic testing techniques, as performed by Davidson et al. [66]. Observing the crack front using this method will impact the accuracy and confidence level of the standard test as it involves removing the specimen from the loading fixture, scanning it, then replacing it back and resuming the test. And given the nature of ultrasonic scans, the accuracy and level of detail are inferior to those acquired using Micro CT. To date, no one has observed the progression of the crack front in DCB specimens In-Situ testing.

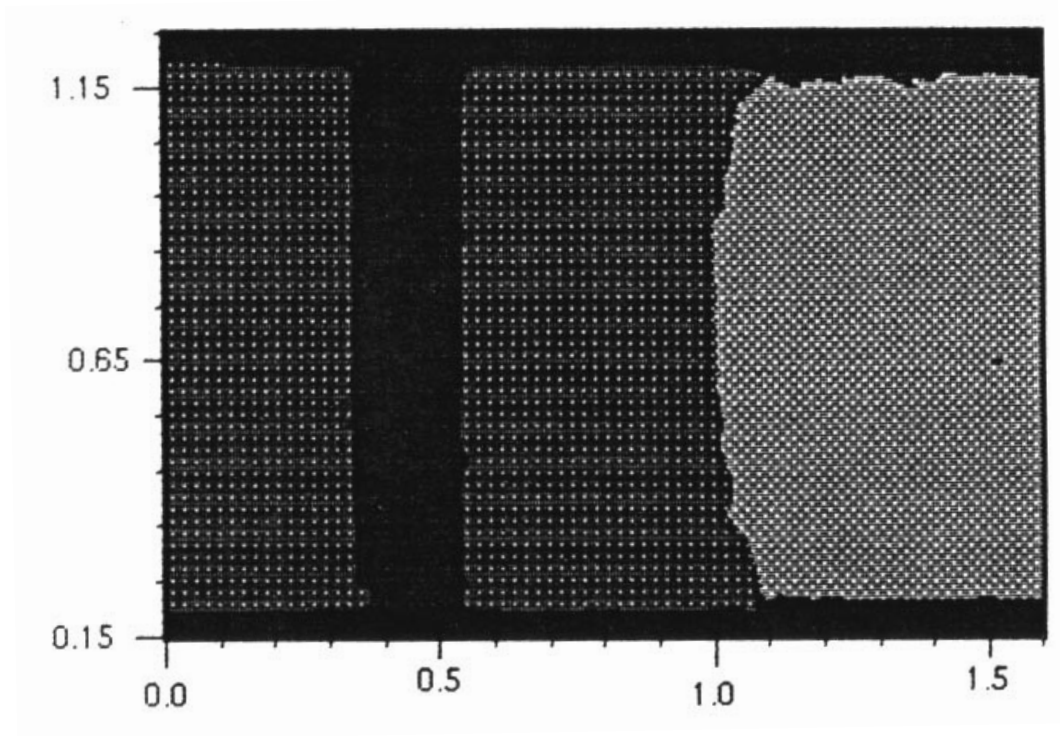


Figure 3-2 C-scan of ENF failure between angle plies [67]

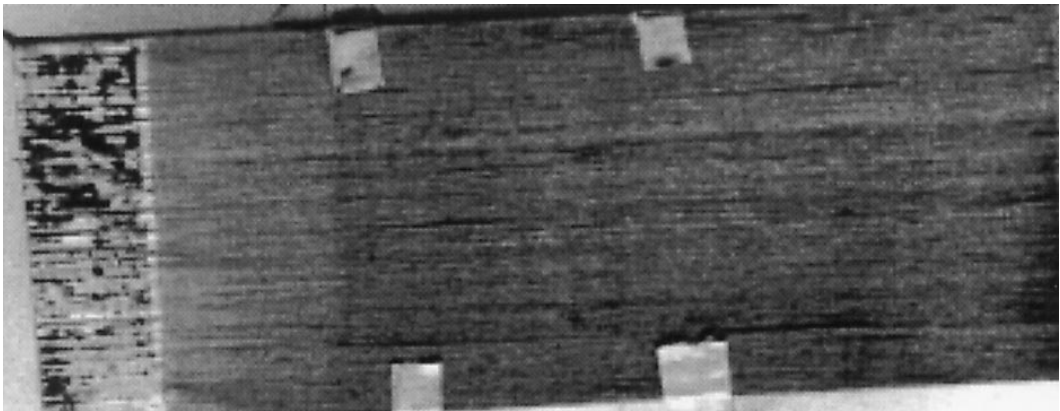


Figure 3-3 curved crack front I DCB specimen after fatigue failure [65].

The observed curved crack front for DCB specimens was attributed to 3D effects at the specimen edge, such as anticlastic bending [64], [68]–[71]. Davidson [63] has found a correlation between the nonlinear decay of energy release rates close to the specimen edge, and the nonlinear factor D_c . D_c characterizes the difference between the plane stress and plane strain flexural rigidities. It is defined as one minus the ratio of plane strain to plane stress rigidities [66].

$$D_c = 1 - \frac{D_{11}D_{22} - D_{12}^2}{D_{11}D_{22}} = \frac{D_{12}^2}{D_{11}D_{22}} \quad 4.1$$

Where D_{11} , D_{22} and D_{12} are components from the bending stiffness D matrix calculated using Classical Lamination Theory (CLT) for a specially orthotropic laminated material [72]. The general form for the bending stiffness coefficients is given as:

$$D_{ij} = \frac{1}{3} \sum_{k=1}^N (\overline{Q}_{ij})_k (Z_k^3 - Z_{k-1}^3) \quad 4.2$$

Where \overline{Q}_{ij} is the transformed reduced stiffness coefficient, and Z_k^3 is the cube of the distance from the mid-plane to the bottom of the k^{th} layer. For unidirectional laminates, the transformed reduced stiffness is the same as the reduced stiffness. However, for isotropic materials, the coefficient D_c reduces to ν^2 where ν is the material's Poisson's ratio.

Shokrieh et al [73] have investigated different data reduction methods for calculating the corresponding energy release rate of a DCB specimen. In other work Shokrieh [74] studied the effect of the crack length to specimen width ratio on the non-linear strain energy release rate across the specimen width for straight crack fronts. They

characterized it using a factor β . However, their work did not include any NDT tests or testing methods. It also did not involve calculating the corresponding strain energy release rate distribution across the width of the specimen for a curved crack front. This work also briefly discusses the different methods of data reduction for both experimental and numerical models. They confirm that using the modified or compensated data reduction methods for the experimental procedure, will result in a value close to that calculated for the middle section of the specimen width using FEM models. Also, using non-compensated data reduction methods, like Euler-Bernoulli beam equation, will result in a value close to that of the average of the SERR across the whole width.

Budzik et al [68] have investigated the effect of crack front curvature on the resulting SERR across the specimen width for Single Cantilever Beam (SCB) specimens. They have observed that for SCB specimens made from isotropic materials and bonded with isotropic adhesive, the crack propagates to a curved shape from the onset of crack growth. They have modeled the curved crack front and demonstrated the different SERR distribution across the specimen width between the straight and the curved crack front. However, they did not study the curved crack front for symmetric DCB specimens. Nor they studied the behavior of composite materials. It is also unclear whether they used an orthogonal mesh for the curved crack front models.

Budzik et al have also showed both analytically and numerically that for SCB and non-symmetric DCB specimens. The fracture is in fact a mixed mode fracture with contributions from both Mode II and Mode III fracture modes. This is due to the significant contribution of the shear and transverse stresses to the total stress field at each point across the crack front. It is worth noting that this mode mix observed, is only evident in SCP specimens, or non-symmetric DCB specimens. Symmetric DCB specimens fail under pure mode I, even when accounting for the curved crack front. This is due to the

self-similar characteristic of symmetric DCB specimens, which result in almost zero shear and transverse forces (ones responsible for mode II and mode III fracture modes), as well as negligible deformations in the axial and transverse directions in the area surrounding the crack front.

R. Krueger [24], [70], [75]–[77] has intensively investigated numerical modeling of fractures in composite laminates using Finite Element Method, including DCB specimens. To better capture the non-linear decay of the strain energy release rates close to the specimen edge, Krueger used a refined mesh near the edges of the specimen [67]. Several element types were investigated by Krueger and Geotze as well [77]. They demonstrated that eight noded brick elements with incompatible modes (C3D8I) produce results equivalent to those obtained when using a 20 node, 2nd order, non-linear brick elements (C3D20), or a 20 node 2nd order reduced integration brick elements (C3D20R).

Chapter 4
In-situ X-ray System
System Design

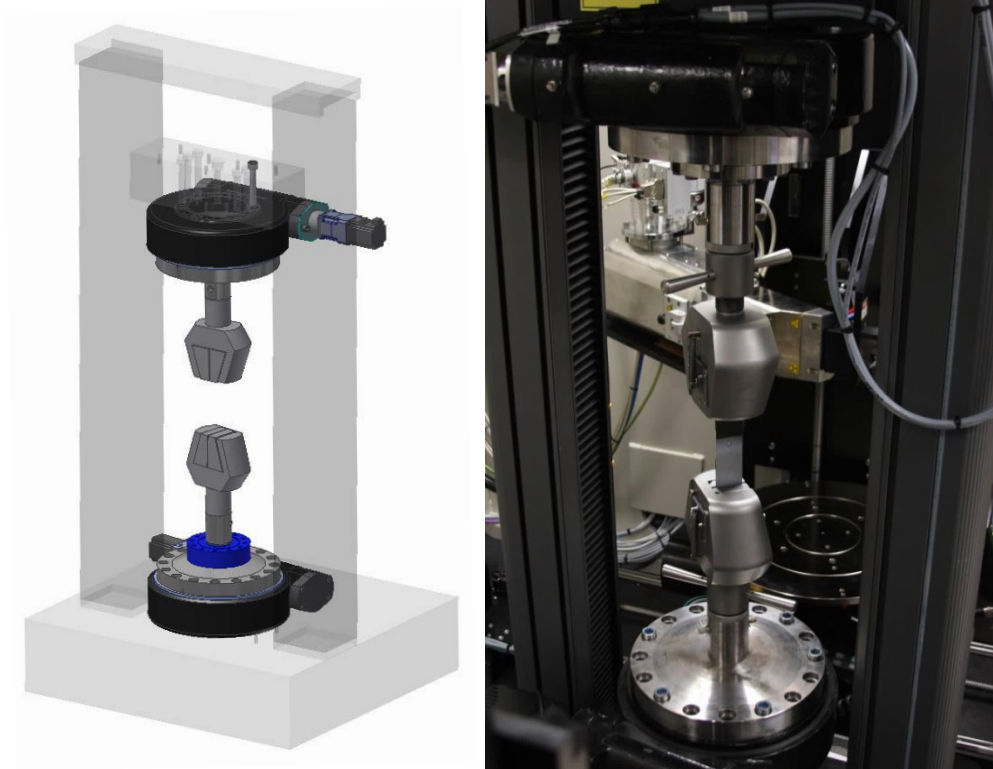


Figure 4-1 Computer representation, and a picture of the in-situ system

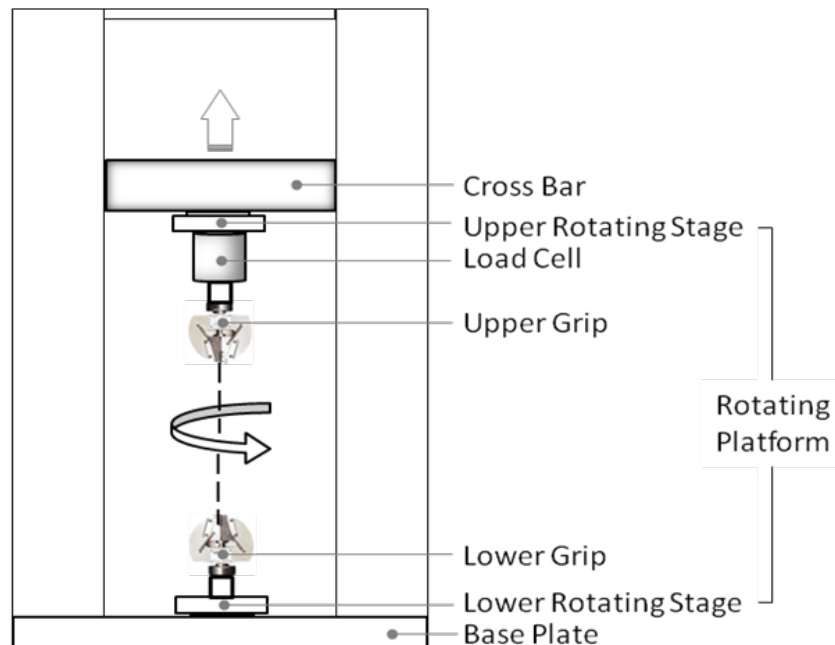


Figure 4-2 Conceptual drawing for the proposed device [78]

In order to avoid the limitations of current systems, as well as allowing for more general use of the developed system, a standard load frame, modified to allow for CT while loading the specimen is devised. A conceptual drawing for the proposed system is shown in Figure 4-2 [78]. As illustrated, the specimen is suspended between the grips, which are mounted on two rotating stages moving synchronously to allow for computed tomography projections to be recorded. This allows for simultaneous loading and rotation of the specimen. Also, since the actuation of each rotation stage is independent of the other, the machine can also be used to apply torsional loads on the specimen. This can be achieved by offsetting the rotation stages from each other by the required torque / angle, then synchronizing them together to allow for CT scans.

The final design is as follows. The load frame is a modified Instron 5969 load frame [79]. Two hourglass, worm, slew drives were added to the top and the bottom of the machine. The drives are SE9C-61M-24H01-RC, 9 inch standard slew drives, with 61:1 ratio, and 40% efficiency, purchased from Kinematics engineering [80]. They have shoulder bearings that can withstand up to 80.99 kN (18207.28 lbf) dynamic axial load, and 337.44 kN (75859.53 lbf) static axial load.

The slew drives have an input torque gain of 10 in-lb when subjected to 10,000 lb of compressive loading. This was validated experimentally as follows. The test setup was composed of three components thrust bearings, a loading plate and the slew drive. First, the friction in the thrust bearings under a 10,000 lb compression load was calculated. This was done by aligning two thrust bearings together so that their axis of rotation are aligned, then setting them up in a standard test machine. The machine was then actuated until 10,000 lb of compressive force was achieved. While the thrust bearings were loaded, a torque meter was used to calculate the torque required to rotate the middle races (the ones free to move) of the thrust bearings. The resistance of the bearings to rotate while under 10,000 lb compressive load was found to be smaller than the smallest reading on the used torque meter, which means that it is less than one ounce-inch of torque. With that result, testing of the increase in input torque for the slew drives due to 10,000 lb compressive load proceeded. The slew drive was put in the machine between the moving cross-head and the stationary bottom, with the rotating gear facing upward. Then a steel plate was put on top of the gear race, and the thrust bearings between the steel plate and the loading nose. Care was taken to align the center of rotation of the thrust bearings, and that of the slew drive gear. While the setup is not loaded, the torque on the input shaft to the worm gear was measured. Then, the assembly was loaded to 10,000 lb. The input torque to the worm gear was measured again. The difference

between both input torques measured, is the amount of extra input torque required due to the 10,000 lb load. This was found to be 10 inch-pound. It is worth noting that this figure could even be smaller in reality, if a special alignment fixture was used to align the gear with the thrust bearings axis of rotation. However, since the purpose of this experiment is was to determine the required input torque for the slew drives under maximum operating conditions, further refinement of the testing method and the experimental setup were deemed unnecessary since the current results were conclusive enough to size the motors required for our application.

Using the results from the previous experiment, Mitsubishi HF-KP23K servo motors and Apex-Dynamics AB060-005-S2-P2 planetary reduction gearboxes, were selected to actuate the slew drives. The motors have a rated torque of 0.64 N.m. and speed of 3000 rpm, which adds up to a rated power of about 200 Watts. The motors also have an 18bit (262,144 p/rev) encoder for speed and position measurement [81]. Also, in order to protect the motors from excessive loads, servo controllers with over-load protection circuits are used. In collaboration with North Star Imaging, a specially modified version of the CT scanner control software (efx-dr) has been developed to allow for control of the rotation of the two motors from the same interface that controls the rest of the X5000 machine functions. This streamlined the process of integration of the rotational stages with the CT software.

The Apex-Dynamics gearboxes are a single stage, 5:1 ratio, 97% efficient, keyed planetary gearboxes. A small shaft coupling was manufactured to act as an adapter between the gearbox output shaft and the slew drive input. Six extra, oversized, holes were machined in the cross head in order to affix the top slew drive to the moving cross head.

Adapters manufactured from high-strength low-alloy 4140 steel were designed to fit all parts together. A finite element analysis was made on the designed parts that are in the load path. The result of the analysis is shown in Figure X. The parts had a maximum deflection of 0.007 mm and 0.01 mm respectively, under 11,000 lbf. After the parts were machined, they were then heat treated to increase the hardness, decrease the maximum deflection and increase the wear life of the parts. All machined parts had a fine finished locating surfaces to ensure proper alignment of all the stages together.

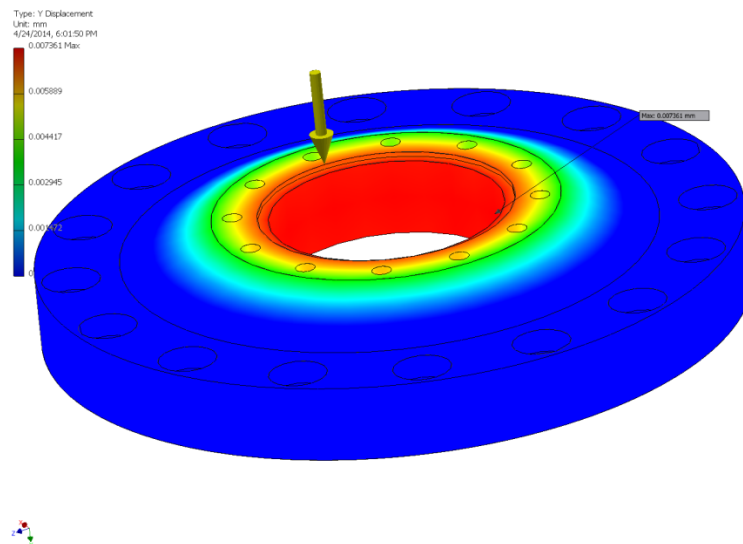


Figure 4-3 FEM analysis showing maximum deflection of the Load Cell attachment

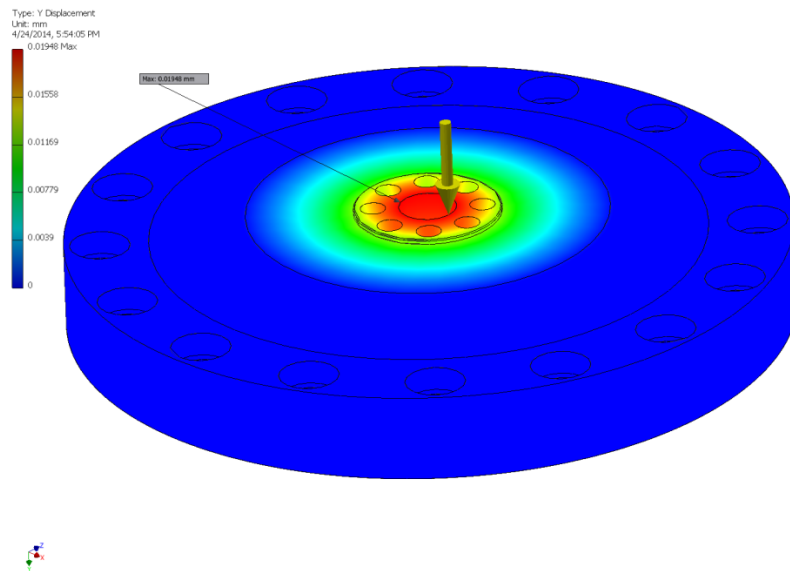


Figure 4-4 FEM analysis showing maximum deflection of the Top grip attachment

After the heat treatment process, most parts were re-checked and in few cases re-machined to fix and hole size changes, or warping resulting from the heat-treatment process. Also, to improve the alignment of the slew drives, both the top and bottom surfaces of each drive gear had their paint stripped chemically, then the loading surfaces for each drive were milled to ensure flatness and parallelism. Also, in order to allow for free movement of the top gear box during the alignment process, two hardened and finely ground steel sheets are used as bearing surfaces between the bolts and the cross-head top surface. This allows for ease of positioning while aligning the machine.

To be able to detect any rotational miss-alignment of the top and bottom rotation stages, as well as measure the torque exerted on the specimen if tension-torsion or compression torsion testing is required. An InterfaceTM tension-torsion 10,000/6,000 lb load cell [82] was used as a replacement for the original stock, single axis, load cell. This allows us to monitor the torques exerted on the specimen in real time, during installation,

loading and the scanning phases, and to adjust for any twist offsets that might occur. Special 15 foot load cell cables were purchased to accommodate any of the machine's configurations. Also, several adapters were designed and manufactured in order to allow for interfacing the new load cell with the machine's standard wedge grips.

To achieve maximum possible magnification, modifications to the X5000 machine had to be made. The x-ray tube support structure was replaced with one that allows for horizontal movement. This allows us to get the tube as close as possible to the scanned object, achieving similar magnifications to scans made using the original machine turn table. This allows us to observe damage with a micron level magnification.

System Configurations

The machine is designed to have two different configurations. One with the load cell below the bottom gear train, and one with the load cell above it. First the slew drives are attached to the machine using the appropriate attachment parts. Then, using a 0.015 inch dial indicator with a magnetic base, the slew drive adapters are aligned with the slew drive gear in order to eliminate any rotational eccentricities. The process is an iterative process that involves rotating the gear, then moving the adapter plate according to the indication on the dial indicator to minimize the misalignment, then repeating until we have the least misalignment possible. Once both adapters are properly aligned with their respective drives, the top assembly is aligned with the bottom assembly using a combination of a machined steel rod (Figure 4-6) and a steel shaft collar.

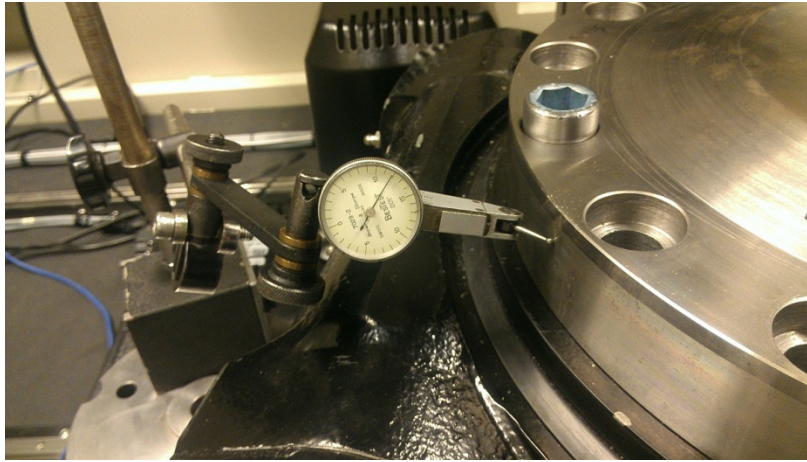


Figure 4-5 Aligning the bottom adapter using the dial indicator

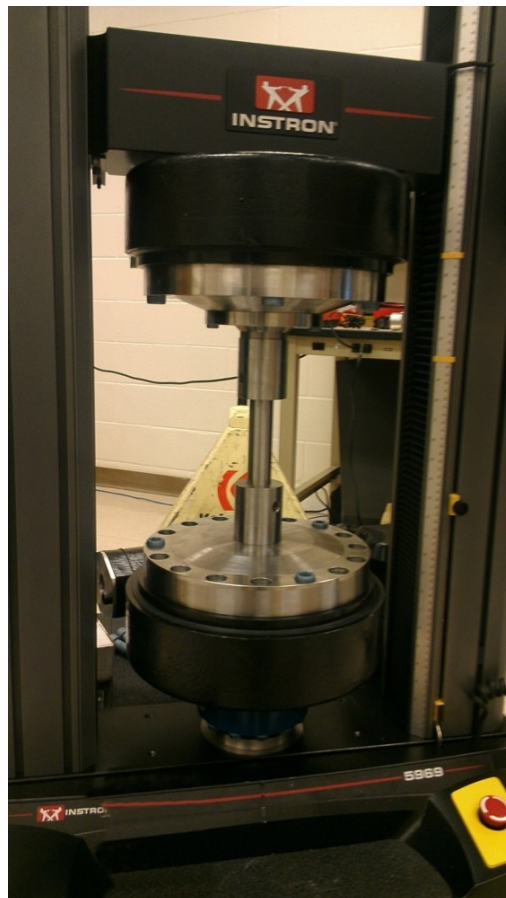


Figure 4-6 Using a steel rod to align the top and bottom drives

For convenience, the configuration with the load cell on the bottom is preferred because it eliminates cable winding issues. However, that resulted in large load measurement offsets and fluctuations while the machine rotates. When the load cell was moved to the top of the gear train, loads were more stable, and fluctuations were significantly smaller. The figures below show a comparison between torque value fluctuations in inch-pound vs time when the load cell is on the bottom, and when it is on the top, for the same specimen. The torques fluctuate a maximum of 60 in-lb when the load cell is on the bottom. And they fluctuate a maximum of 7 in-lb when the load cell is on the top. That is a 750% decrease in fluctuation magnitude.

A possible reason for the higher torque fluctuation magnitude when the load cell is placed on the bottom, is due to the lack of concentricity of the load cell with the line of action of the force. Another possible reason, is the fact that when the load cell is on the bottom, the total support structure for the bottom slew drive is weak, giving way for higher amplitude vibrations when rotating, that, in turn, is erroneously registered as extra torque by the load cell.

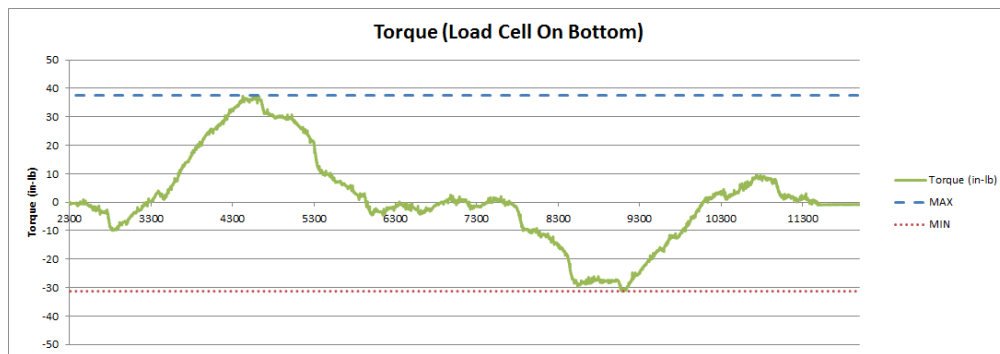


Figure 4-7 Torque fluctuations as the machine rotates, specimen I

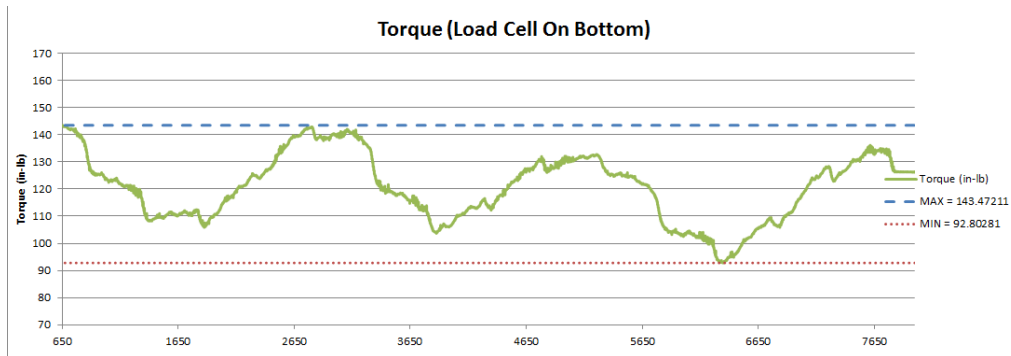


Figure 4-8 Torque fluctuations as the machine rotates, specimen II

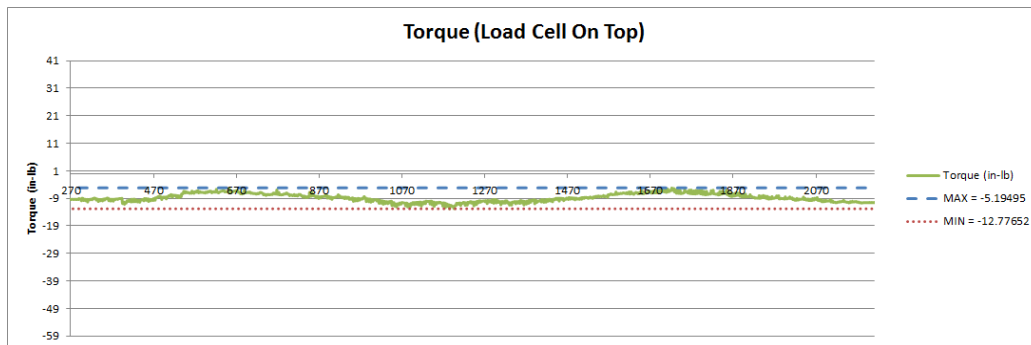


Figure 4-9 Torque fluctuations as the machine rotates, specimen I

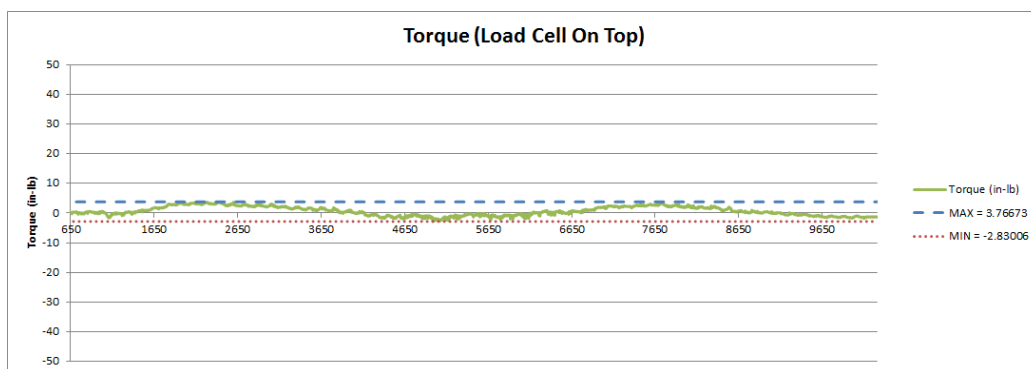


Figure 4-10 Torque fluctuations as the machine rotates, specimen II

Because it was suspected that the slew drive surfaces did not have proper alignment. They were taken out of the machine, and machined to within 0.002 inch of misalignment. This improved the alignment of the machine dramatically. The change in percent bending during machine rotation was calculated according to the guidelines outlined in ASTM standard E1012-12 for test frame alignment [83]. The percent bending is the ratio of bending strain to axial strain of the specimen. The standard tests for two types of test machine misalignment, the concentric misalignment between the top and the bottom fixtures of the machine, and the angular misalignment.

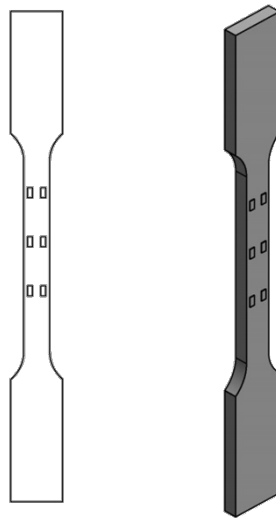


Figure 4-11 Illustration of calibration specimen.

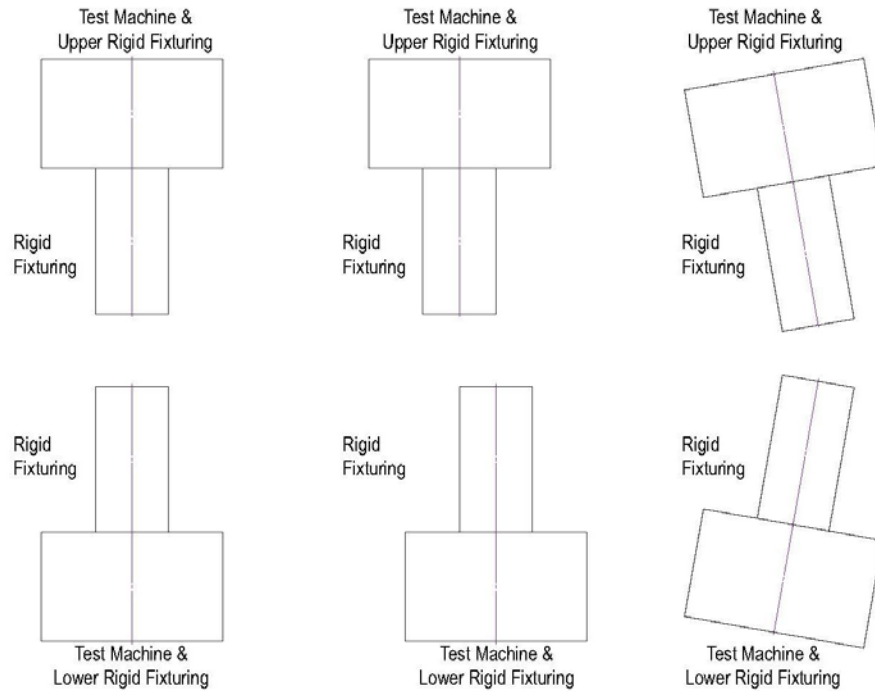


Figure 4-12 Test machine misalignment types, showing the concentric misalignment and the angular misalignment between machine fixtures [83].

A twelve (12) gauge calibration specimen was used to calculate the bending strain and percent bending. The percent bending during a full 360° rotation of the machine was recorded every 1.8° . The percent bending changed only 6.4% during the full rotation of the machine. There was a large constant offset in the reading; however, this is due to calibration specimen misalignment within the grips, and strain gauge equipment reading noise and hysteresis that were noticed during the test. Since the total percent bending fluctuation is less than 8%, this categorizes the machine as classification 8, as per the standard.

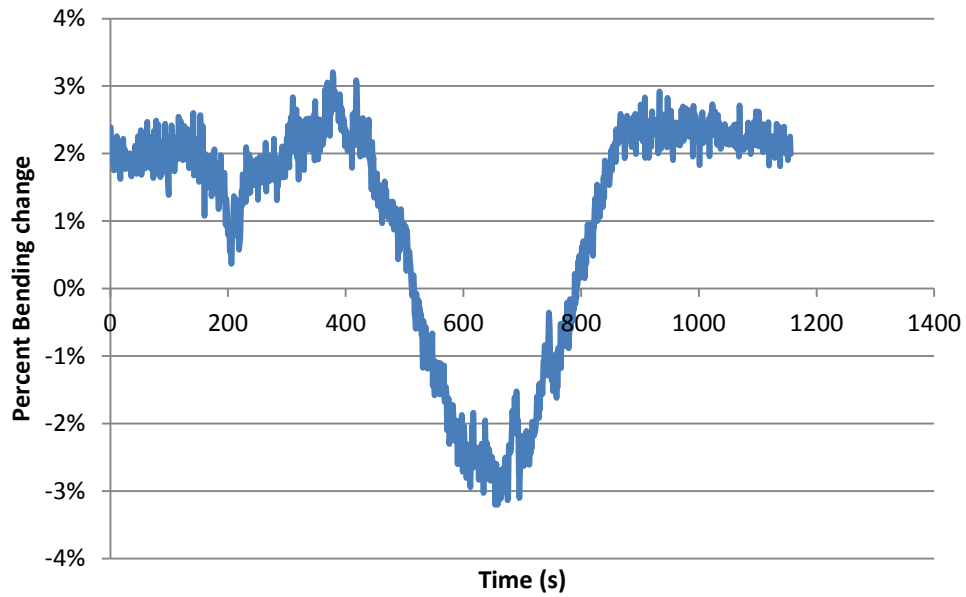


Figure 4-13 Normalized percent bending during a full rotation

To further improve the accuracy of the machine output and minimize errors. For tests that required smaller loads, e.g. the vertical DCB tests, a smaller 200 lb load cell is used to have a much lower reading noise while measuring the small loads associated with DCB test (MAX 20 lb). It was also found that load cell readings vary by about 0.1% of the full scale if the electrical connector that is attached to the load cell is twisted or moved while reading. This would amount for 10 lb in a 10,000 lb load cell. To alleviate that effect, the cables were anchored to the rotation stage, to isolate the load cell connection from the rotation of the machine and hence have a less noisy signal.

Chapter 5

Validation of Current Models

Damage Observation

The developed system is intended for subsurface measurements of composite structures under load. As preliminary work intended to investigate the capabilities of the system, the ability to observe more damage was investigated by scanning the same specimens once under no loading conditions and another under 4500 lbf load and observing the difference. Damaged, 24-ply [0/-45/90/45]S3 IM7/8552 Open Hole Compression (OHC) specimens were scanned and damage was recorded. The figures below show comparisons between section slices obtained for the scanned specimens both with load and without load. It is clear that there is significantly more visible damage the can be observed in the loaded cases versus the un-loaded ones. Some damage is visible in both scans, it is however more pronounced in the loaded scan.

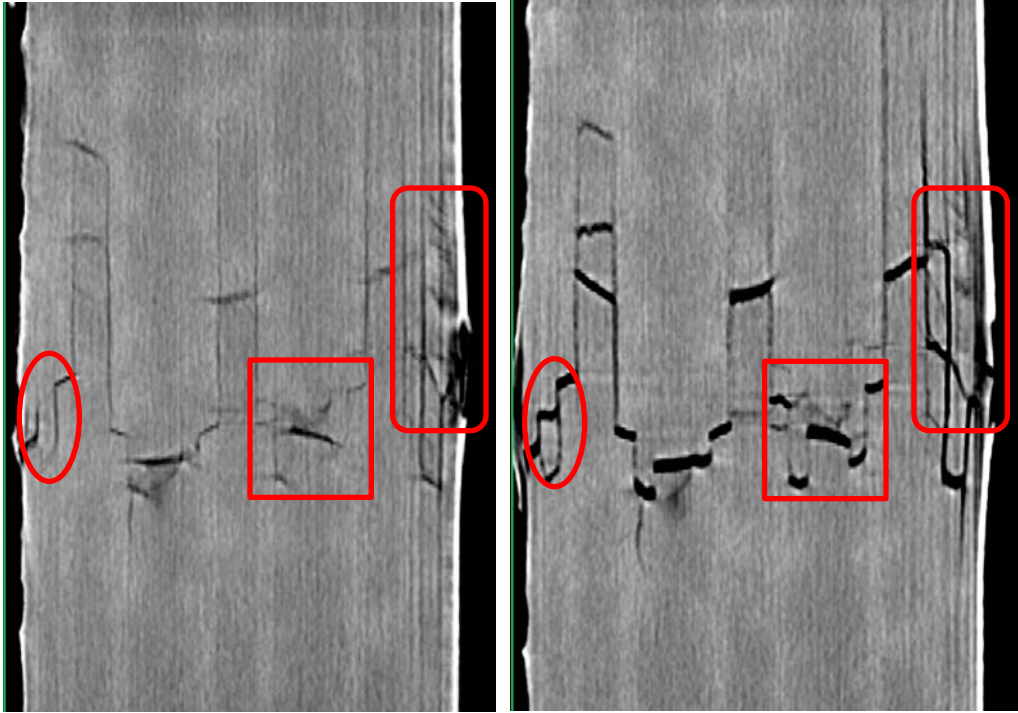


Figure 5-1 Left: no load. Right: 4500 lb tensile load.

The above figure shows a comparison between cross-sectional slices around the hole of two scans of the same quasi isotropic OHC specimen. This specimen was damaged previously under a load of 9,500 lb (42.3 kN) [1]. Several of the damage mechanisms in the specimen are visible in the un-loaded case. However, the loaded CT scan, shows clearly several new damage mechanisms that were not visible in the unloaded case. Like the matrix cracks in the 45° plies on the left side of the specimen (oval shape). In the middle of the specimen, delaminations and matrix cracks were not visible in the un-loaded scan. Also, towards the right edge of the specimen, the complex combination of damage mechanisms was significantly undermined in the un-loaded scan, not showing several of the cracks and delaminations that are present in the specimen.

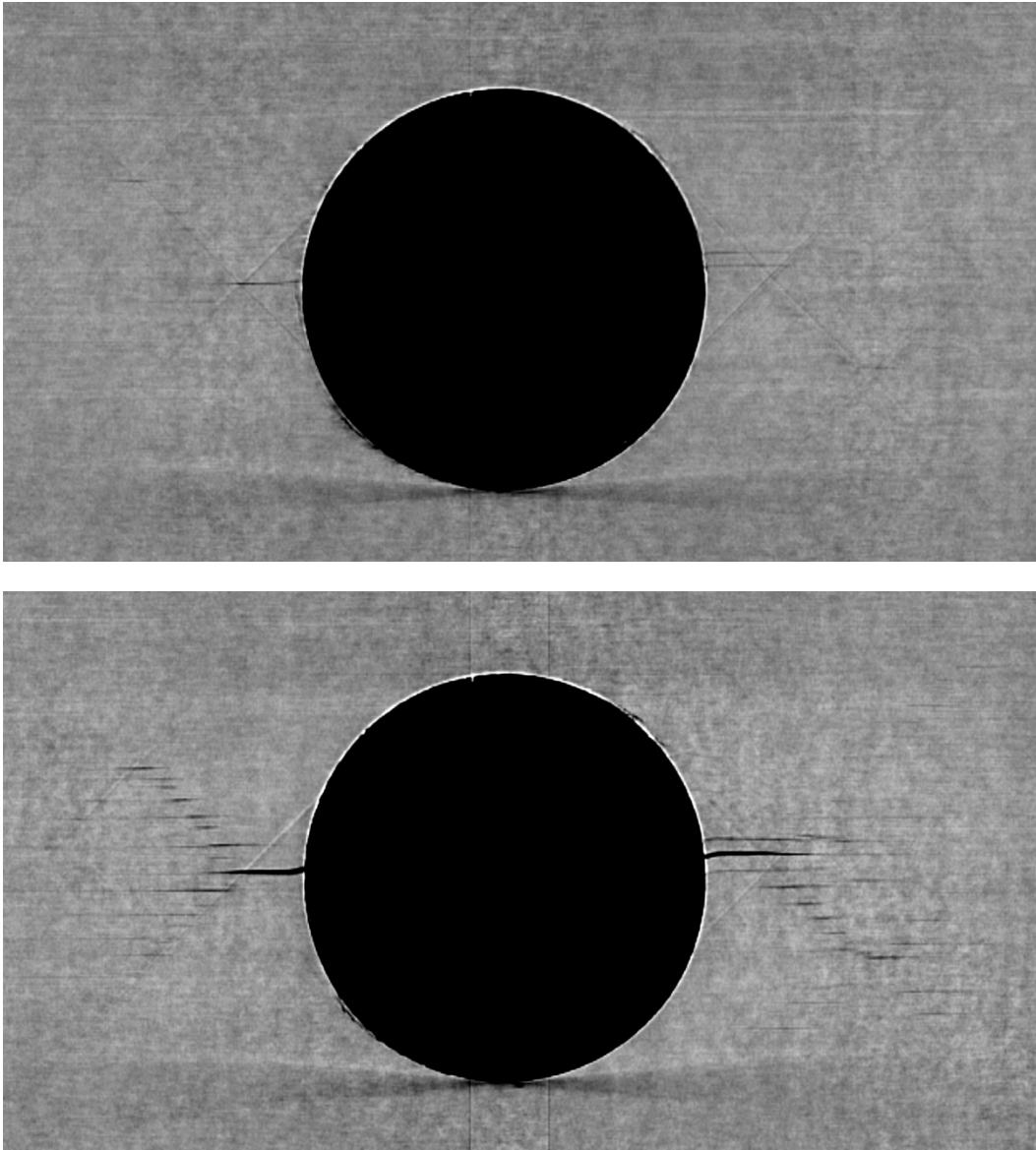


Figure 5-2 Top: no load showing little damage. Bottom: 4500 lb tensile load showing several matrix cracks.

Figure 5-3 shows a cut through one of the 45° plies. The two matrix cracks on the lower left side of the specimen, were not visible in the scan without load, but are very pronounced in the scan with load.

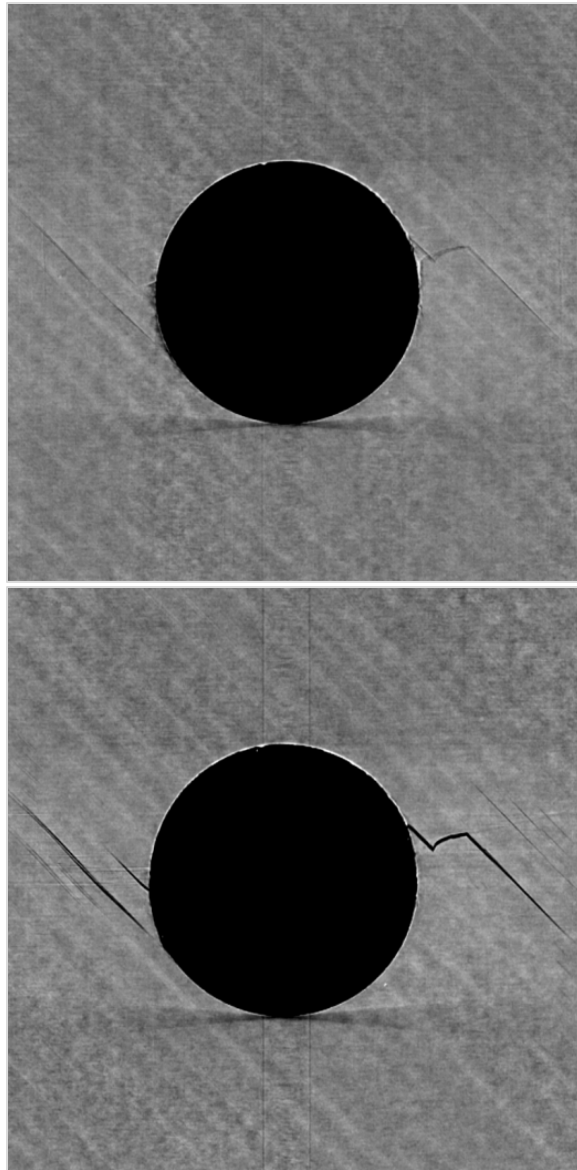


Figure 5-3 Top: no load. Bottom: 4500 lb tensile load showing matrix cracks and fiber breaks.

Another study was conducted to investigate the ability to see, and if possible observe, the progression of a measurable crack opening by going from one load level to another. The scans below show a comparison between the reconstructed images of the

same specimen under two different loads, 4700 lbf and 6520 lbf. The crack opening at the crack tip more than doubled with the increase of the load, as shown in Figure 5-4, and almost doubled in the matrix crack shown in Figure 5-5.

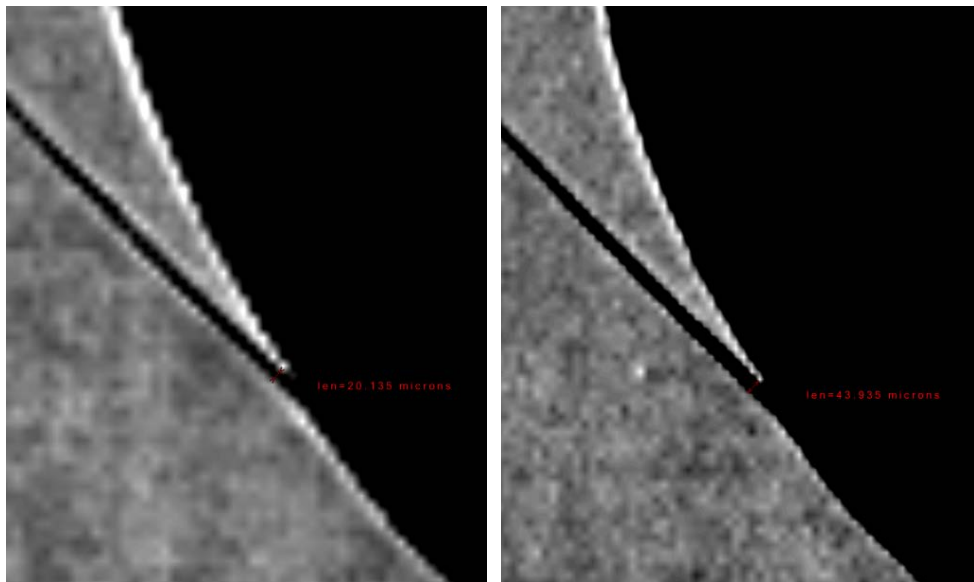


Figure 5-4 Left: specimen under 4700 lbf, crack opening is 20 μm ; Right: specimen under 6520 lbf, crack opening is 44 μm

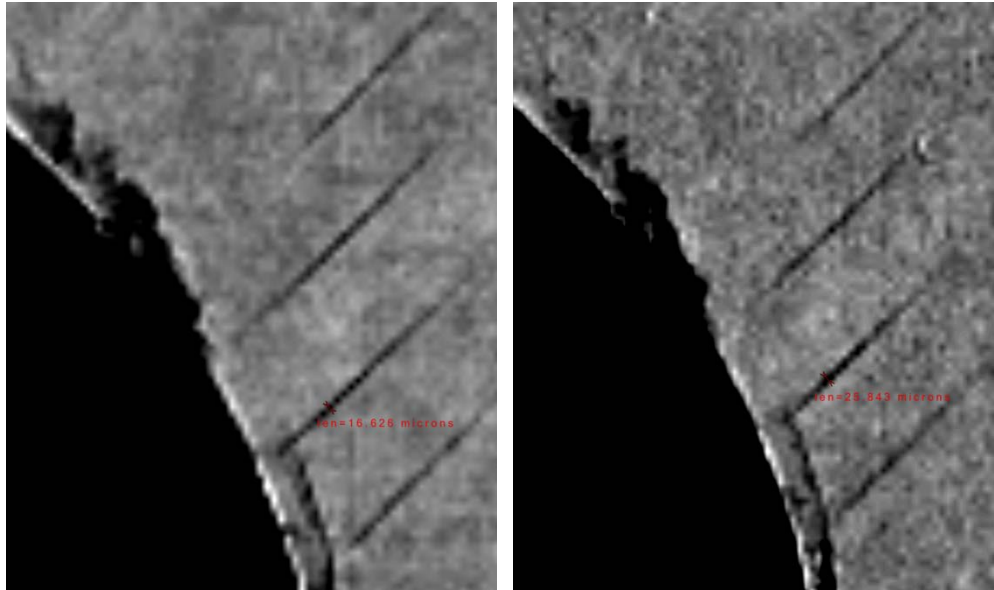


Figure 5-5 Left: specimen under 4700 lbf, crack opening is 16 μm ; Right: specimen under 6520 lbf, crack opening is 25 μm

Validation of Numerical Models

Prediction of Damage in OHC Specimens

Using this methodology, a study comparing the findings of numerical models that predict the damage of Open Hole Compression (OHC) specimens to in-situ x-ray computed tomography scans under load was conducted. First attempts to correlate the Finite element model results, developed by Seon et al [1], with 3D CT reconstructions of the OHC specimens after 10,000 lbf (44.5 kN) compressive loading, seemed to show that the numerical model over-estimated the crack lengths and progression. Also, significant number of matrix cracks that were predicted by the model, did not appear in the scanned part reconstructed volumes. Actually, conventional CT scans only showed fiber failure in the 0° plies and delaminations in the adjacent plies [1], whereas the FE model predicted matrix cracks and delaminations for each laminate ply groups, as shown in Figure 5-6

and Table 5-1. Closer local CT inspections using maximal magnification suggested that cracks were probably present at expected locations, but fracture surfaces “closed up” during unloading of the specimens, preventing successful damage detection in the CT scans [1].

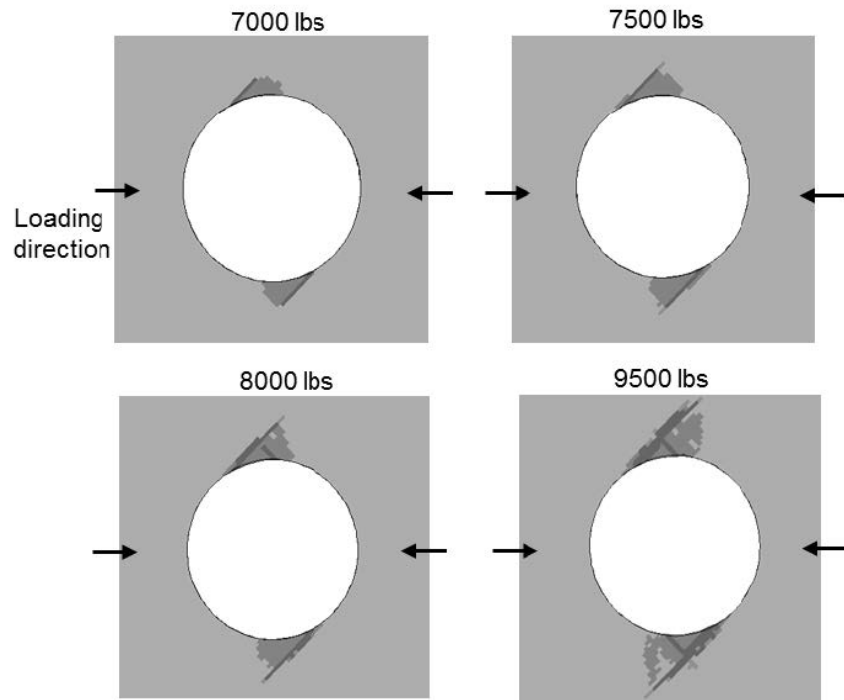
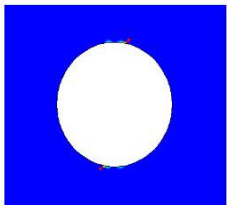
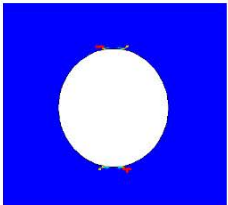
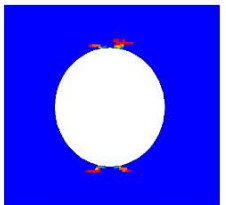
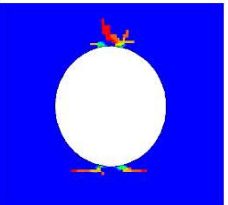
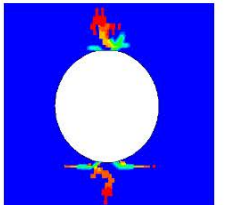
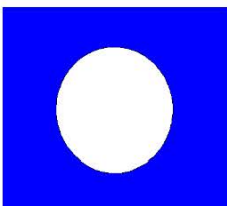
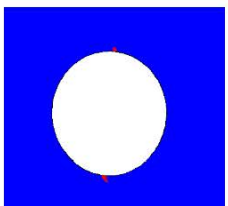
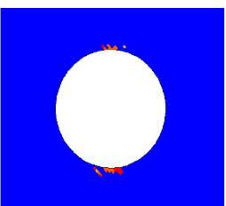
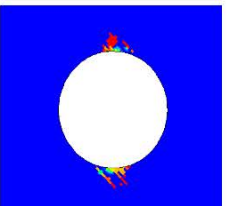
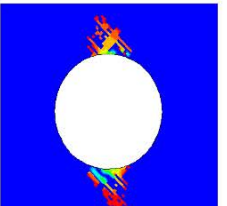
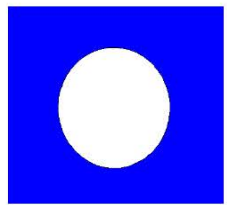
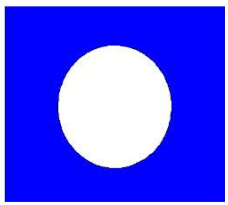
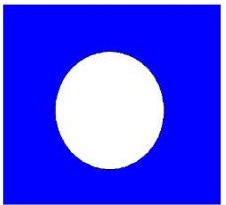
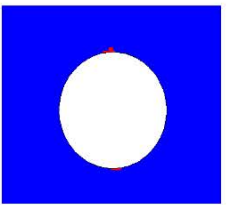
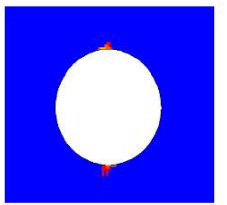


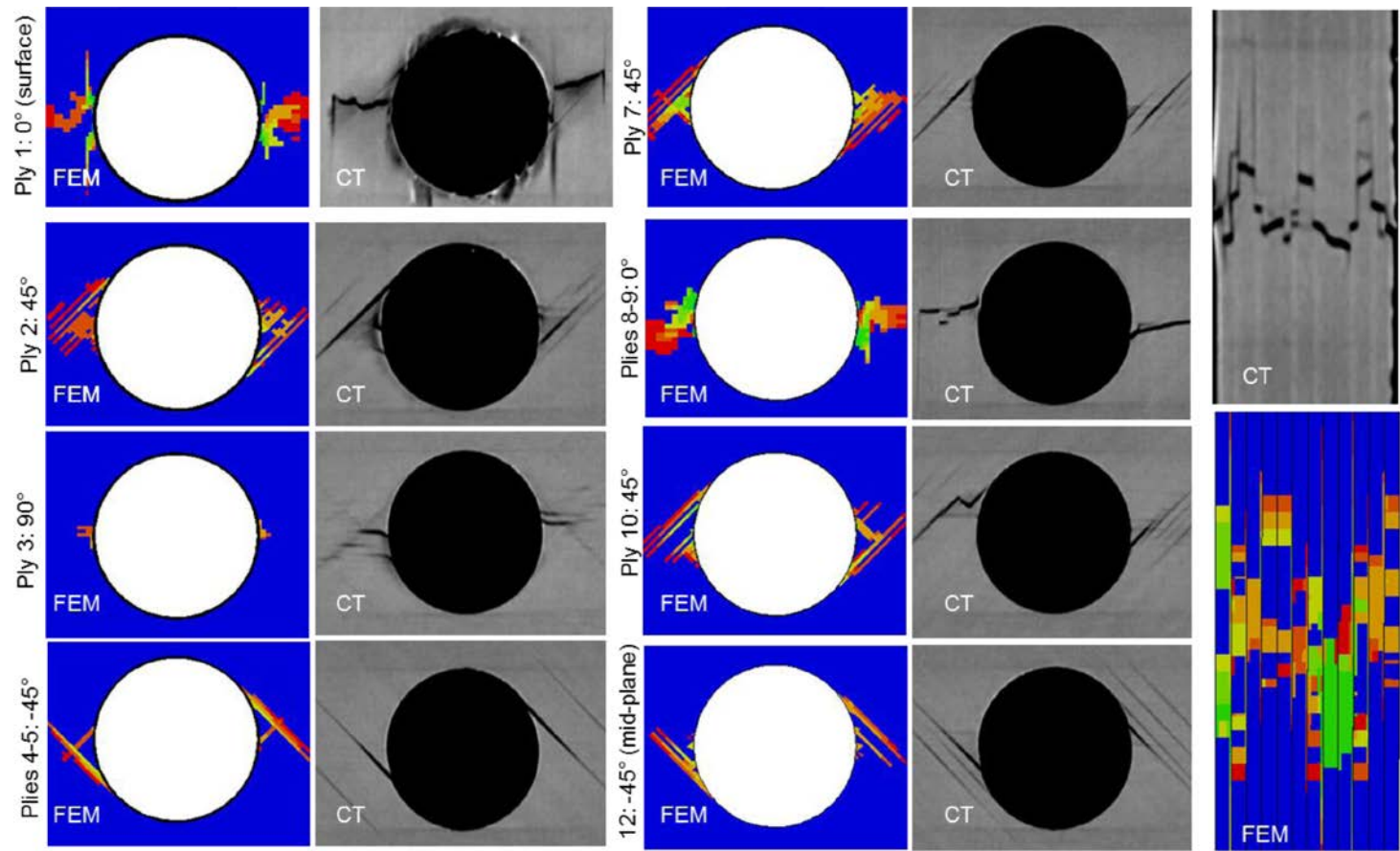
Figure 5-6 Development of matrix cracks (dark grey) and delaminations (lighter grey) in OHC first sub-surface 45° ply [1]

Table 5-1 FE-based simulation of matrix cracks and fiber failure developments in OHC specimens [1]

Compressive load	5000 lbs (22.2 kN)	6000 lbs (26.7 kN)	6600 lbs (29.4 kN)	7800 lbs (34.5 kN)	9500 lbs (42.3 kN)
0° ply (surface ply #1)					
45° ply (ply #10)					
90° ply (ply #10)					
Failure event	Initiation of compressive matrix cracking in 0° plies	Initiation of matrix cracking in 45° plies	Development of compressive fiber failure in 0° plies	Initiation of compressive matrix cracking in 90° plies	Growth of 0° ply fiber failure leading to large element distortion

The experiment procedure was as follows. 24-ply [0/-45/90/45]S3 IM7/8552 OHC coupons were manufactured and tested in quasi-static loading per ASTM D 6484 specifications. The DIC technique was used to monitor surface strains and progression of surface-ply cracks. Quasi-static compressive loading of the specimen was stopped at 10,000 lbs (44.5 kN) when fiber failure in the zero degree surface ply is well developed and visible, but before ultimate structural failure of the laminate. For all the 0° plies, the damage mechanism was a combination of all three main damage mechanisms. We could see fiber breakage, delaminations, and matrix cracks both adjacent and far away from the hole. The dominant failure mode for the 45° plies was matrix cracks, with delaminations noticed in the second ply and fiber breakage in ply 10. The 90° plies failure mechanism was a matrix cracks. Cross sectional slice is shown in the figure as well. It shows that delaminations occurred between almost all plies. This shows an excellent correlation between the Finite Element numerical model and the damage observed in each ply [1].

Table 5-2 Comparison between predicted failure in a 12 ply composite laminate, and scans conducted under load [1].



Investigation of Mode-mixity in OHT Specimens

The system was also used in preliminary work that investigates crack growth in unidirectional open hole tension specimens. The purpose of this work is to investigate mixed-mode failure in composites by calculating the SERR for the different fracture modes and potentially developing a criterion for mode-mixity. Panels were manufactured from 6 ply, unidirectional IM7/8552 carbon-epoxy pre-pregs, rectangular specimens were cut and holes were drilled in the middle according to specified dimensions. Specimens were tested under load and scans were conducted for each crack growth increment. The CT scans clearly show crack fronts developing in a curved shape across the thickness of the specimen.

Finite element models were created to model the damage in each of the specimens for each crack growth increment in order to allow for the measurement of the associated SERR at each of the crack fronts. The figures below show one of the studied specimens, and the corresponding SERR across the specimen thickness for mode I, mode II and mode III fractures.

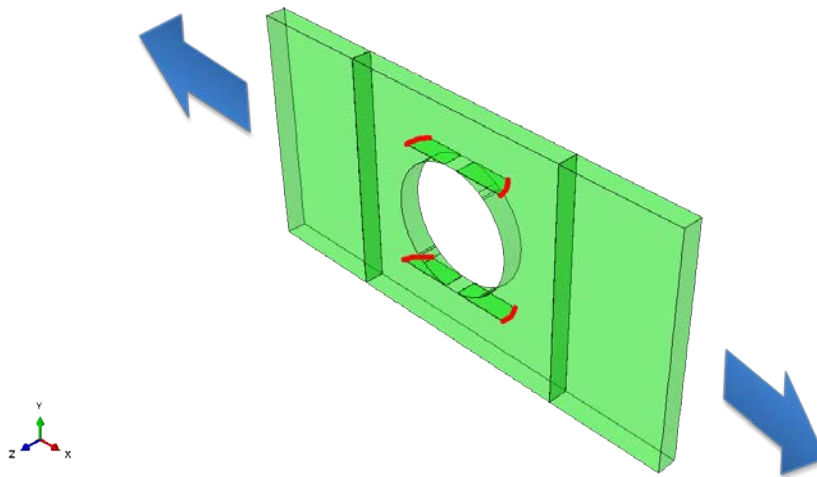


Figure 5-7 FEM model of an open hole tension specimen

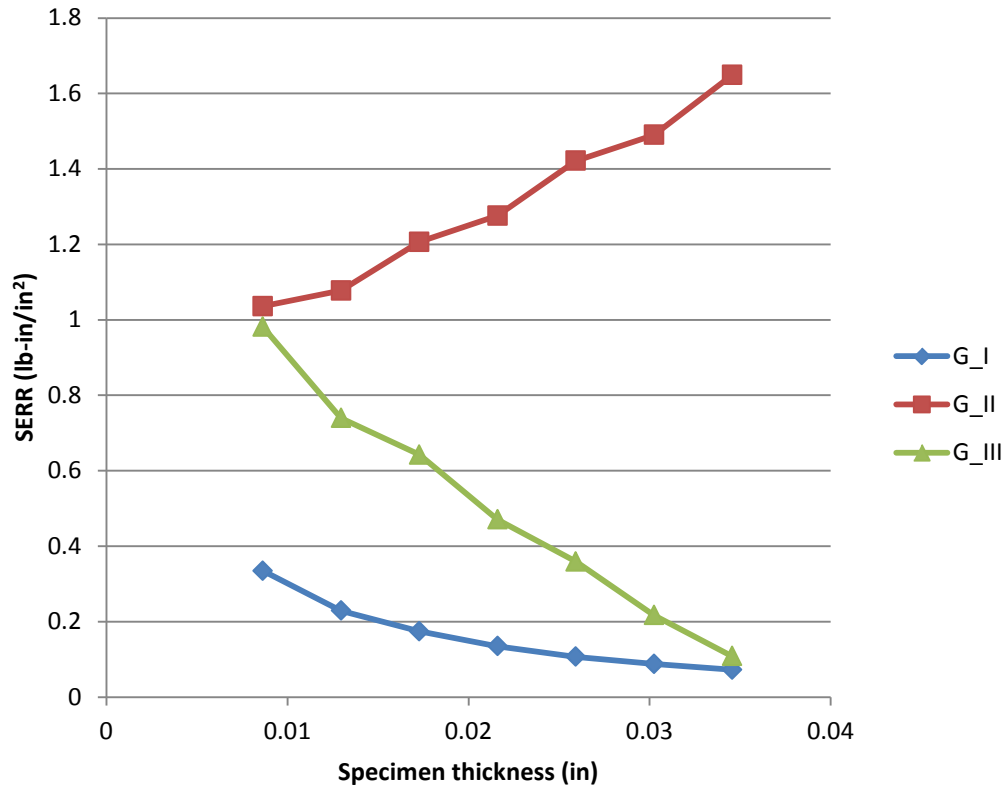


Figure 5-8 GI, GII and GIII for one of the crack fronts in OHT specimen at 660 lb load

As shown in Figure 5-8, it is clear that the SERR for mode I has the least effect on the total SERR across the specimen width. Mode II and mode III energies clearly show the effect of crack front curvature on the value of the SERR calculated for each respective mode. This is because as the crack front curves, the normal and longitudinal shear forces change directions making the SERR for the shear modes (Mode II and mode III) highly dependent on the shape of the curved crack front.

Chapter 6

DCB : Part I Mechanical Testing

Outline

In this and the following sections, standard DCB tests will be conducted as per ASTM D5528 standard. Finite element models will be created to calculate the strain energy release rate in each of the specimens. The critical fracture toughness for the material will be used to validate the experimental and numerical methods. Then, a special fixture specifically designed for special DCB testing in-situ CT scanning is described and used to investigate the progression of failure in DCB specimens. CT scans are conducted to visualize the crack front in the DCB specimens while testing, and finite element models similar to those validated earlier will be used to calculate the energy release rates for the new vertical DCB and the newly observed crack fronts.

Horizontal DCB

Double cantilever beam specimens were manufactured according to the guidelines in ASME D5528-01 [22] from 24 ply, unidirectional S2/E773 Glass-epoxy. The specimen dimensions and picture are shown in Figure 6-2. DCB tests were conducted and test data was recorded according to the procedure outlined in the standard. A 96x Olympus electronic microscope was used to identify the tip of the Teflon insert. The surface after the insert was painted with white paint in order to ease the monitoring of crack progression on the surface of the specimen. Specimens were then pre-cracked, markings for the 50 mm crack length were scribed on the side of the specimens starting from the tip of the pre-crack. The specimens were then loaded at a constant rate of 0.05 inch/min, the load and crack opening displacement (COD) at each of the crack

progression markings was recorded as per the standard. Mode I fracture toughness was then calculated for 5 different specimens using two Different data reduction methods, namely the Modified Beam Theory (MBT) and the Compliance Calibration method (CC), as explained earlier in the background section.

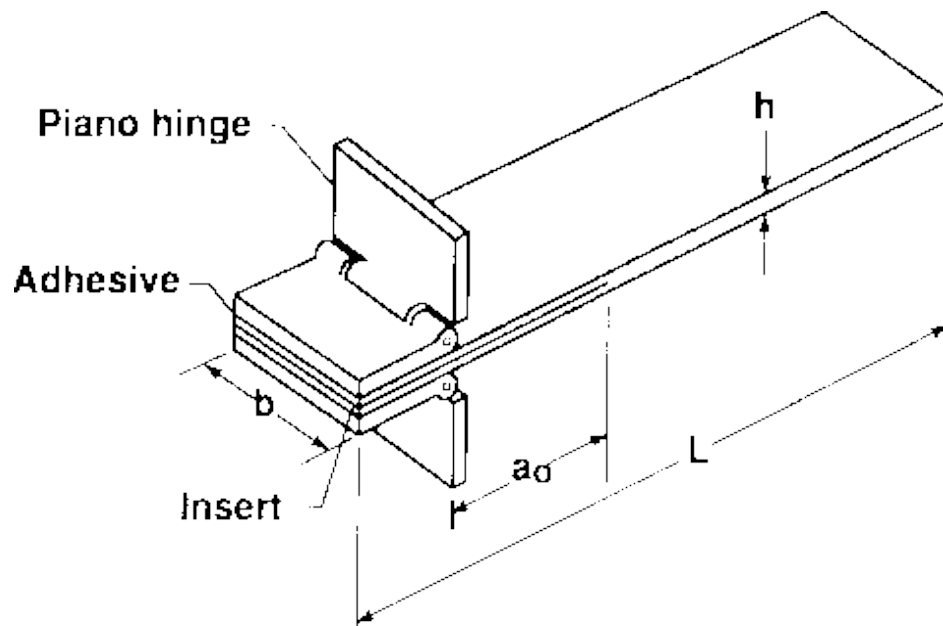


Figure 6-1 DCB specimen with piano hinge

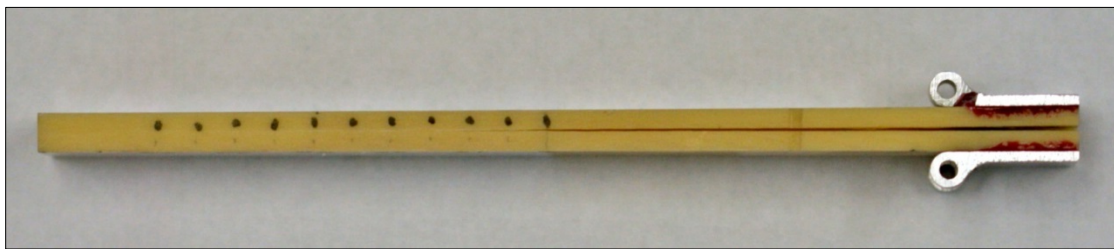
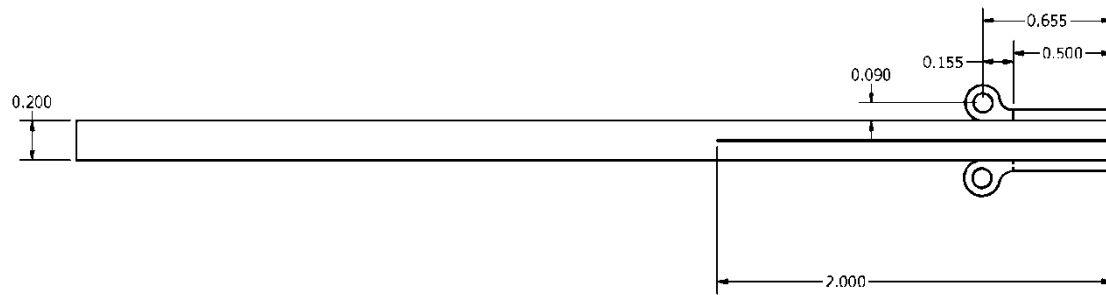


Figure 6-2 DCB specimen Picture and dimensions

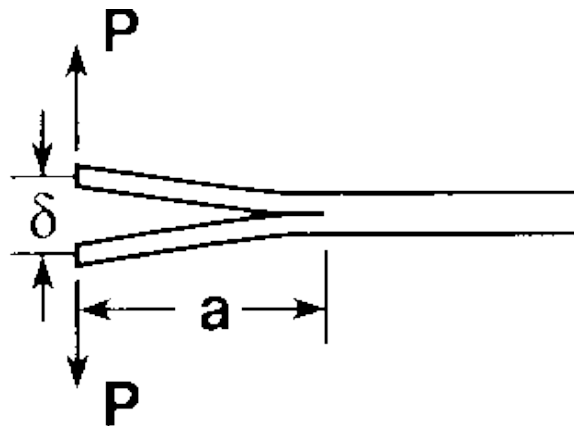


Figure 6-3 DCB Specimen Loading

The scope of DCB testing in this work is to monitor and characterize fracture progression and crack shape in DCB tests. So while the standard DCB test and the associated data reduction techniques are used, the primary focus is not the calculation of

the material's fracture toughness. This work will focus mainly on the numerical methods for calculation of the Strain Energy Release Rates (SERR) and the crack front shape and its effect on the calculated SERR. Any further discussion about fracture toughness and its calculation is for validation purposes only.

Because of the well-known fiber bridging phenomenon in DCB tests of composite materials [22], the critical fracture toughness calculated from the DCB test is taken to be one of three values. The SERR at the non-linearity point, the SERR at the Visual crack point, and the SERR at the 5% point. In most experiments, fracture toughness is taken to be the SERR at the non-linearity point because it produces the most conservative value for fracture toughness, it is also the point with the least parasitic effects on the calculated value. However, some researchers prefer the visual crack point or the 5% point because of because of the micro resin pocket that forms at the Teflon insert tip [16]. The mode I fracture toughness in this study is only calculated in order to compare to other reported values in the literature as well as to validate the current test technique. It is chosen to be the first visual (VIS) crack progression point, after the pre-crack is introduced in the specimen.

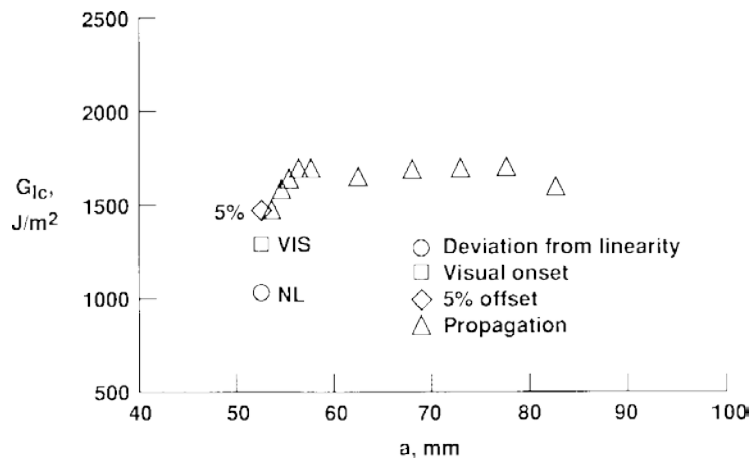


Figure 6-4 R-curve showing the NL, VIS and 5% points [22]

Figure 6-5 shows the plots of the average R-curve (G_I vs crack length) for all five specimens. Mode I fracture toughness for the specimens tested was found to be 0.9 lb-in/in² using MBT and 0.97 lb-in/in² using CC, calculated at the visual pre-crack point. In comparison, Murri et al [84] have calculated the fracture toughness for unidirectional S2/E773 glass-epoxy specimens and found it to be 0.8 lb-in/in² at the deviation from linearity point (NL). This lower value is expected since the NL point produces the most conservative estimation of the fracture toughness [22] and it is 14% smaller than the measured value for the visual pre-crack point, which is expected.

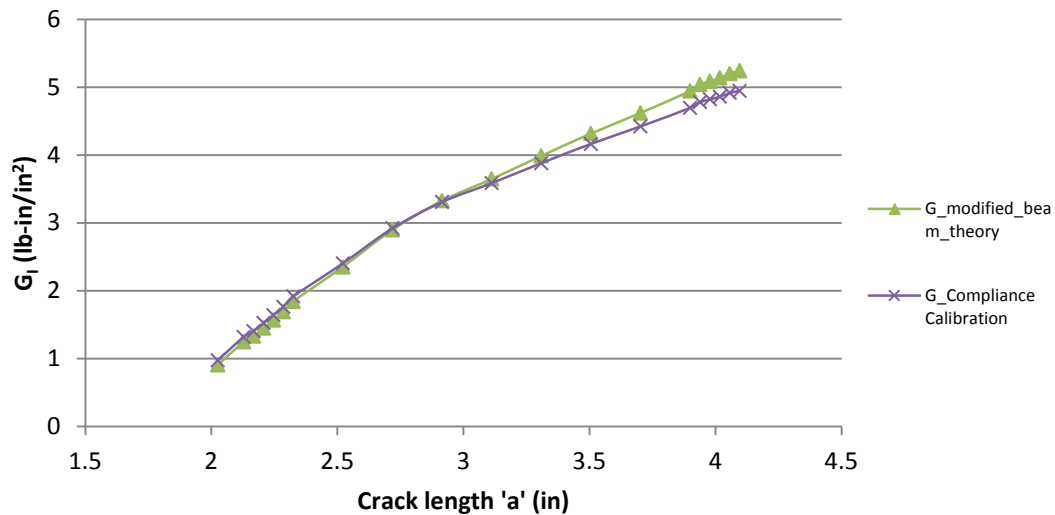


Figure 6-5 Average Fracture Toughness values for S2/E773 Glass-epoxy Composite

Vertical DCB

In order to be able to perform Computed Tomography scans in-situ DCB testing, a special test fixture was developed. The new vertical fixture is shown in the figure below. It has a wedge attached to the machine movable cross-head via a threaded connection, two rigid roller assemblies affixed to the specimen sides, and a bottom holder (inverted

wedge shaped) to provide support for the bottom of the specimen, while allowing for self-alignment once the load is applied.

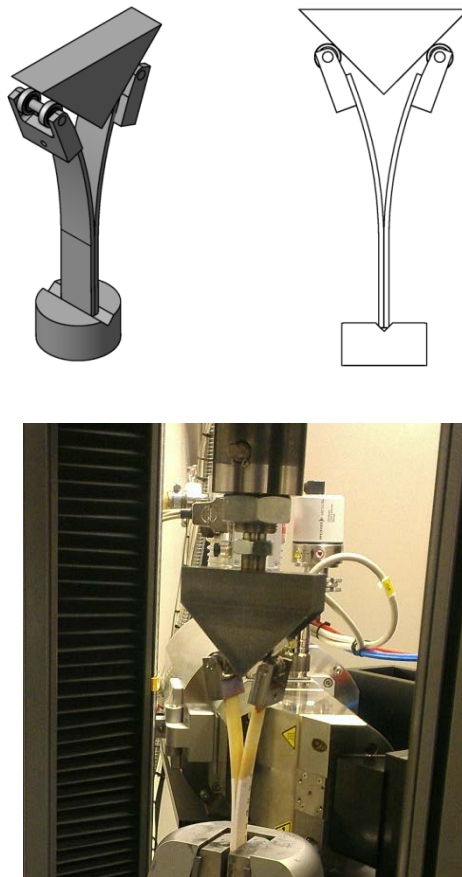


Figure 6-6 Fixture for vertical DCB

Force analysis for the vertical fixture show that there are two force components acting on the specimen loading point, a normal force, and an axial force. The normal forces acting to open the specimen (p_1) are equal to one half of the total applied load by the test machine (P). The axial forces have the same value. The friction forces in the ball

bearing, and between the ball bearing surface and the wedge surface are considered zero and infinity respectively.

$$P = 2R\cos(45)$$

$$R = \frac{P}{2\cos(45)}$$

$$p1 = p2 = R\cos(45) = \frac{P\cos(45)}{2\cos(45)} = \frac{P}{2}$$

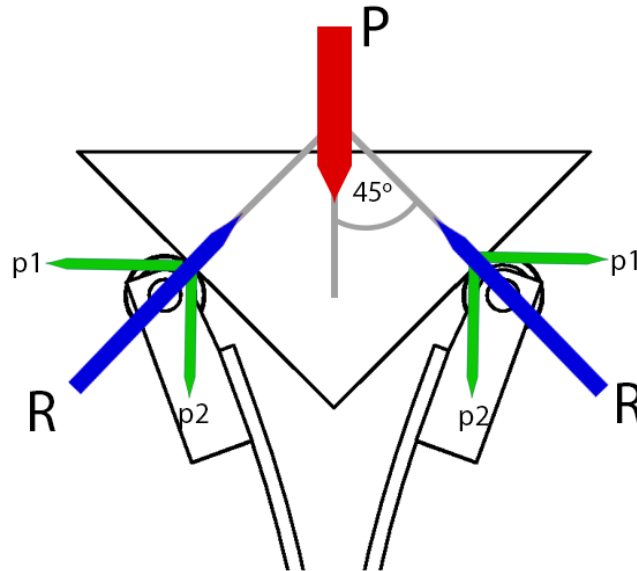


Figure 6-7 Vertical DCB Force Analysis

Finite element models were created to investigate the effect of the axial forces (p2) on the calculated SERR across the width of the specimen. There was a significant difference of 18% decrease in the calculated SERR towards the midpoint of the specimen (Figure 6-8) when neglecting the effect of the axial force p2. It is then determined that

since the purpose of this study is to investigate the effect of crack front shape on the calculated SERR, a comparative study between FEM models for both observed and idealized shapes will be conducted. However, devising a nonlinear model for the calculation of SERR that account for the combined loading at the loading points is beyond the scope of this work. It will also still not be comparable to the values calculated from the standard DCB test due to the miss match in boundary conditions. With that said, no analytical data reduction will be performed on the vertical tests, only finite element models will be developed, analyzed and compared for the different crack front shapes.

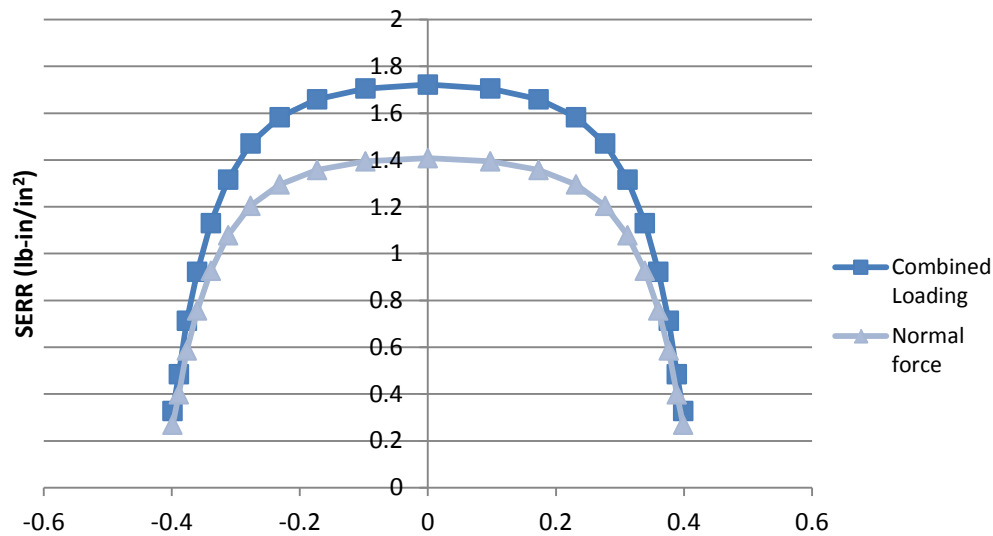


Figure 6-8 FEM of Combined loading vs normal forces for one of the crack increments

Test Procedure

The procedure for the vertical test was similar to the one used for the standard DCB test. The specimens were setup in the machine and loaded at a rate of 0.05 inch/min. Since FEM models require accurate force and deflection inputs, a 16 megapixel, Prosilica GE 4900 digital camera, with a resolution of 4872x3248 pixels.

Equipped with a Sigma 180mm macro lens, was used to capture the specimen deformations at the different crack lengths. The effect of lens distortion on the measured dimensions, as well as the difference in depth between the different features of the specimen is considered negligible in comparison to the measured dimensions (inches). This data was post processed later using computer CAD software to measure the crack opening at each crack length increment.

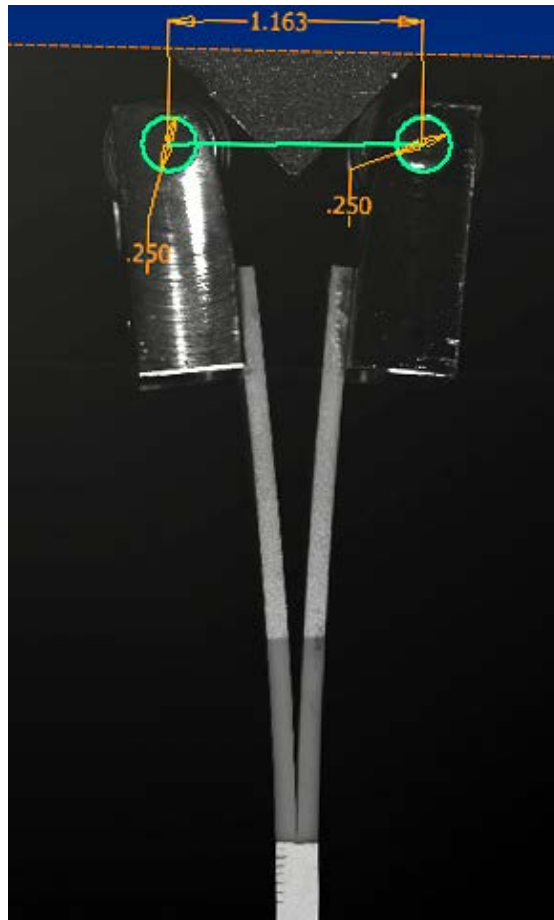


Figure 6-9 Example of measuring specimen deformation using DIC camera and computer software.

CT scan Technique

After loading the specimen in the fixture, the test would proceed and at every 5mm crack growth increment, the test would be paused, and a CT scan of the specimen is taken. This process was repeated 10 times, for all crack lengths. Also two more scans of the specimen were conducted, one before any testing took place, in order to determine whether there are any defects in the specimens. Another scan was taken after the visible pre-crack.

Several ct-scan techniques were investigated to find the technique that yields acceptable results for crack identification and characterization, while taking the least scan time. The output power, geometric magnification, pixel binning, number of projections and projection angle were all varied. A 29 W (73 Kv & 400 micro Amp) technique with 3.5 frames per second, 360 projections over 360 degrees and 6.59 x geometric magnification was devised. This resulted in a voxel size (volumetric pixel) of 19.3 microns (0.00075 in), and a scan time of 19 minutes. The lower magnification was used to allow for visibility of the whole region of interest (the 50 mm crack propagation region) and allowed for shorter source-to-detector distance which in turn enabled the use of higher frame rates due to the higher x-ray intensity at the detector surface.

All scans were reconstructed using filtered back-projection techniques, generating 3D volumetric representation for each 5mm crack growth in the specimen. To find the precise location of the crack front, the histogram viewable band of grey values, cutting plane depth, and the cutting plane yaw and pitch angles were all manipulated until the lowest crack front is visible. This is taken as the preliminary crack front. The preliminary crack front is then adjusted based on the location of the visible crack front acquired from the high resolution camera images. The preliminary crack front would be

adjusted in the vertical direction until the edge of the crack front curve matches the measurement from the camera.

The location of the tip of the Teflon insert was used as a reference for measurement of the crack length for each scan. The insert offset from the edge of the reconstructed volume was measured in the pre-crack scan. Then this distance was used in consecutive scans to calculate the actual crack length. Figure 6-11 shows a 2D slice from one of the reconstructed volumes showing the location of the insert and the measurement of the pre-crack curved front. Since all cracks exhibited a front that follows a circular shape. An arc was fitted to all the measured fronts, recording the diameter and the location of the center of the arc with respect to the side edge, and the top of the scanned volume.

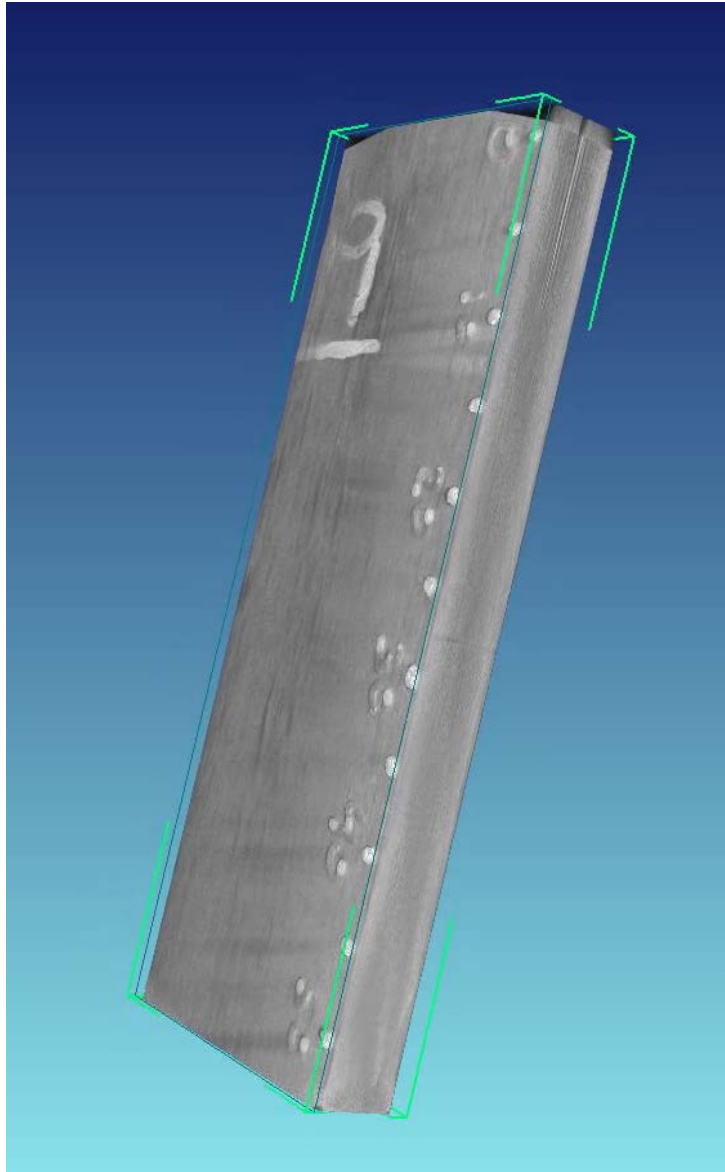


Figure 6-10 CT reconstructed volume

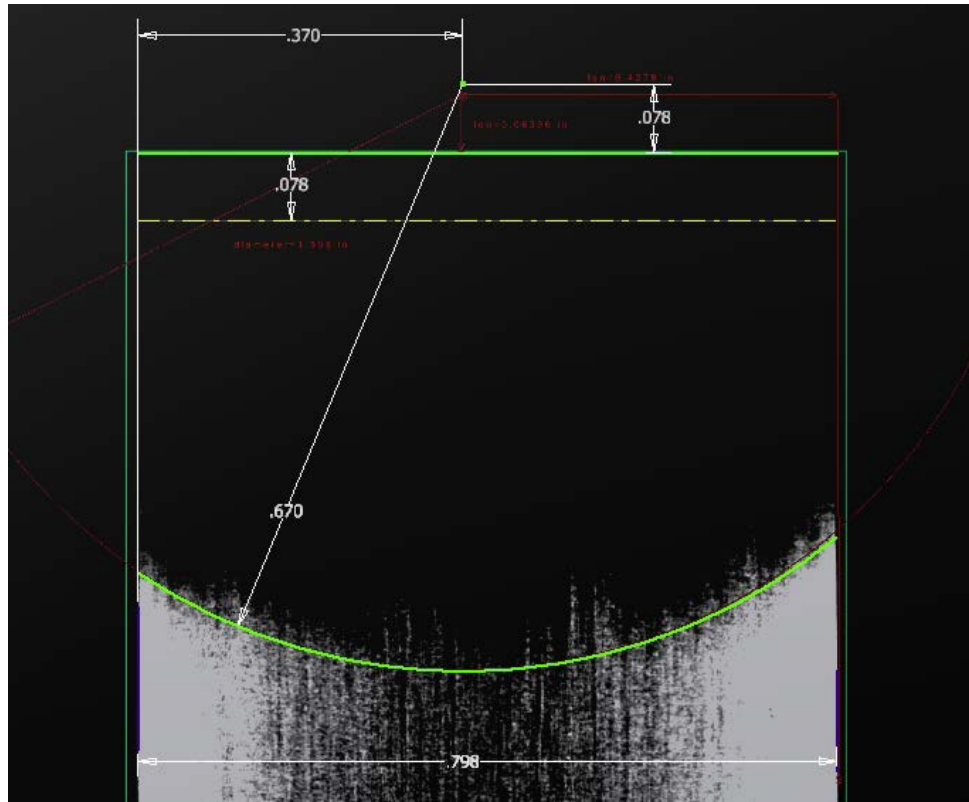


Figure 6-11 Crack front identification from CT reconstructed volume

Since the crack front identification and measurement process is subject to operator errors. A sensitivity study was conducted in order to evaluate the sensitivity of the calculated fracture toughness to certain changes and inconsistencies in the crack measurement process. All values identifying the curved crack front were varied within acceptable ranges, and the resulting fracture toughness was recorded. Then the percent change between the values of the first increment to that of the last increment were recorded. The study shows that the results are not very sensitive to measurements errors. For the X distance of the center of the arc from the top edge of the scan (length dimension), it was found that by varying the measurement by 0.01 inch, the calculated SERR changes by 0.43%. And by varying the same dimension by 0.1 inch, the output

changes by 2.6%. It is concluded that the calculated SERR is not very sensitive to errors in the length direction.

The measurement of the distance from the center of the arc to the side edge of the specimen (width direction) was then varied. It was found that for every 0.01 inch change in this dimension, the SERR changes by 0.67%. And for a total 0.06 inches, the resulting SERR changes by 3.7%. This also shows that the calculated SERR is also not very sensitive to errors in this measurement direction.

The radius of the arc was then varied to check its effect on the SERR. It was found that for each 0.01 inch change in the radius, the resulting SERR changes by 0.77%. And for a total of 0.08 inches change, the total error was 6.3%. This means that the resulting SERR is most sensitive to changes in the arc radius. However, the arc radius is the least prone measurement to error since it is easier to spot the trend of the crack line (radius), rather than its actual location (arc center X and Y).

To investigate the effect of a combination of measurement errors on the resulting SERR, the two cases, shown in Figure 6-12, were investigated and compared to each other. The output mode I SERR, through the middle 25% of the specimen, changed only by 7%. Even though this error is not significant enough to warrant the use of new testing devices or equipment, to assure accuracy, a procedure to evaluate the quality of the measurements was devised. For each measured crack front. The edge intersects are measured and compared with the visually measured crack progression for the same crack step. If at least one of the sides is not within 1% of the measured straight crack, the measurement is either discarded from the dataset, or retaken. Using this methodology, accuracy for all the measurements for the curved crack fronts is assured.

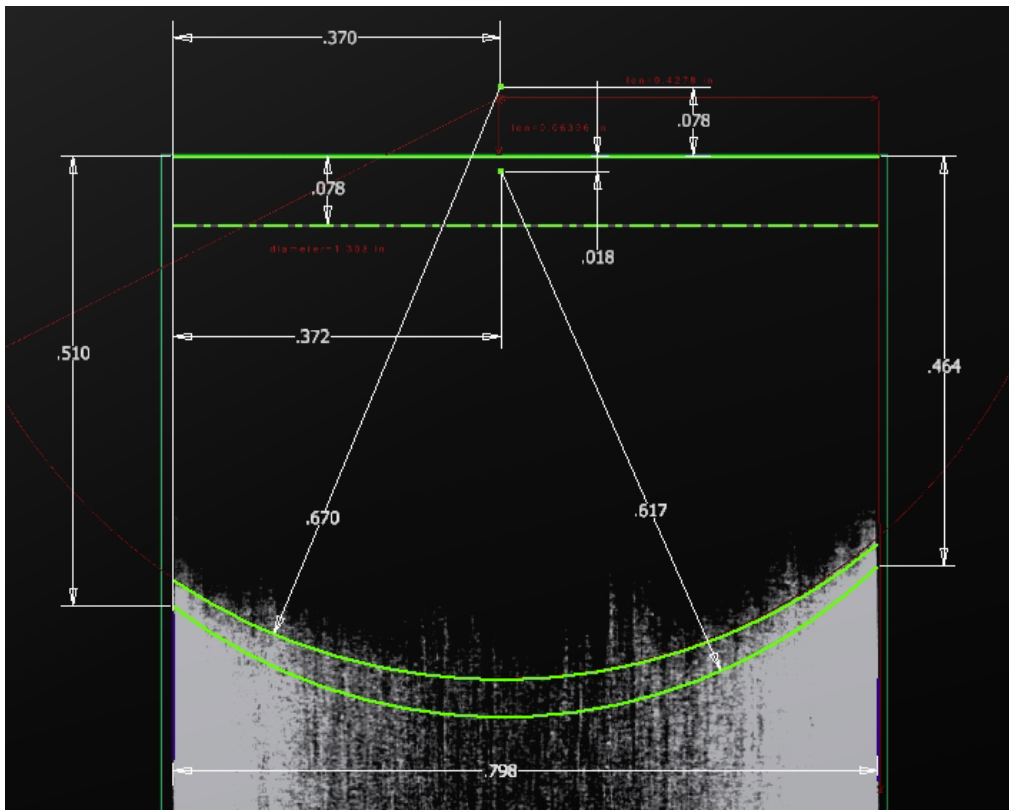


Figure 6-12 Crack front error sensitivity

To investigate the validity of the measurement method used earlier, The SERR across the specimen width was calculated using a different measurement technique and compared to the one obtained using the visual method. Instead of fitting a curve to a cross section of the specimen that is parallel to the crack plane. The depth of the crack front, measured from a cross section through the width (orthogonal to the crack front) was measured every 0.118 inches (3 mm) throughout the whole width of the specimen. To ensure measurement accuracy, the slicing plane yaw and pitch angles were adjusted so that the slicing plane is as orthogonal as possible to the width of the specimen. A

curve was fit to these data points resulting in the location and size of the curved crack front.

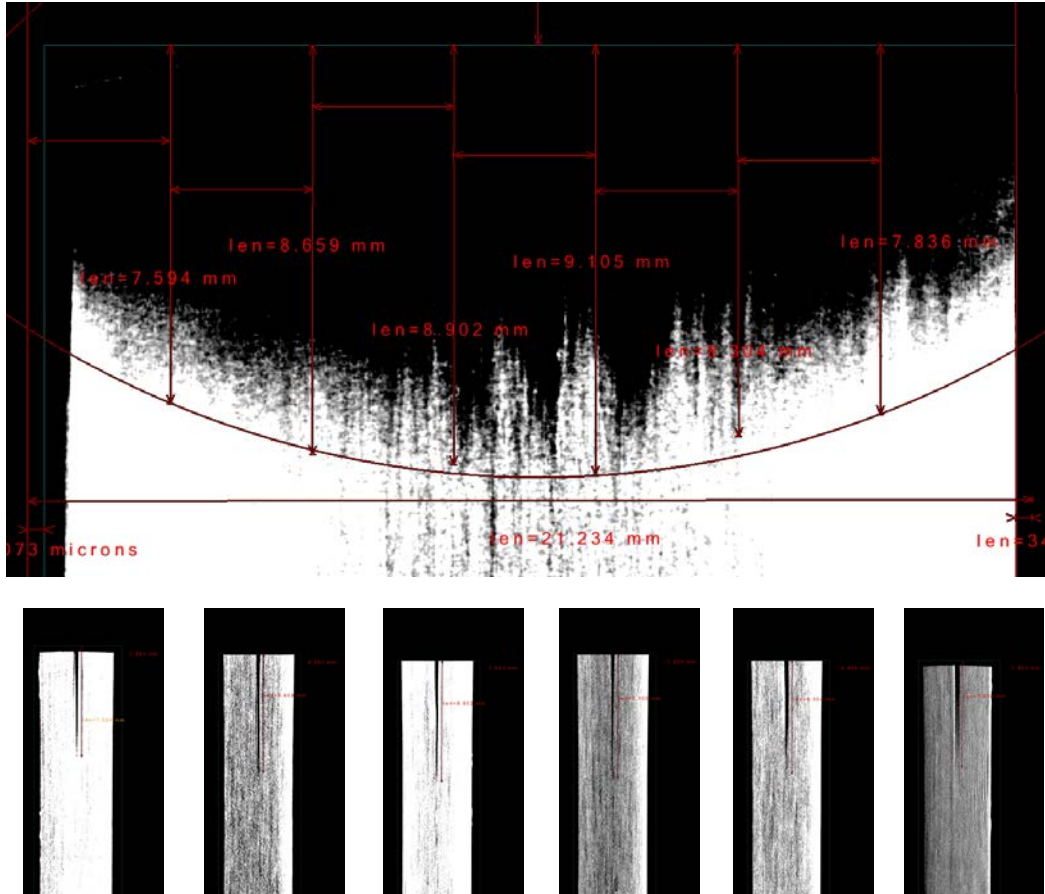


Figure 6-13 Different crack front measurement technique

For accuracy, a RANSAC algorithm with 0.01 fit tolerance, was used to fit the crack front to the data points. This ensures that a crack front that actually connects measured crack depths across the width of the specimen is identified. The algorithm was run a number of times equal to the factorial of the number of measurement points. The fit with the maximum number of point inliers, and minimum 'maximum error' was chosen.

This is shown in the figure below. As shown, the resulting SERR from this curved crack front resembled the ones obtained from visual fit of crack front as shown in Figure 7-34 and Table 7-6.

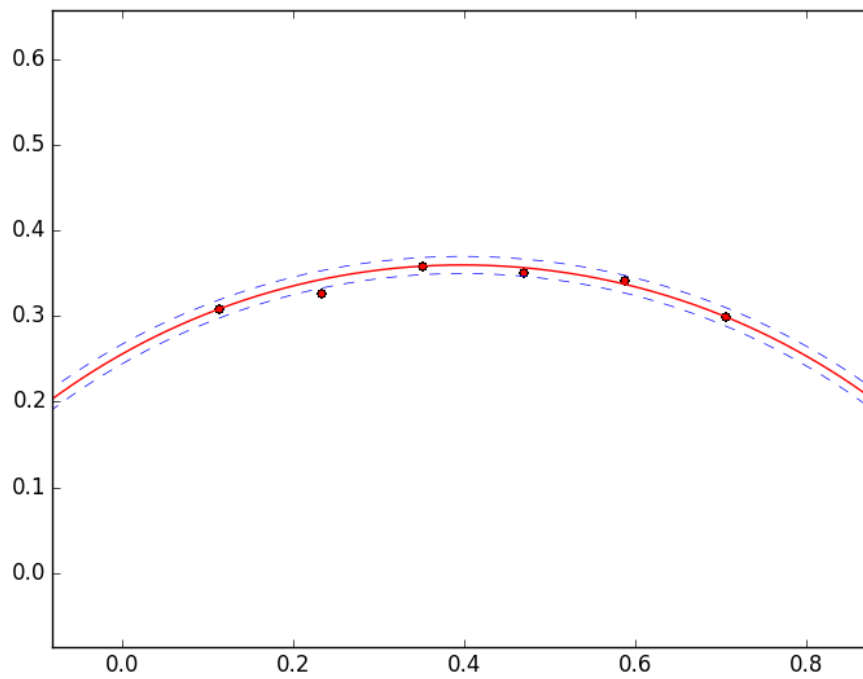


Figure 6-14 RANSAC curve fit

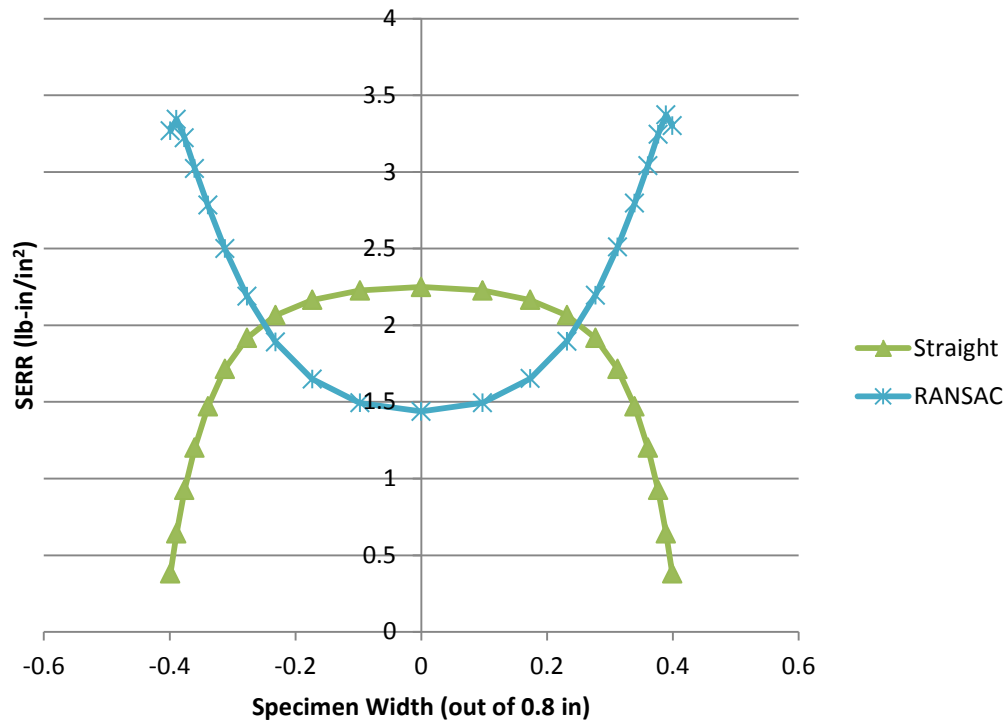


Figure 6-15 RANSAC curve fit for a 5mm crack length

Analytical Results

As mentioned earlier, due to the significant difference between the loading conditions of the current vertical test, and the loading condition assumptions used while devising any of the currently used DCB data reduction techniques, analytical data reduction for the vertical DCB test using the current techniques is not going to yield accurate results, however, it is calculated here for comparison and verification purposes only.

Figure 6-13 shows a comparison between the values of the strain energy release rates obtained using the compliance calibration technique for both the standard test, and the modified vertical test. The graph is plotted against the net growth in crack length. This

is because the vertical DCB specimen loading blocks are larger than the hinges used for the horizontal DCB. As seen, there is a visible difference between both methods. This is the result of the combined loading conditions in the vertical test, unlike those in the horizontal, standard one.

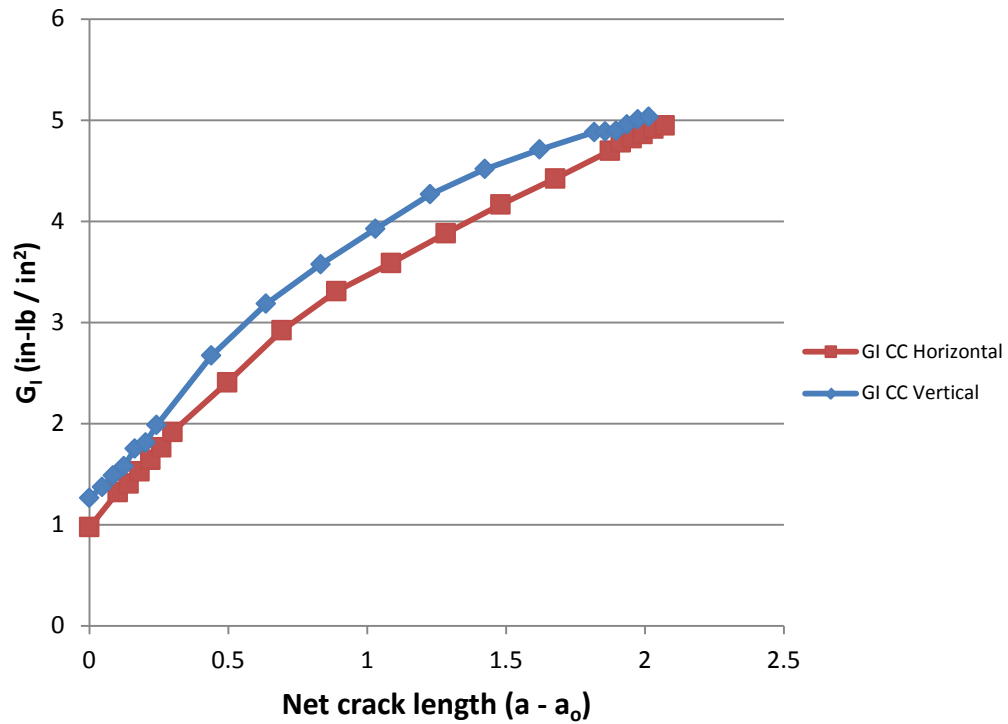


Figure 6-16 Comparison between horizontal DCB and Vertical DCB

Chapter 7

DCB : Part II FEM Modeling

Horizontal DCB

A finite element model was developed to calculate the strain energy release rates for the tested specimens. The FEM specimen dimensions are the same as the ones tested earlier and the material properties are listed in Table 7-1. The FEM model is also shown in Figure 7-1. The hinge supports were modeled using reference points and coupling constraints, tied to the area of the specimen that is glued to the hinge. The reference point is located at the mid-point of the hinge pin axis. Displacement boundary conditions were applied at the top reference point to simulate the test machine cross-head movement using the load measured from the experiments. While the bottom hinge reference point was fixed in all translations and rotations except for rotation around the Y-axis, just like the test setup.

Table 7-1 S2-E773 Material Properties [85]

Property	Value
E_{11} (msi)	6.82
E_{22} (msi)	1.82
E_{33} (msi)	1.82
G_{12} (msi)	0.617
G_{13} (msi)	0.604
G_{23} (msi)	0.649
ν_{12}	0.29
ν_{13}	0.27
ν_{23}	0.41

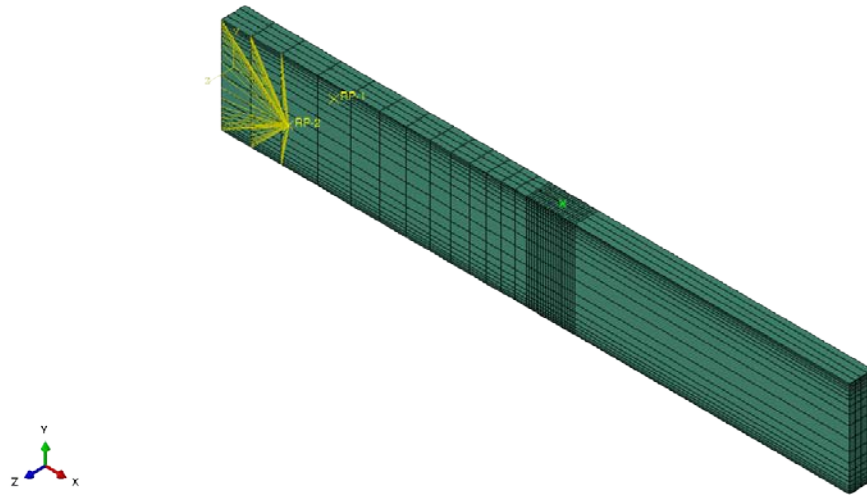


Figure 7-1 FEM DCB model

Several modeling and meshing techniques were experimented with, to gauge their effect on the resulting SERR. To model the crack opening, two techniques were experimented with, a model with Tie constraints constraining the nodes that are not cracked, and another by merging the same nodes. Both methods resulted in the same SERR values. Also, two different meshing techniques were used to mesh the region around the crack front. One with collapsed elements around the crack front as shown in Figure 7-2, and another with fiber-oriented mesh. They both resulted in the same values, and the oriented mesh was chosen for its simplicity.

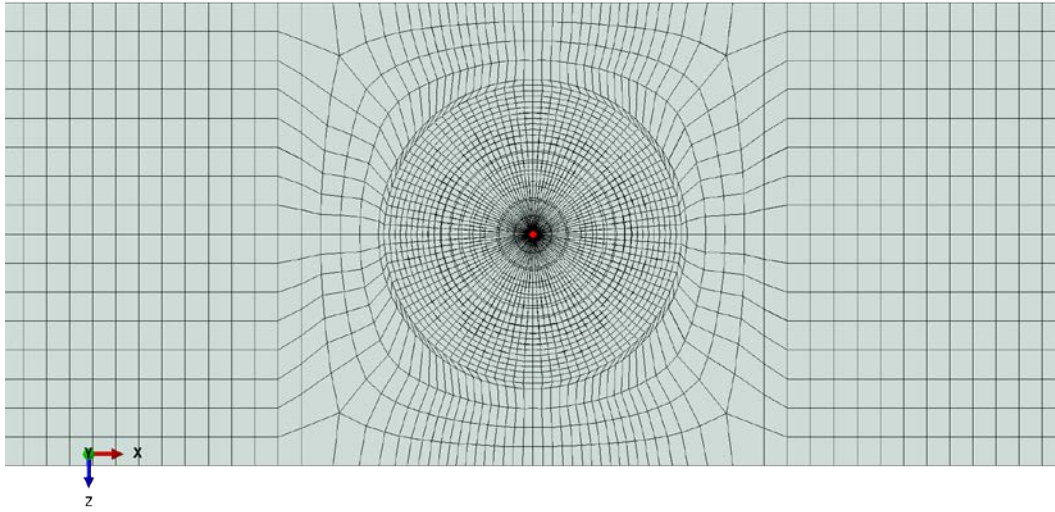


Figure 7-2 Collapsed mesh

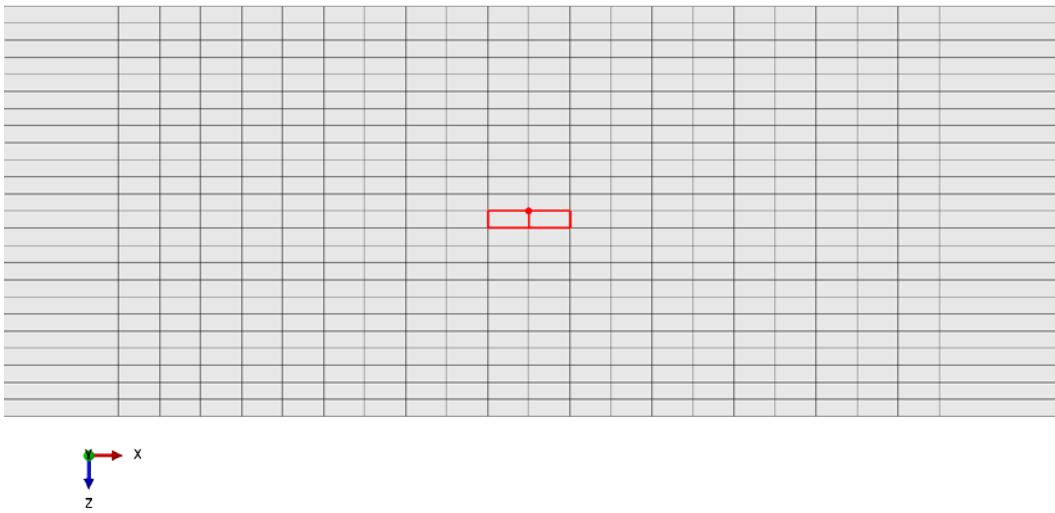


Figure 7-3 Top view of elements below crack front and crack front nodes

The DCB experiment is modeled using python programming language and the python scripting utility in the commercial finite element modeling software Abaqus. The modeling process is as follows (See appendix A for the model creation script). A

rectangular part having the specimen dimensions and extruded to half the specimen thickness is created. The part is then partitioned into four sections. The hinge supports, before-crack section, crack region, and after crack region. The crack region is a fine mesh region that allows for capturing any non-linear effect or behavior around the crack front. It is 0.4 inches in length with the crack front in the middle. Each section is seeded using the appropriate size or ratio as explained further in the following mesh convergence study. The part is then meshed. This mesh is orphaned and then mirrored. The full DCB model is created by merging both mirrored parts. The nodes identified as the crack face nodes are temporarily dislocated away from the mid-plane of the specimen during the merge process; they are then relocated back to their original position after merging. This resulted in double nodes throughout the crack surface, allowing for the split behavior of the DCB specimen.

Node sets and element sets are created for the crack front and the elements surrounding it in pre-processing. This is to allow for the calculation of the SERR in post processing using nodal displacements and nodal forces from element contribution as explained earlier in the background section regarding the calculation of SERR using the VCCT method. Constraints, boundary conditions and loading forces are prescribed as discussed earlier. Nodal forces and displacements are requested as simulation outputs. Also, the contour Integral J-Integral is requested as a history output for 7 different contours for all the nodes defining the crack front. This is to compare and validate the SERR values that are calculated via the VCCT method.

After the simulation is completed, the output database is post processed using python scripts to calculate the SERR at each of the crack front nodes using the VCCT method by means of the nodal forces calculated from element contribution and the corresponding nodal displacements for fracture modes I, II and III. Also, the values for the

J-contour integral for the seven different contours for each of the crack front nodes is extracted and compared to these calculated using the VCCT method earlier.

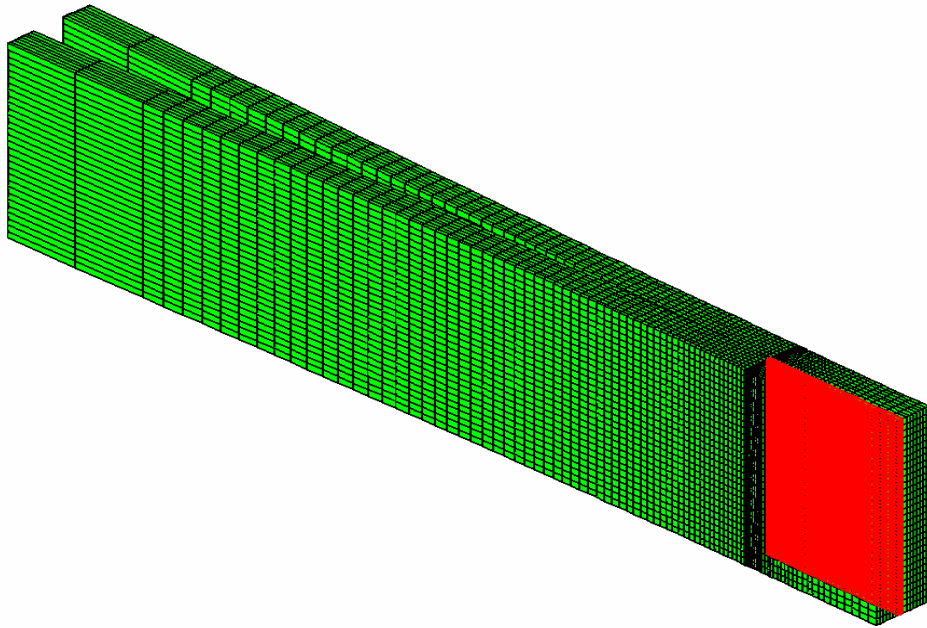


Figure 7-4 Model showing merged nodes

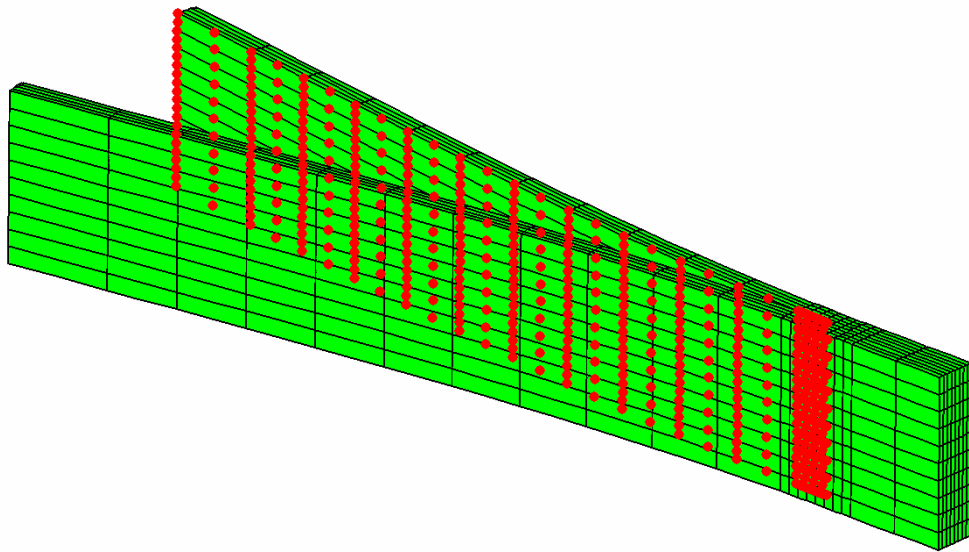


Figure 7-5 Nodes not merged

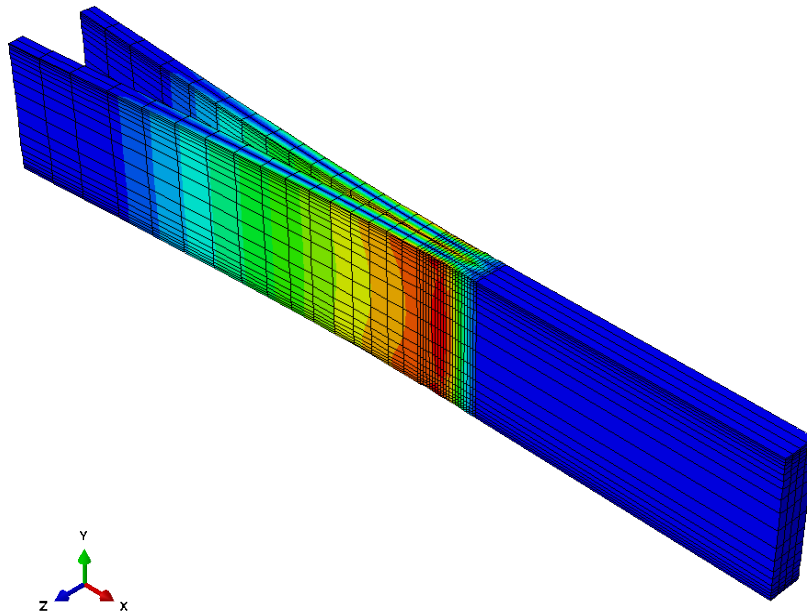


Figure 7-6 Sample output for orphan mesh, merged model.

Model Mesh

Several mesh distributions and sizes were experimented with in order to find a configuration that yields converged results, while taking a reasonably small amount of time to process. First the convergence criterion was to be determined. For that, several, fine mesh models were created and processed in order to determine which SERR calculation method should be used (VCCT vs J-Integral). It was found that for finer meshes, the values acquired using the J-Integral matched very well those calculated using the VCCT method. However, as the mesh was made coarser, the calculated SERR values calculated using the J-integral method started deviating from the converged value, while the values obtained using VCCT remained the same. This shows that the SERR calculated using the J-Integral is more sensitive to mesh size than that calculated using the VCCT method. For this reason, the SERR calculated by means of the VCCT method is used as a convergence criterion.

Mesh Convergence

The convergence process is as follows; the model is generated and processed for a specified specimen dimensions and forces. All mesh sizes and ratios are held constant except for the one being studied. The mesh size of the region being studied is varied within a set of values and the simulation is processed each time. The VCCT SERR values for each of these mesh size iterations are then calculated after the simulation is processed, and stored in a table. This process is repeated for all mesh regions. After all the simulations are conducted, the calculated values are post processed using spreadsheet computer software, and the percent difference in SERR value between each iteration and that of the finest mesh for this one mesh region is calculated and recorded. These values are then plotted against the mesh size / number and the coarse mesh

value where the plot is within 1% of the finest mesh value is selected as the converged value.

As shown below, the model is divided into four meshing regions in the length, the hinge supports (region I), before crack region (region II), crack-front region (region III), and after crack region (region IIII). There is only one width region, and one height region. In total, there are 6 different meshing regions. The specimen dimensions and boundary conditions of the maximum crack length for one of the tested specimens were used for the study. Both region II and the specimen width have a linearly variable (biased) mesh arrangement. Region II has the minimum and maximum element sizes specified with the maximum size fixed at 0.3 inches and the minimum size being part of the convergence study. The specimen width has the number of elements and element size ratio (maximum element size to minimum element size) prescribed instead. The width mesh ratio is studied and a ratio of 10 was found to be adequate. The details of this study are discussed after this section.

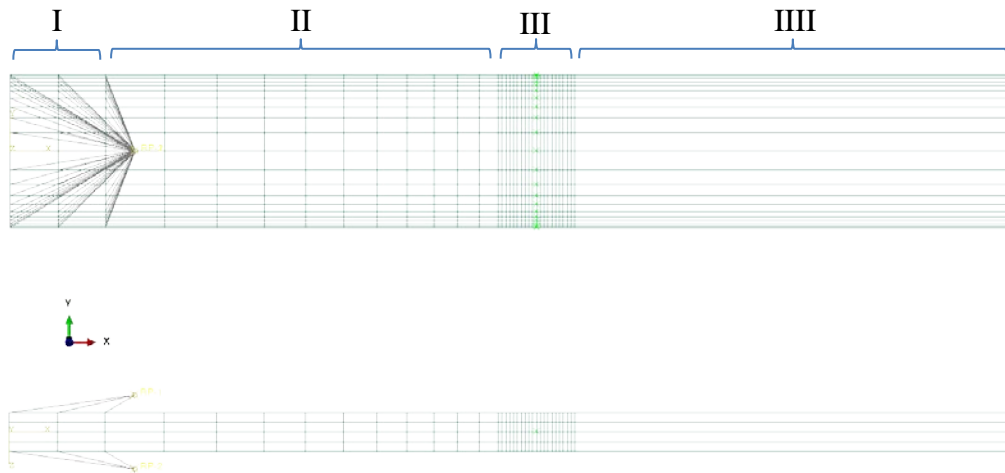


Figure 7-7 FEM DCB model

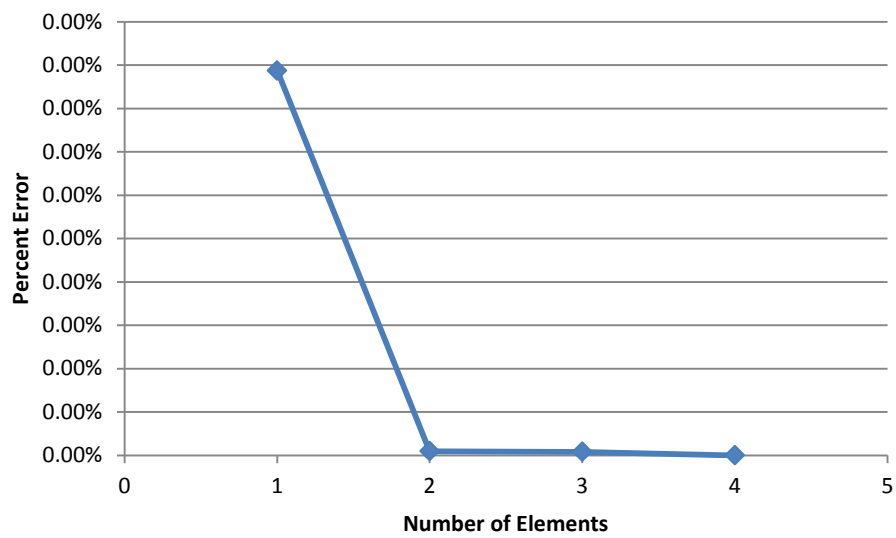


Figure 7-8 Mesh convergence for region I

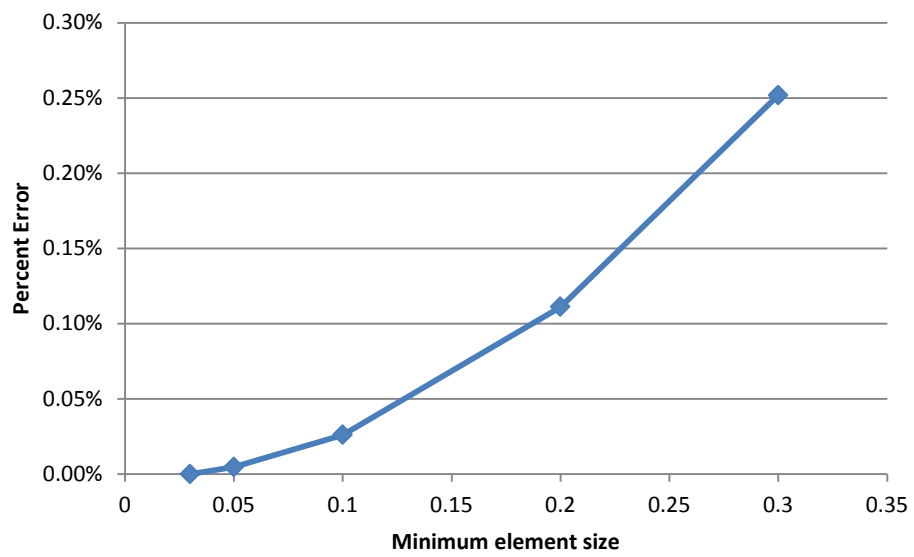


Figure 7-9 Mesh convergence for region II

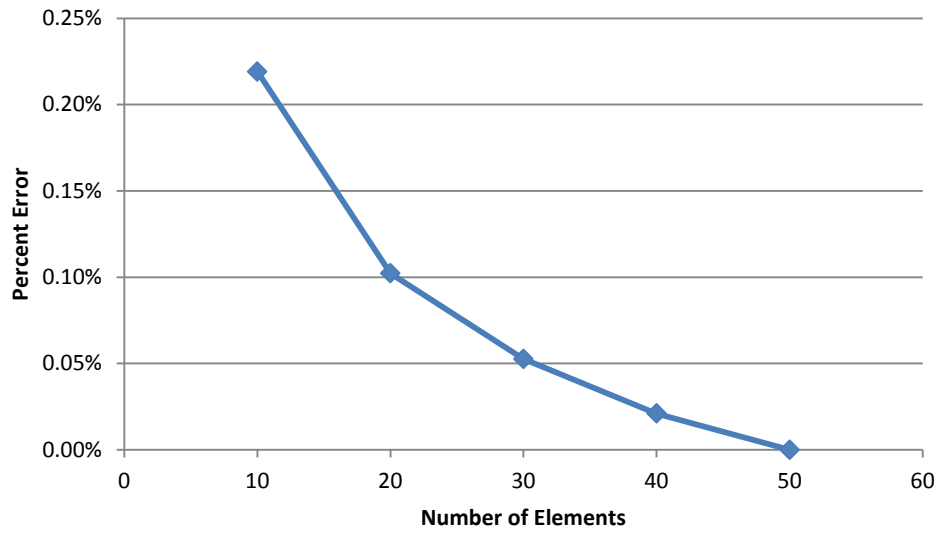


Figure 7-10 Mesh convergence for region III

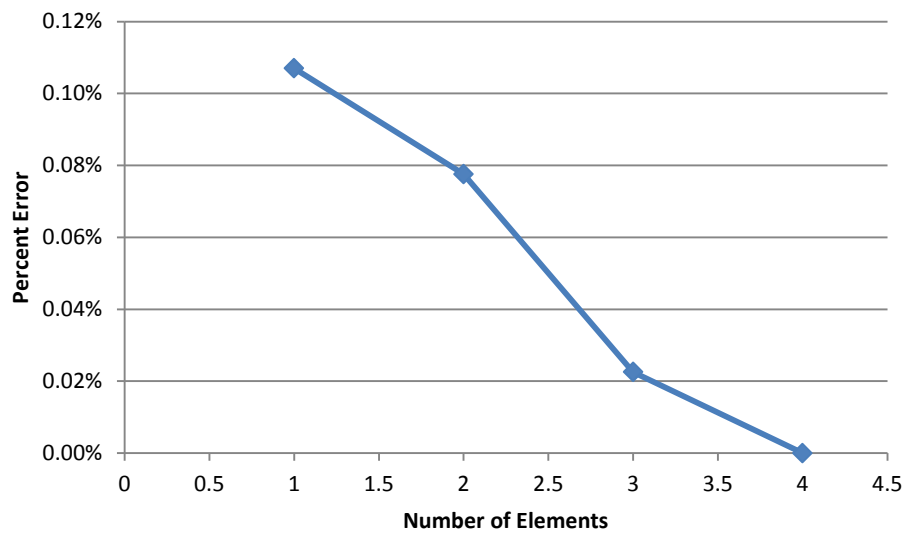


Figure 7-11 Mesh convergence for region IIII

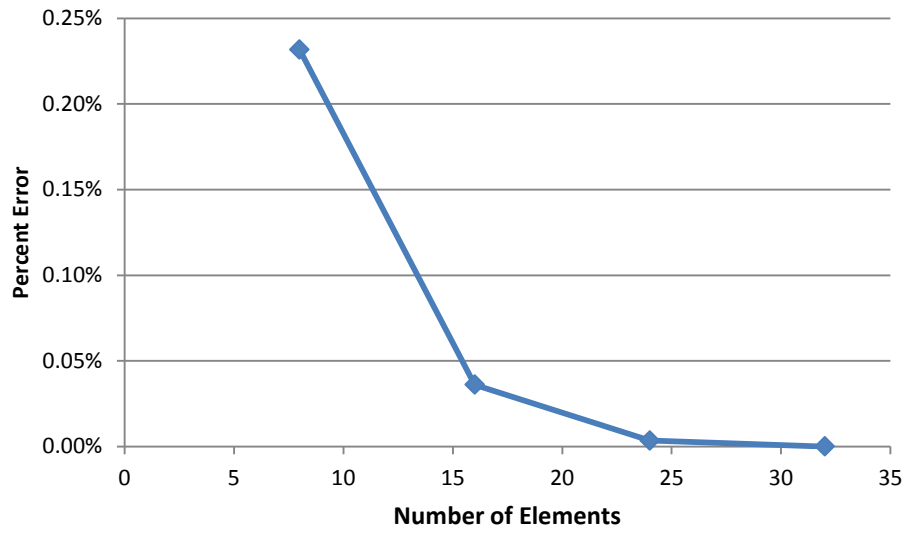


Figure 7-12 Mesh convergence for Specimen Thickness

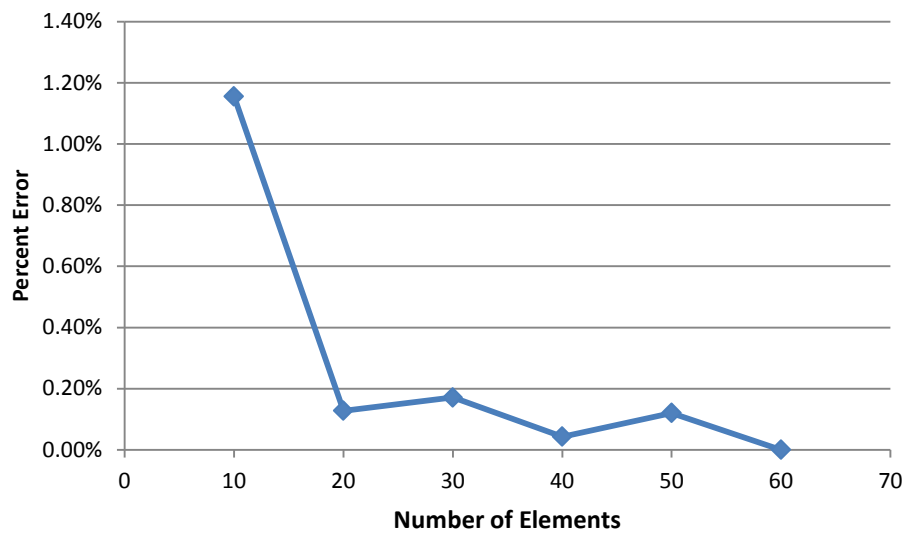


Figure 7-13 Mesh convergence for Specimen width

Table 7-2 Mesh Convergence Results

Region	Parameter
Hinge (Region I : number of elements)	2
Before crack (Region II: minimum element size)	0.1
Crack Front (Region III: number of elements)	20
After Crack (Region IIII: number of elements)	1
Specimen Thickness (number of elements)	8
Specimen width (number of elements)	20

Mesh across specimen width

The width of the specimen was meshed using three different methods. The first method used was uniform mesh size through specimen width. This did not properly capture the nonlinear SERR distribution around the specimen edges as shown in Figure 7-14. To alleviate that, a mesh similar to the one used by R. Krueger et al [67] was then used. Two fine mesh regions were added to the length-wise sides of the specimen as shown in Figure 7-15. This depicted the nonlinear SERR distribution close to the specimen edges much better than the previous method. However there was no even distribution of data points along the specimen width, also a large number of elements had to be used in order to capture the nonlinear behavior around the specimen edges in detail. This prompted the use of a different meshing method across the specimen width. A linearly variable, double bias mesh, that is coarse in the middle of the specimen, and gets finer as we approach the width edges was used. To achieve this effect, the element size was made dependent on the element location relative to the specimen width.

For that new mesh, it was found that a ratio of the size of the largest element to that of the smallest element of 10 produced evenly distributed data points across the width. To determine this ratio, the number of elements across the specimen width was kept constant, and the ratio of the size of the largest element to the smallest one was

varied until a uniform SERR distribution across the specimen width was achieved. A value of 10 for the bias ratio means that the largest element size is 10 times the size of the smallest one. This distribution is shown in Figure 7-16.

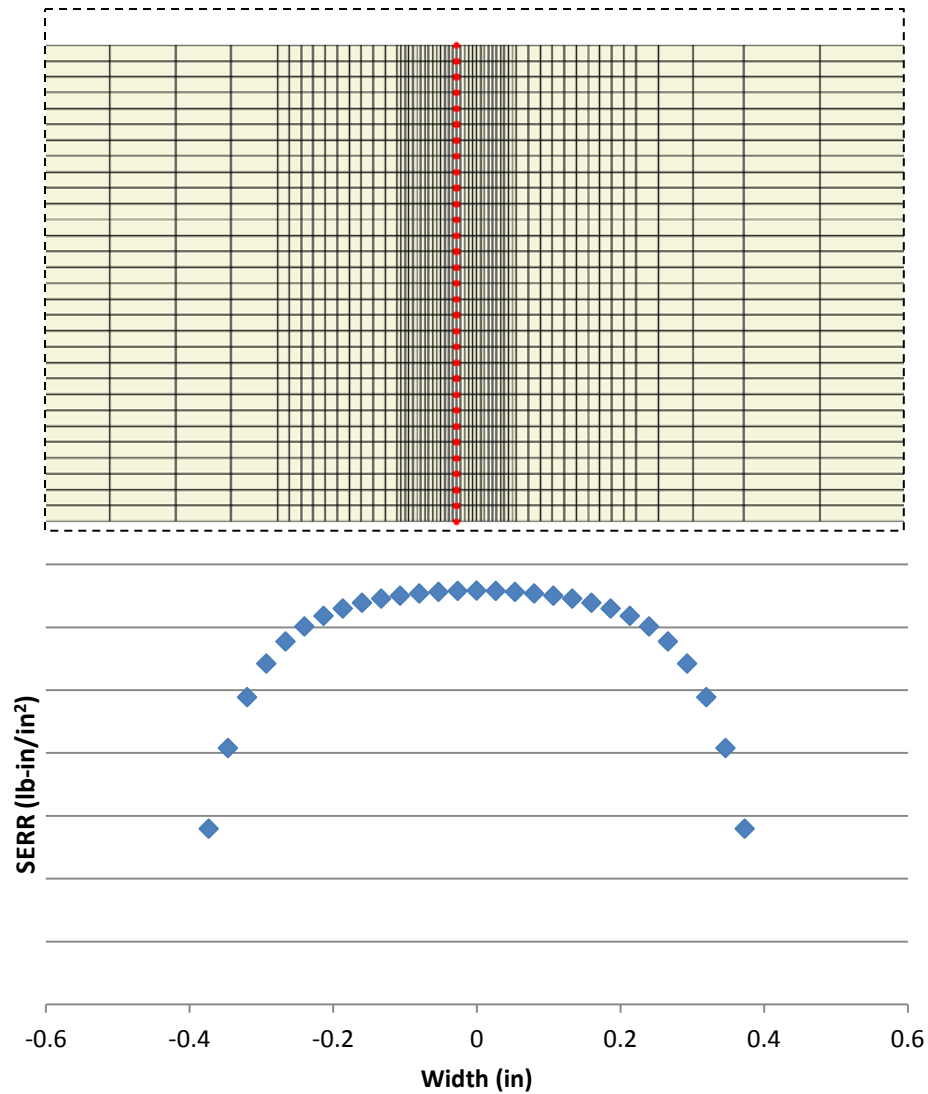


Figure 7-14 Uniform mesh size across the specimen width

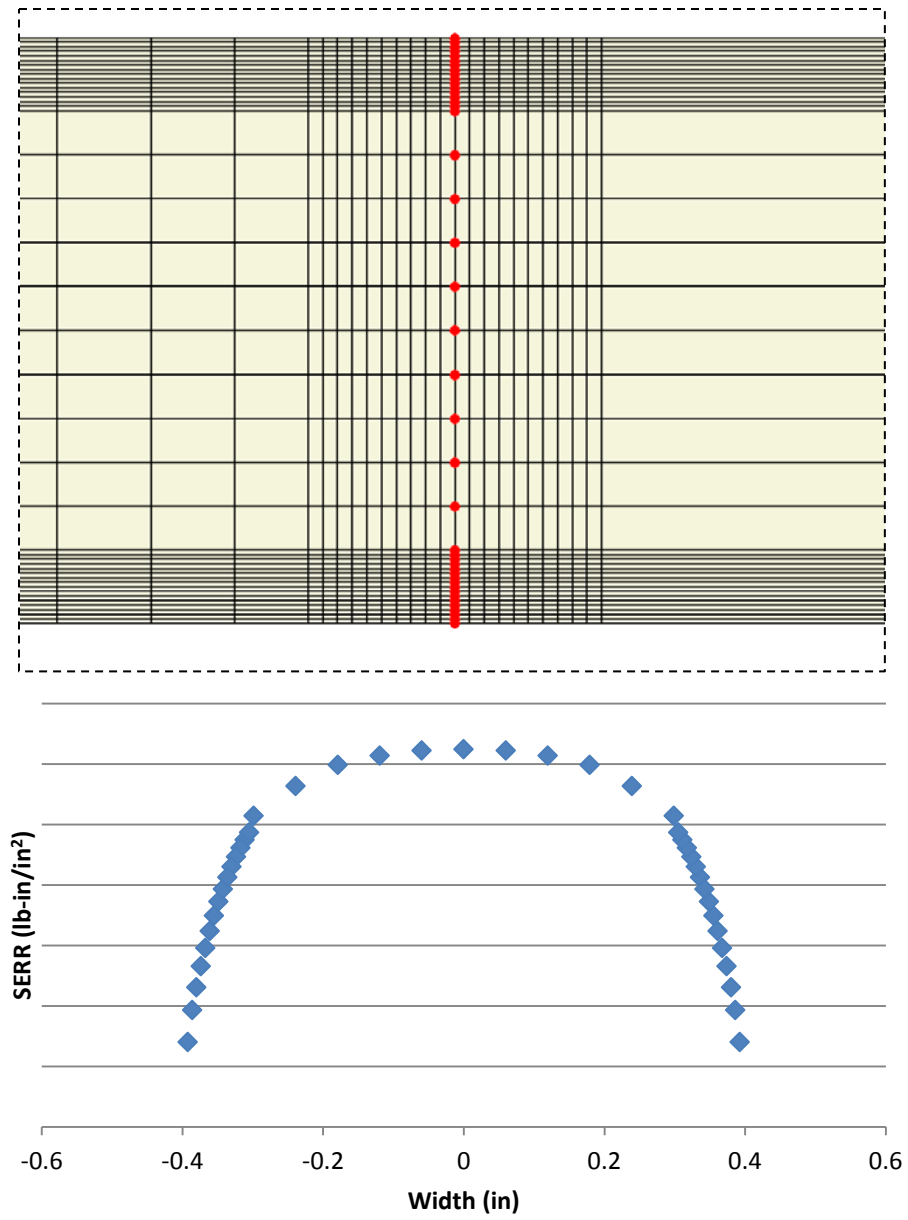


Figure 7-15 Mesh with refined bands at the edges

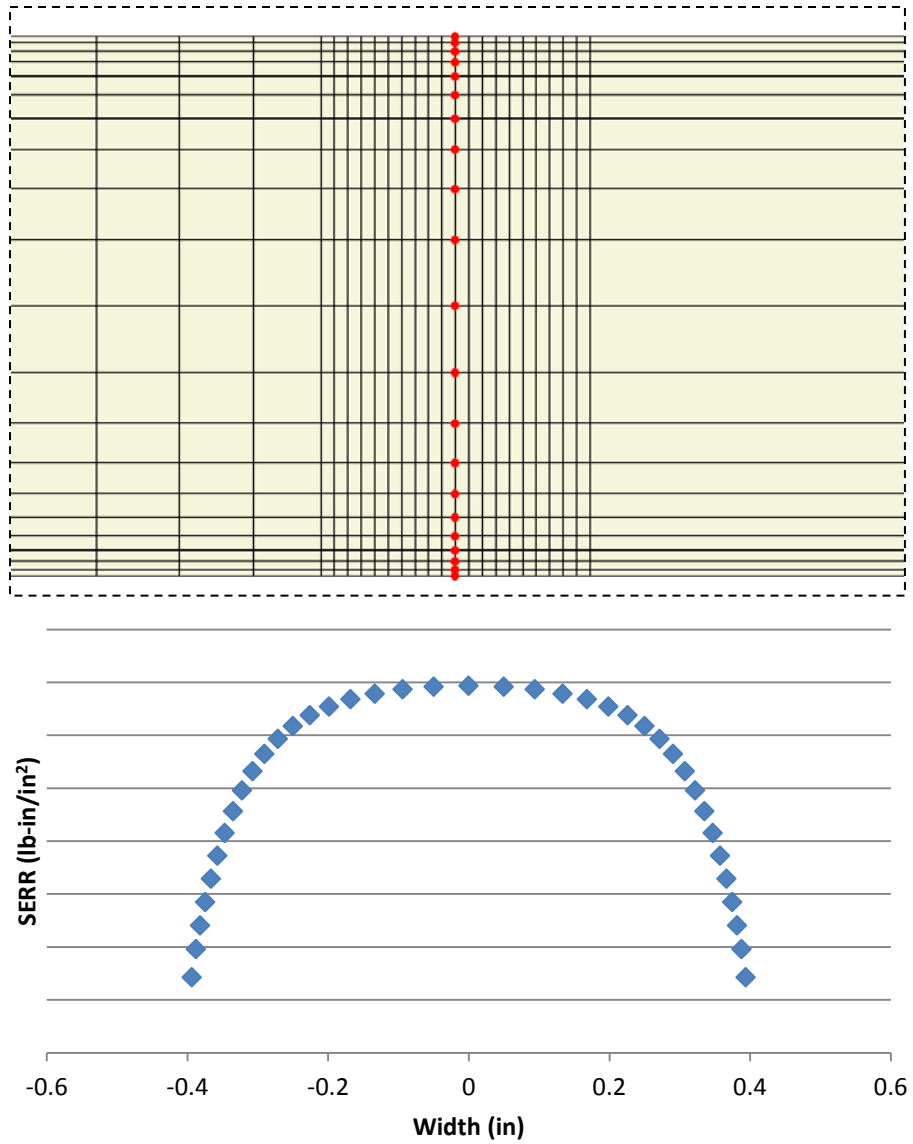


Figure 7-16 Mesh with linearly variable mesh size across the width

Verification

In order to validate the model, it was used to predict the crack opening displacement for an isotropic double cantilever beam with material properties shown in table 4 and Parameters shown in Table 5. The results from the simulations were then

compared to the deflection calculated using Euler Bernoulli beam theory (equation 8.1). Four element types were used, a 1st order 8-noded reduced integration brick element (C3D8R), an 8-noded element with incompatible modes to improve response under bending loads (C3D8I), a 2nd order 20-noded reduced integration brick element (C2D20R), and a 2nd order 20 node brick element (C3D20).

Table 7-3 Isotropic Material Properties

Property	Value
E (msi)	6.82
v	0.29

Table 7-4 Verification Model Parameters

Verification Model Parameters	
Length (in)	3
Width (in)	0.8
Height (in)	0.2
Tip Load (lb)	2

$$\delta = \frac{pl^3}{3EI} \quad (8.1)$$

Using the above equation and for the given beam dimensions, the beam deflection using Euler-Bernoulli beam theory is found to be equal to 0.079 inches. The percent difference between the FEM results for each of the selected element types and that of beam theory are shown in Table 7-4. From the results, it is clear that the 20-noded elements, as well as the 8-noded element with compatible modes all produce acceptable results that are within reasonable limits from the deflection computed using beam theory. The 8-noded element with incompatible modes produced the least error of all. This

validates the use of this element type for this model. This conclusion is the same as what Kreuger concluded in [24], [86], [87].

Table 7-5 FEM Element Selection

Element Type	δ FEM	% Error
8-noded reduced integration brick elements (C3D8R)	0.1088	37.4 %
8-noded incompatible modes elements (C3D8I)	0.0821	3.7 %
20-noded full integration brick elements (C3D20)	0.0824	4.0 %
20-noded reduced integration brick elements (C3D20R)	0.0825	4.1 %

It was also noticed that the element type affected the convergence of the SERR calculated using the J-integral method over 6 contours. The largest scatter was that for the 8-noded reduced integration elements with 0.9% difference between the maximum and minimum values. The 8-noded element with incompatible modes had a difference of 0.3% while both 20-noded elements had a difference less than 0.1%. Also the mean of the values obtained from the 8-noded reduced integration elements was significantly higher than that of any of the other element types used as shown in Figure 7-17.

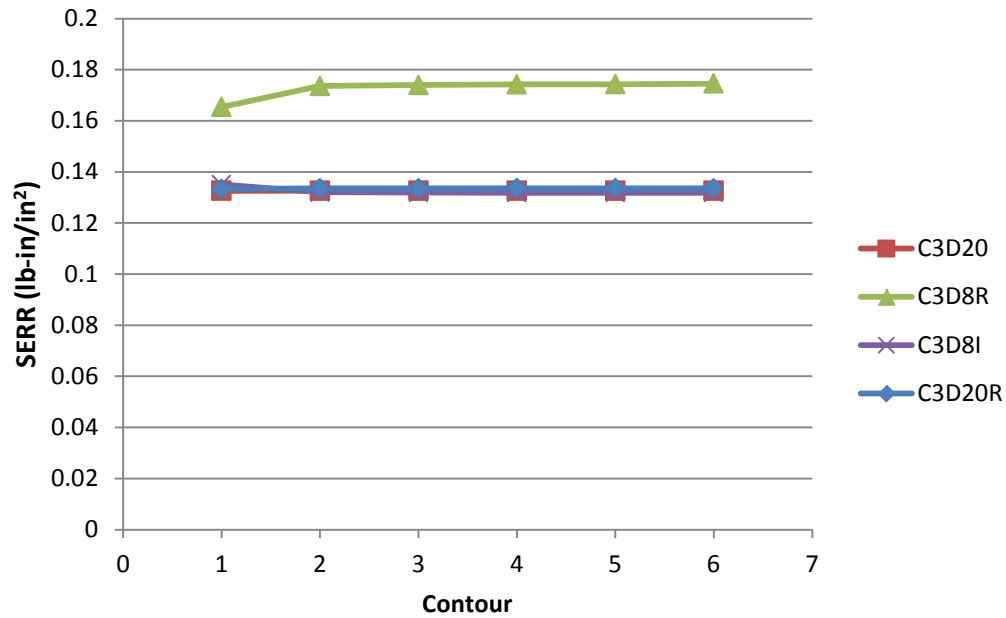


Figure 7-17 Comparison between J-contour values for the different element types.

Effect of accounting for material non-linear Behavior

The effect of accounting for material non-linear behavior was studied using two different mesh sizes and two material models. The meshes were a fine one and a coarse one. And the two material models were one using 9 elastic constants to model the behavior of the composite, and another using 15 material constants and accounting for material non-linear behavior by using a user material model UMAT utilizing the Ramberg-Osgood equations for shear deformation behavior. The displacements reported by both models had almost identical results. The energy release rates calculated using the VCCT method using both material models also had a negligible difference of 0.001%. However, the model utilizing the non-linear user material showed large scatter (lack of

convergence) of the values of the SERR between the different J-integral contours. It also overestimated the value of SERR for higher order elements and finer meshes.

It is worth noting that the J-integral contours in this study are calculated just for the verification of the values of SERR that are calculated using the VCCT method. This is because a finer mesh is required in order to obtain good convergence for the values of the contour integrals. On the contrary, the VCCT method is found to be much less sensitive to mesh size. For this reason, the J-integral value and the VCCT values were compared for few cases to assure accuracy and validate the VCCT SERR values. But for the remainder of the study, mesh that only converges for the SERR calculated using the VCCT method is used.

The contour integral capability in the commercial Finite Element package Abaqus was used to output the j-integral values over seven contours around the crack tip as a history output. Figure 7-19 shows the plot of the Strain Energy Release Rate calculated using the VCCT method across the width of a specimen compared to those of the 7 contours of the j-integral. They show good agreement, with a maximum difference of 0.6%.

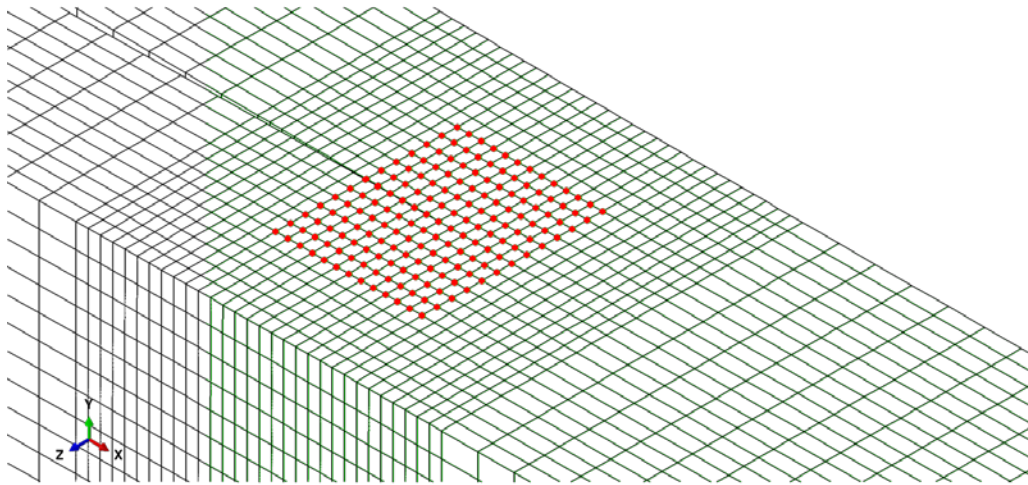


Figure 7-18 Close-up showing Node Set for Contour #7 in red

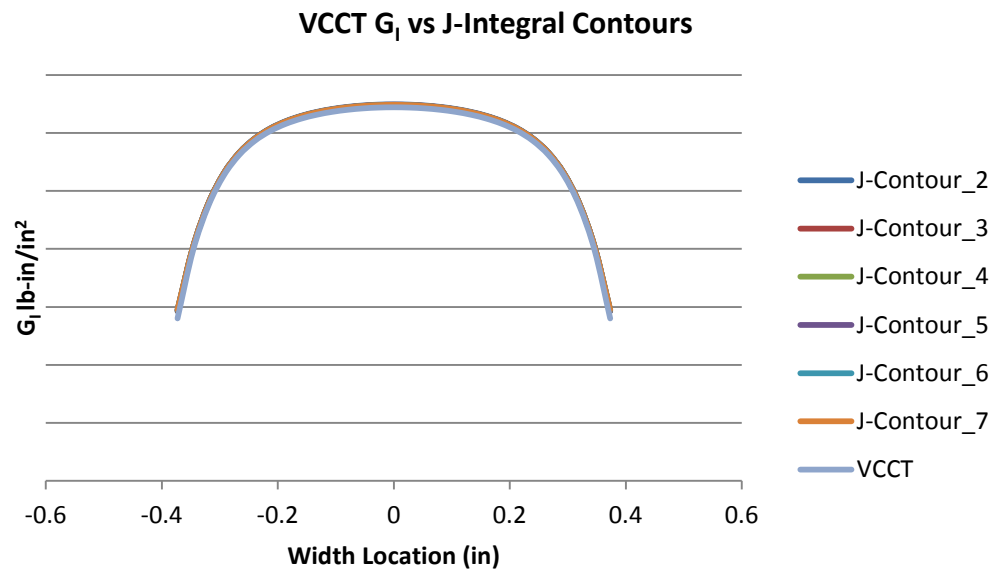


Figure 7-19 VCCT vs J-integral Contours

FEM Data Reduction

The data acquired from the FEM model was the SERR for the nodes along the crack front, the resultant is a curve that has much smaller SERR values close to the specimen edges and higher values towards the middle of the specimen. This is due to 3D effects like anticlastic bending and free edge effects as discussed earlier. Figure 7-20 shows a comparison between the normalized FEA SERR across the width of the specimen, and that calculated using the Compliance Calibration method.

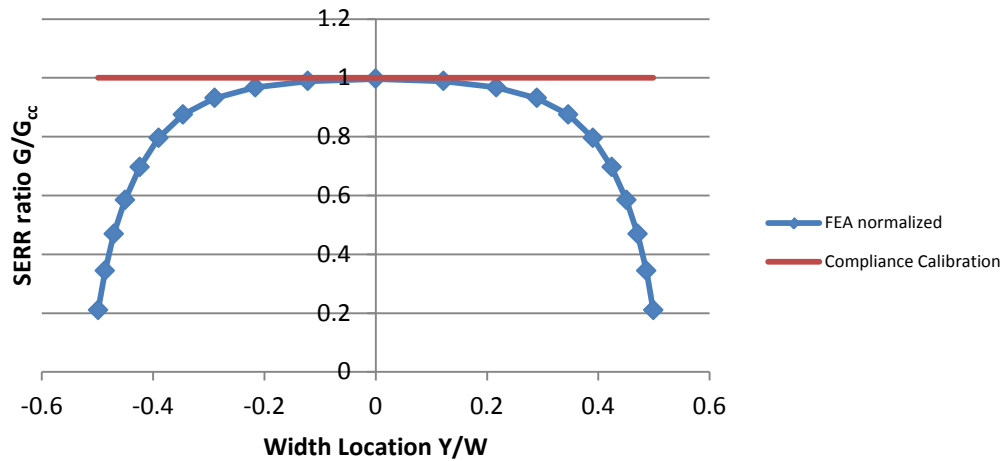


Figure 7-20 SERR across specimen width

From the above figure, it is clear that the FEA SERR across the specimen width approaches the experimental value calculated using the compliance calibration method, in the middle of the specimen, it then decays as it approaches the specimen edges. Raju et al [88] attributed this to boundary-layer effects for isotropic materials. Also Chan discussed the boundary layer sizes and stresses, and their effects on the overall performance of composite laminates [15]. This prompted the examination of the effect of specimen aspect ratio (width to thickness) on the SERR distribution across the specimen width. In the study, several finite element models were created while varying the

specimen width and keeping all other dimensions the same. The SERR normalized with respect to the midpoint (maximum) SERR value was used in order to only observe the effect of the width on the SERR distribution and not the effect of width on the total energy release rate for the specimen.

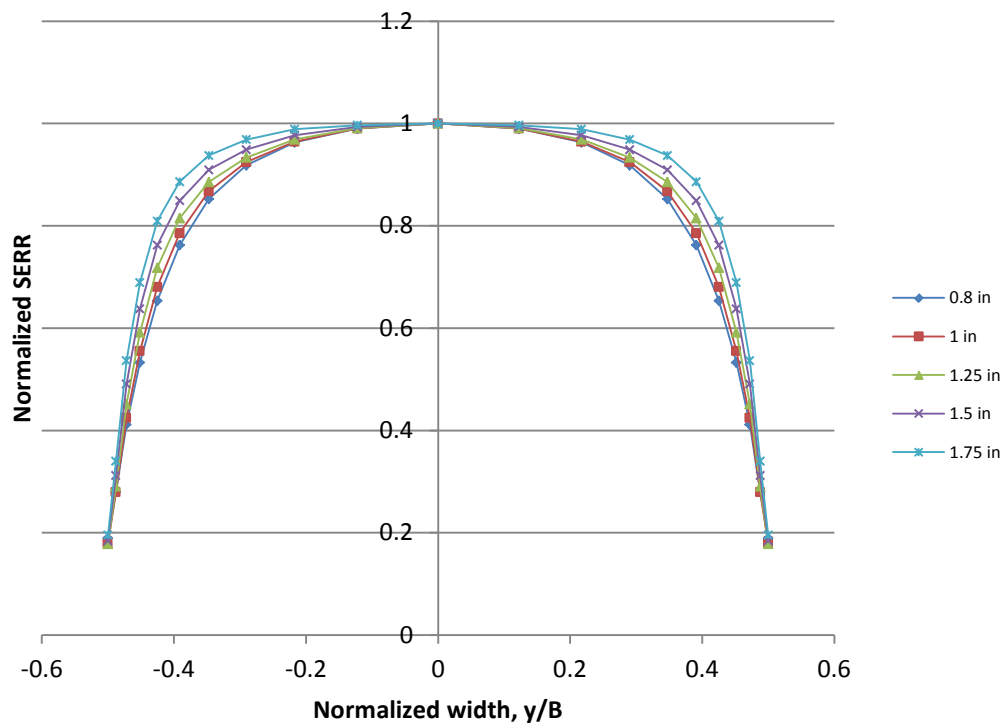


Figure 7-21 Normalized SERR vs Normalized width for different specimen widths

From the above figure, it is evident that the SERR distribution does change with the change in aspect ratio. The SERR tends to 'flatten' more towards the middle, as the specimen width is increased. This, as discussed earlier, is due to the different D_c factor for each of the different aspect ratios studied. The S2/E773 Glass-epoxy composite used here, has much higher D_c value than other composites. The table below shows D_c

calculated for different materials. The higher the value of D_c , the shorter the region with uniform SERR values across the specimen width will be.

Table 7-6 D_c factor values for different materials

Material	D_c ($\times 10^{-3}$)
IM7-8552	9
T300-976	7
AS4-3502	7
S2/E773	22
Isotropic	90

As shown in Table 7-6, the specimens tested (S2/E773) have higher D_c than other composite materials of the same layup and dimensions. And because the SERR in the middle section the specimen width is the closest to the experimentally calculated value using the compliance Calibration Method, and due to the need for a holistic method to calculate the SERR that would be applicable later while investigating curved crack fronts as well. A method that is not affected by the parasitic SERR decay close to the specimen edges, yet holistic enough to be applicable to both the straight and the curved crack fronts observed from CT scans had to be devised.

After careful observation of Figure 7-20 and Figure 7-21, for the 0.8 inch wide specimens that are used in this study, the average of the data points of the middle 0.2 inch (5 mm) of the specimen (middle 25%) would yield reasonable SERR measurement. This was chosen because larger values would start to capture the parasitic, non-linear behavior close to the specimen edges. And smaller values would result in the calculation being very sensitive to the location of the center of the curved crack with respect to the

specimen center. This chosen value resulted in an average difference of 0.9% between the SERR calculated from FEA models and that calculated using the compliance calibration method for the pre-crack increment of the standard DCB tests.

Horizontal FEM Model Results

Each of the specific specimen geometries and boundary conditions was used as an input for the finite element model and the average of the middle 0.2 inches was taken as the SERR for that crack opening increment. This process was repeated for each crack progress increment generating an R-curve for each tested specimen. The average of the results for all the specimens for each crack opening length is taken and is used to plot the average R-curve for all the specimens. The average had a standard deviation and a covariance of 0.14. This is compared to the results obtained from the FEA models as shown below.

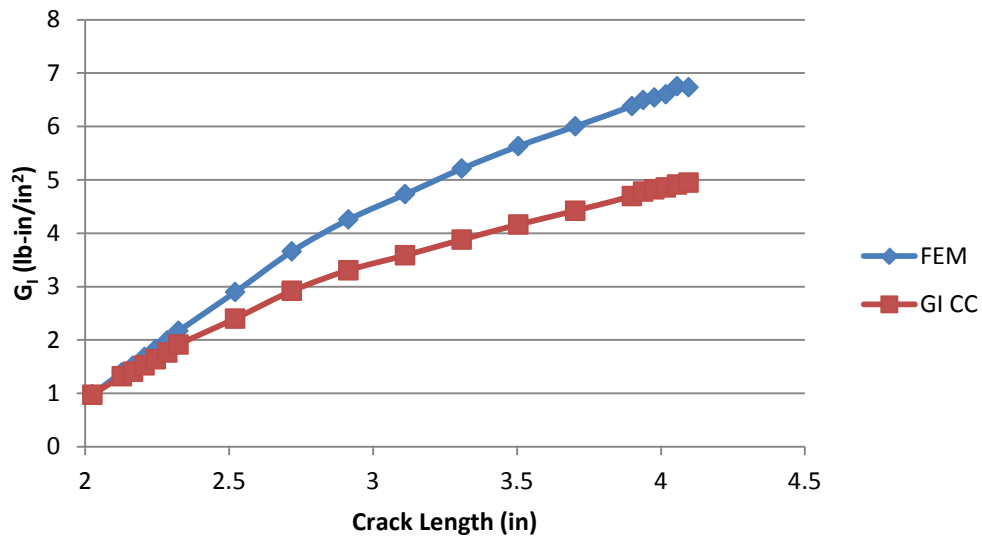


Figure 7-22 Comparison between FEM and Experimental results

As shown, the Fem results did yield highly correlated values to those obtained experimentally. Having only 0.9 % difference for the critical value compared to the values obtained using Compliance Calibration. As shown, for smaller crack lengths, the FEM model and the Experimental values have very good correlation. The difference gets larger as the crack length increases. This is mainly because of the fiber bridging phenomenon as mentioned in [22]. This can be explained as follows, as the specimen starts to delaminate, the delamination front does not stay in the mid-plane across the whole width of the specimen all the time. In parts of the width, the delamination jumps from one ply interface to another due to material / loading non-linearities or manufacturing defects. This leads to fibers that are part of one leg of the specimen, still being attached to the other leg, forming a bridge between both specimen legs. As the crack length grows, and the distance between the specimen legs grows, these fibers bridging the top and bottom legs of the specimen break, resulting in an artificial 'toughening' behavior. This behavior is not accounted for in the calculation of the critical fracture toughness (Compliance calibration accounts for the compliance of the whole specimen, regardless of the existence, or lack thereof, of fiber bridging or any other failure mechanism). Fiber bridging is also not modeled in the FEM model either. This is the cause of the growing difference between the experimentally observed results and those of the FEA models for larger crack lengths.

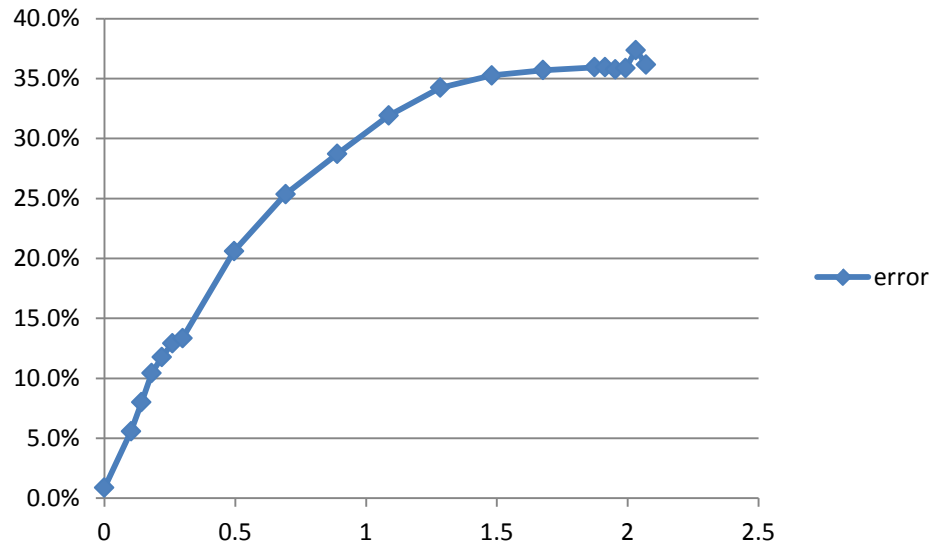


Figure 7-23 percent error between FEM and CC

Vertical Finite Element Model

Two finite models were created to model the vertical DCB. One with a straight crack front, and another using the observed curved crack front. Both models share the same geometry and mesh. To address the issues concerning mesh orthogonality and the accuracy in calculating SERR for cracks that intersect the free edge [23], [89], a newly developed, decaying-orthogonal meshing technique is used to model the curved crack front.

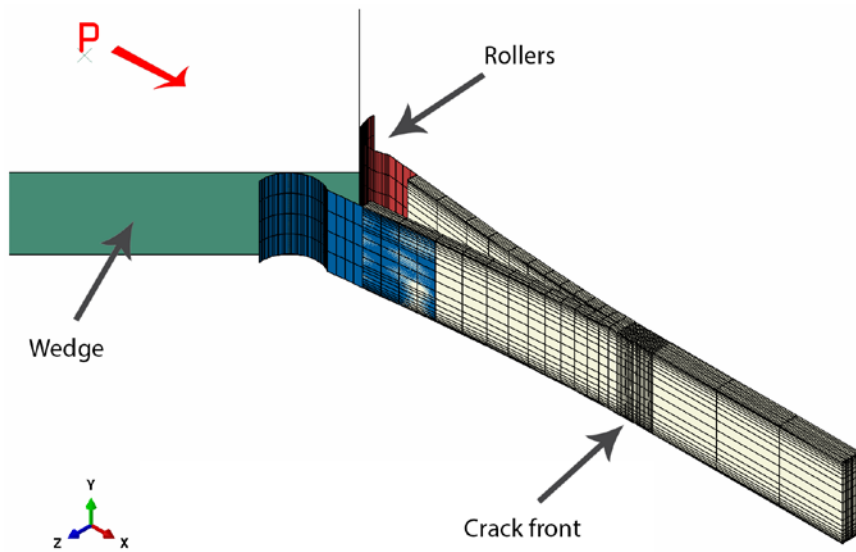


Figure 7-24 Vertical FEM model, straight crack front.

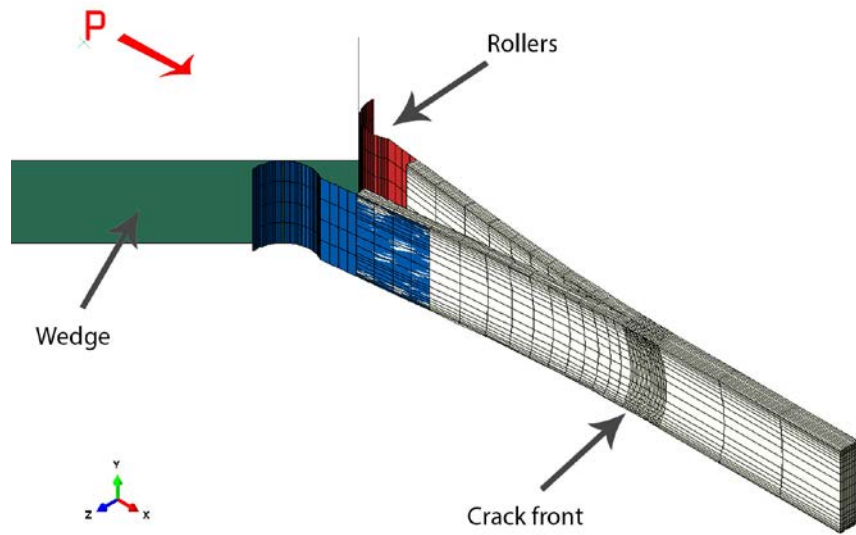


Figure 7-25 Vertical FEM model, curved crack front.

Model Parts and Geometry

The model had three different parts. The wedge, two identical roller supports and the DCB specimen itself. The wedge was modeled as an analytical rigid surface attached to a reference point. To which displacement boundary conditions were prescribed to model machine cross-head downward movement. The specimen roller block supports were modeled as very stiff deformable bodies with 0.1 inch section thickness and a stiffness of 10^9 psi. The contact between the wedge and the rollers was modeled as a frictionless surface-to-surface interaction. The supports were attached to the specimen hinge section (0.75 inches) using a surface-to-surface tie constraints.

The DCB specimen is similar to the one used for the horizontal DCB. It is a merged mesh from two orphaned mesh parts, with the cracked surface not merged together, thus forming the double nodes at each nodal point on the crack surface. The length of the specimen was the total length of the whole specimen (5.25 inches). Boundary conditions were prescribed at the bottom of the specimen to allow for edge small translations and rotations, similar to the experimental setup bottom wedge.

Loading

Because of the known convergence issues that will arise if loading boundary conditions were prescribed at the wedge due to the frictionless interaction used between the wedge and the rollers. A displacement boundary condition was prescribed instead, but since loading boundary conditions were used for the horizontal model, and for consistency purposes, the fracture toughness was calculated at the point where the reaction force on the wedge became equal to the load that was reported by the test machine for this specific crack length. Because of time and processing limitations, this was accomplished using two steps. One for 75% of the prescribed displacement, with a maximum increment size of 0.2 seconds, and total time of 0.75 s. And a second step with

maximum increment size of 0.005 seconds and a total time of 0.25 s. This insured that an increment that is reasonably close to the specimen failure load, for that crack length, will be found using reasonable accuracy, and without resorting to interpolation between output time increments. This usually resulted in an error in load measurement of less than 1%.

Mesh

The block supports were meshed using a fine mesh for the round section that represents the roller bearings, and a coarser mesh for the width of the roller as shown above. This is because it was found that the calculated SERR is somewhat dependent on the level of refinement of the mesh of the roller surface. The fine mesh chosen yields converged results. The DCB specimen was meshed using the same mesh developed earlier for the horizontal DCB model. It has the same four meshing sections with the same seeding numbers / element sizes.

Table 7-7 Vertical FEM Rollers Mesh

Region	Size / Number
Width	4
Length (Fine Mesh Region)	40

Curved Crack fronts

The VCCT method and the associated SERR calculations are developed with the assumption that an orthogonal mesh normal to the crack front is used [23]. However, for curved crack fronts, if an orthogonal mesh cannot be utilized [23], then a methodology like the one proposed by Smith et al [90] can be used. Where the area (for VCCT calculations) is calculated based on a virtual orthogonal mesh instead of the non-

orthogonal (general) mesh would yield reasonable results that are in good agreement (within 3%) of those resulting from orthogonal meshes. However, as stated by Smith, their methodology does not yield correct results towards the specimen edges, that could be because they still used the non-orthogonal mesh for force and displacement calculations, or the special situation where they cannot generate the virtual orthogonal mesh at the specimen free edge. For the current work, a special orthogonal mesh approach was adopted in order to investigate mode mixity around the curved crack front.

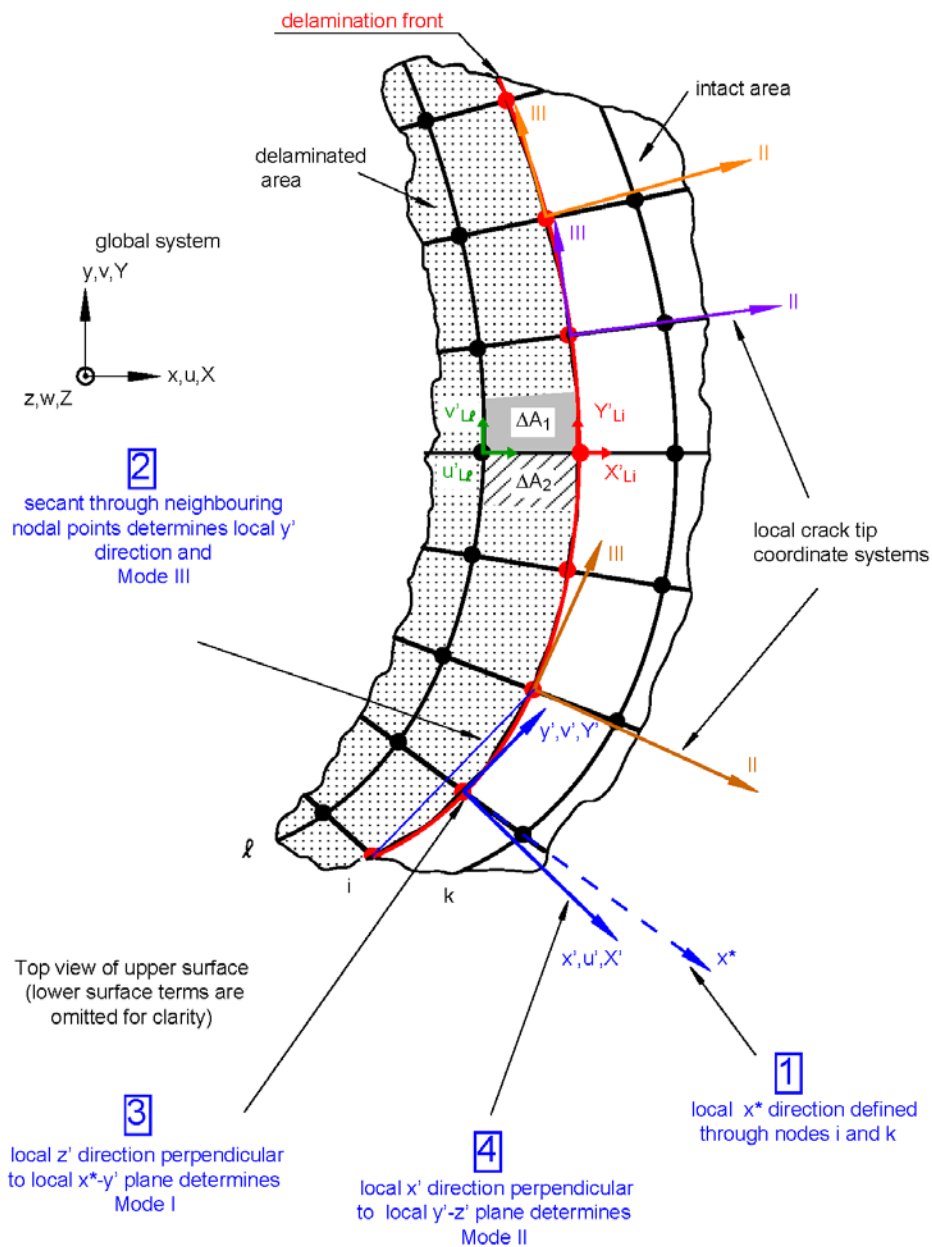


Figure 7-26 Forces and displacements for Orthogonal mesh around crack front [23]

To create the orthogonal mesh around the crack front, a two-fold morphing procedure was used. First, the elements around the crack are morphed in the length direction (x-direction), to model the curved crack front using a linear weight function that decays after the crack front fine region (region II), as the nodes approach the ends of the specimen length. That ensures that the crack front and the adjacent nodes have the same curvature observed from the CT scan. This is shown in the figure below.

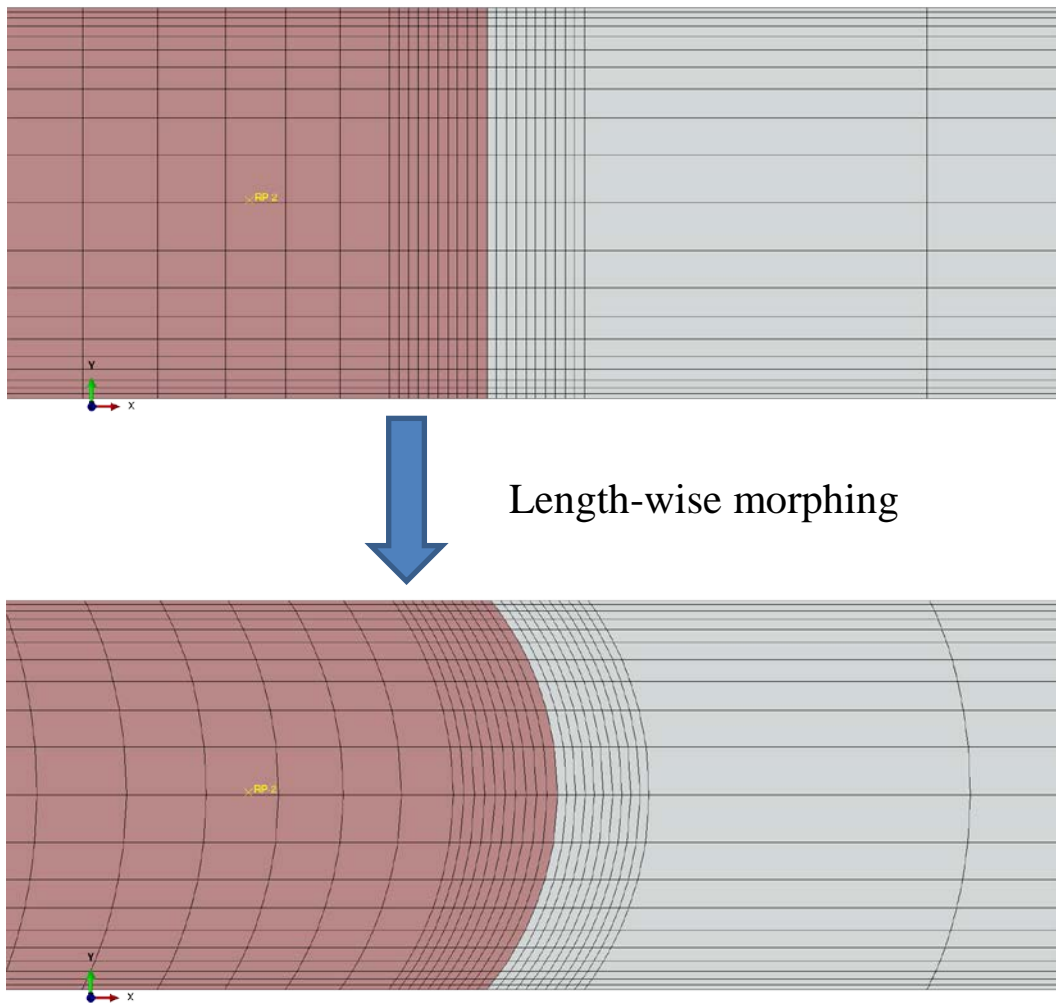


Figure 7-27 Length-wise morphing process

A secondary morph function morphs the nodes in the width direction, effectively rotating the crack front element edges to make them orthogonal to the crack front. This was achieved by re-projecting the y-coordinate of the nodes (width dimension) before and after the crack front onto the lines that connect the arc center to the corresponding node on the crack front. This secondary morph decays using an n^{th} order polynomial proportional to the distance from the specimen free edges. The function used is $\{1-x^n\}$ Where X is the original location of the node in the width direction in percentage. A percentage of 0 would be in the middle of the specimen, and that of 1 would be the node at the edge. This function evaluates to unity in the middle, and decays to zero as it gets close to the edge. This morph also decays as the node gets further away from the crack front edge using a linear decay function. The non-orthogonal mesh and the 'orthogonalized' mesh using a 20^{th} order polynomial are shown in Figure 7-28.

Both decay methods are implemented in order to avoid having zero volume elements or excessively deformed elements at the edges of the specimen after the mesh morph process. However, this will lead to the elements towards the edge of the specimen not being perfectly orthogonal because of the decaying functions. To investigate the effect of the level of orthogonality (the order of polynomial to be used) on the resulting SERR across the specimen width, several polynomial orders were implemented, and the SERR across the specimen width is recorded. Figure 7-30 below shows a plot of the different polynomial orders and their response for one half of the specimen width. From the figure, as the polynomial order increases, the section of the crack front elements being orthogonal to the crack increases by the factor obtained from the nonlinear function. For instance, for a 6^{th} order polynomial decay function, starting from the center of the width of the specimen and making our way towards the edge, 46% of the elements

across the width (0.184 in) would remain 99% orthogonal to the crack front, then it decays non-linearly from there, reaching 0 at the edge. But for a 14th order polynomial function, 71% of the elements across the width (0.284 in) would remain 99% orthogonal to the crack front. This shows that as the order of the polynomial increases, the percent of elements, starting from the middle, that are orthogonal to the crack front increases. Also the remaining elements will have a higher, or lower orthogonality percentage based on the polynomial order.

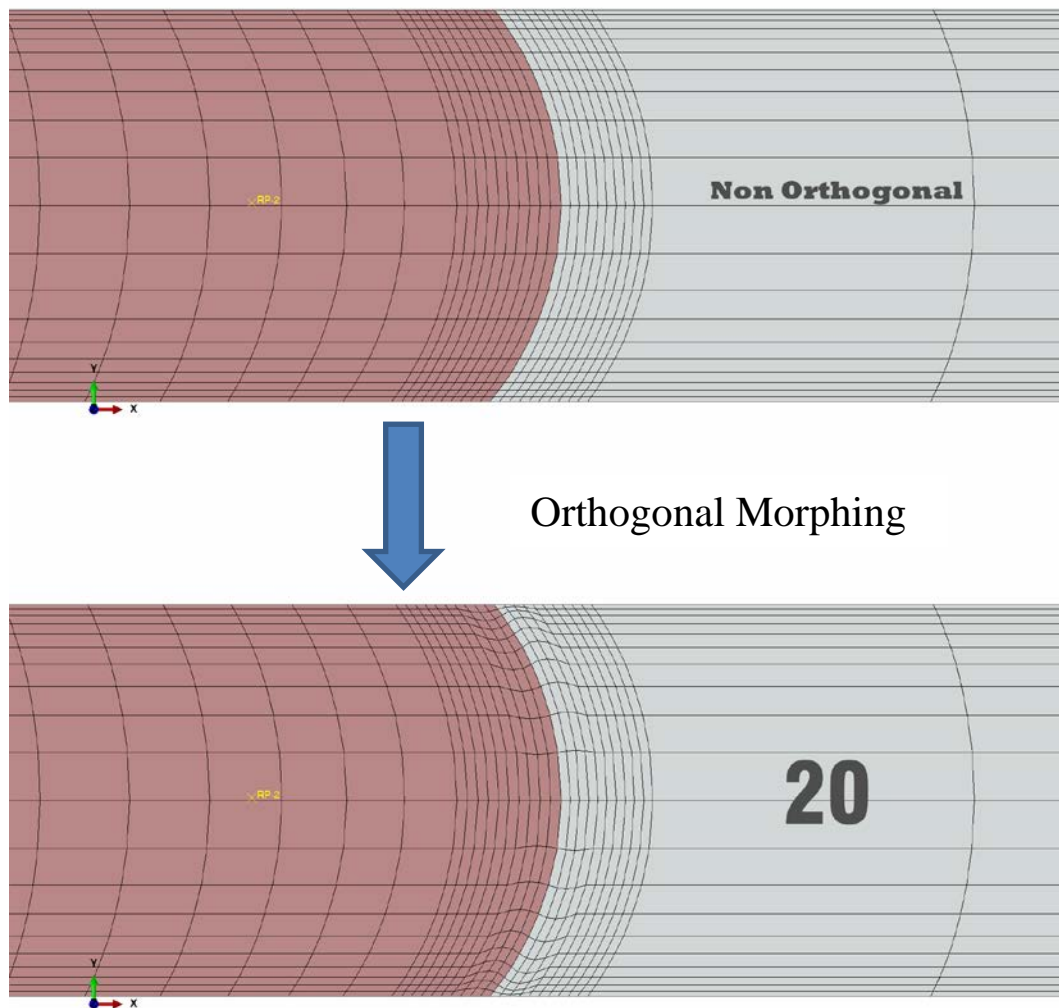


Figure 7-28 Orthogonal morphing using a 20th order polynomial

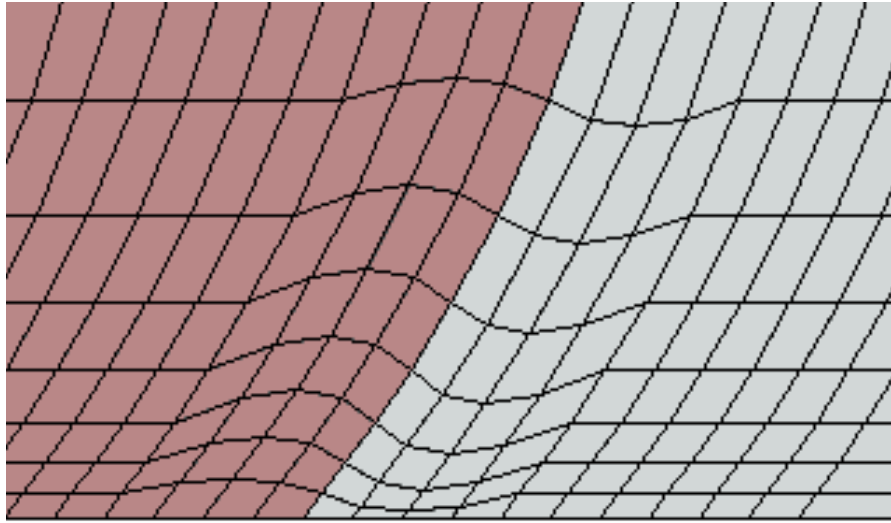


Figure 7-29 Close-up on the morphed elements close to the specimen edge

Because of the use of the orthogonal mesh, the forces and areas had to be calculated based on the new mesh. Also, forces had to be calculated for the local coordinates instead of the global ones in order to generate accurate SERR values. For this, a node set representing the normal vector for each node was created in pre-processing. Then in post processing, the projections of these vectors on the global unit vectors were calculated, and a rotation matrix was formulated in order to calculate the new force values in the local coordinate system from those provided by Abaqus (in the global coordinate system). These transformations do not affect the forces used to calculate the G_I fracture toughness, but the tangential shear forces used in the calculation of mode II and mode III contributions are affected. However, their values were in the order of 10^{-14} and are assumed negligible.

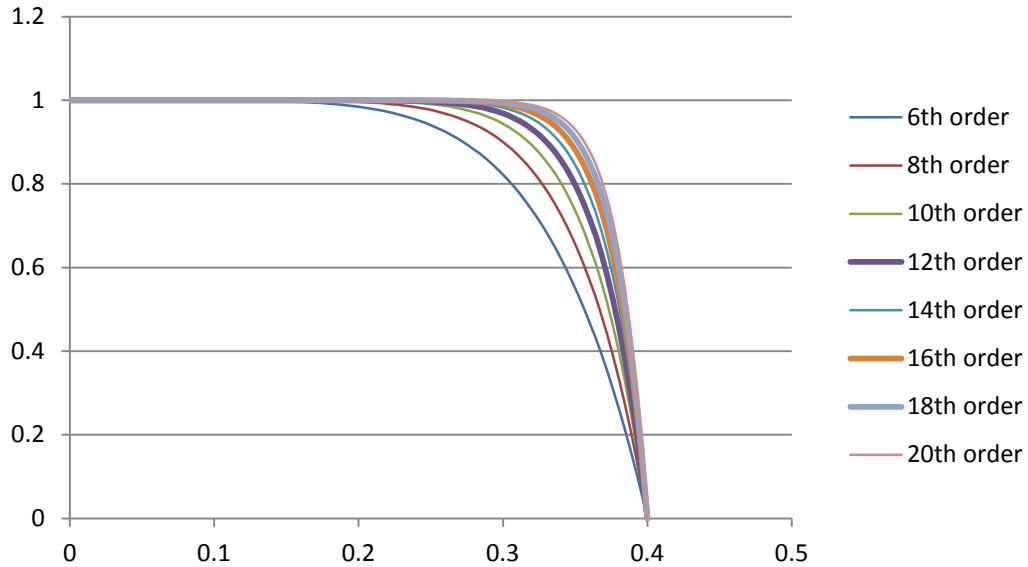


Figure 7-30 Polynomial decay function for orthogonal mesh

In order to determine the appropriate polynomial order for use in this work, a study of the effect of the different orders of polynomial on the SERR across the specimen width was conducted. It was found that regardless of the polynomial order, the contribution from both Mode II and Mode III fracture modes was negligible (in the order of 10^{-14} or less). This is expected due to symmetry of the DCB specimen and the prescribed transverse loading conditions resulting in a predominantly mode I delamination. Figure 7-31 shows the Mode I SERR distribution across the specimen width for a curved crack front for different levels of orthogonality, ranging from 6th order polynomial and going up to a 20th order one. As shown, the values of the SERR agree for all the nodes and for all the polynomial orders, only the nodes associated with the last element (last two nodes) show some difference. However, since the last element is only 0.009 in thick (0.2 mm), and since we already know that the values of the forces at the crack-front / free edge interface are not reliable, this result is accepted.

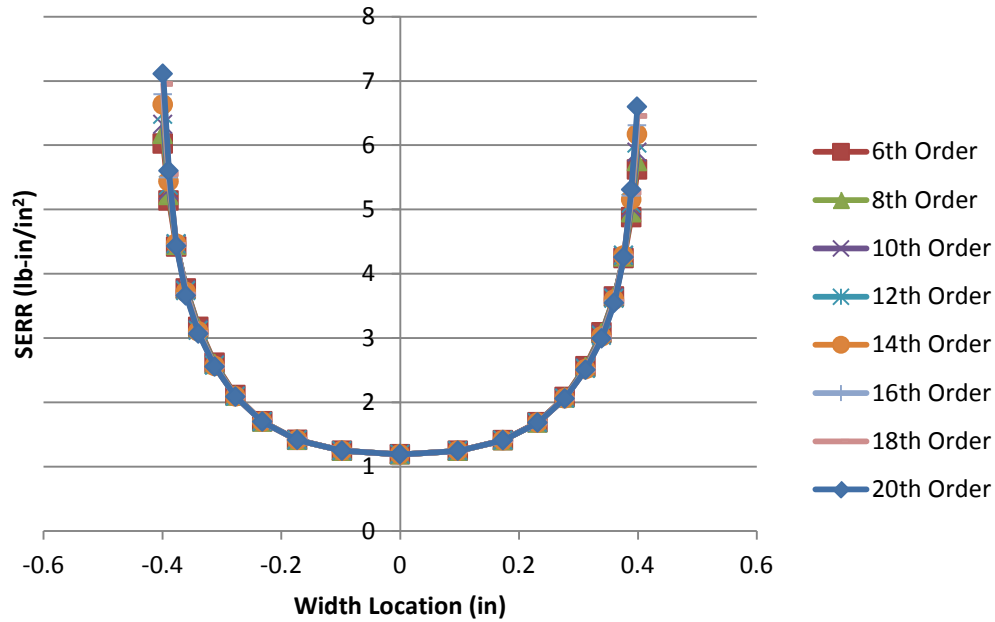


Figure 7-31 SERR for a curved crack front using different levels of orthogonality

For all the elements other than the last ones on the edges of the specimen, it is clear that the level of mesh orthogonality does not have much effect on the values of the SERR for mode I. For instance, the third node from either edge has almost identical SERR value for all polynomial orders, yet the level of orthogonality for the 6th order polynomial is 31% for this node, but 70% for the 20th order one. This seems to be because, for such small elements towards the edge of the specimen, the change in element area due to orthogonality does not seem to be large enough to result in a noticeable change in the calculated SERR around these elements. All other nodes throughout the crack front had a very good correlation, with a maximum difference of 3% between the 6th order and that of the 20th. For this work, a polynomial order of 14 was chosen for its higher accuracy, yet requiring reasonable processing time.

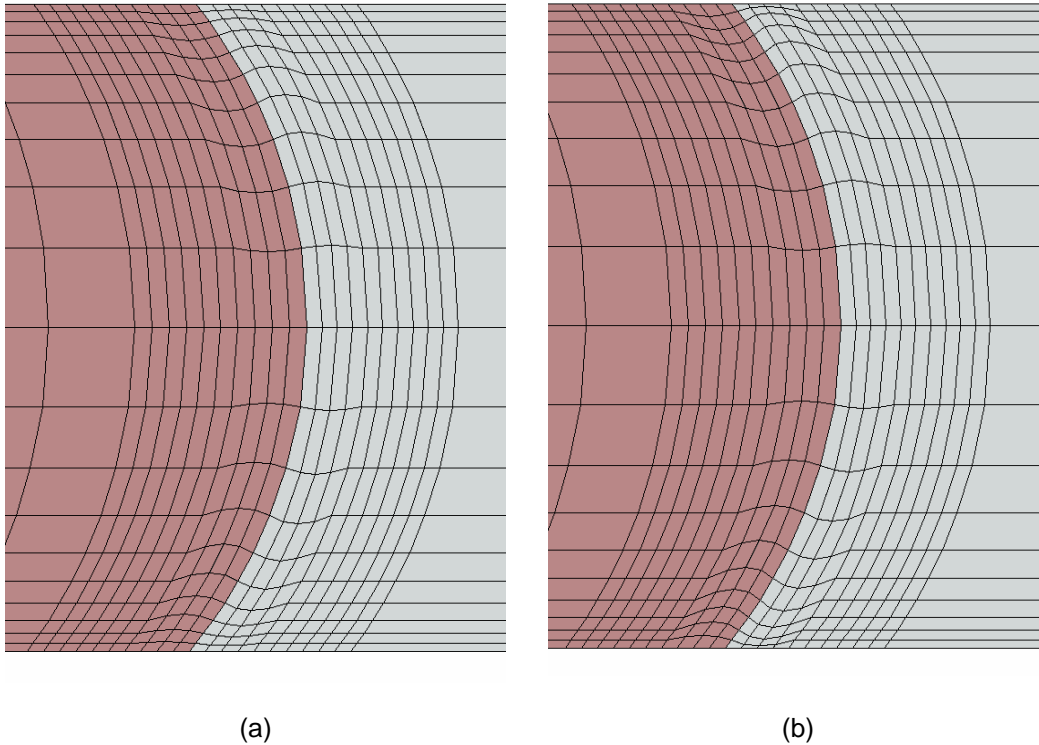


Figure 7-32 Comparison between (a) morphed mesh with 6th order polynomial, and (b) morphed mesh with 20th order polynomial

For comparison purposes, the results of the new 'orthogonalization' approach were compared to those calculated using the virtual orthogonal mesh developed by Smith and Raju [90]. The curved, non-orthogonal mesh was used, the areas for VCCT calculations were calculated as outlined in their work, and the SERR across the specimen width was calculated. Figure 7-33 Shows a plot of the SERR across the specimen width for both methods. The elements at the edge of the specimen were excluded from this calculation since Smith and Raju showed that their method does not yield correct results close to the crack-front / free surface interface. And also since the new method developed here did not yield correct results for the final elements either.

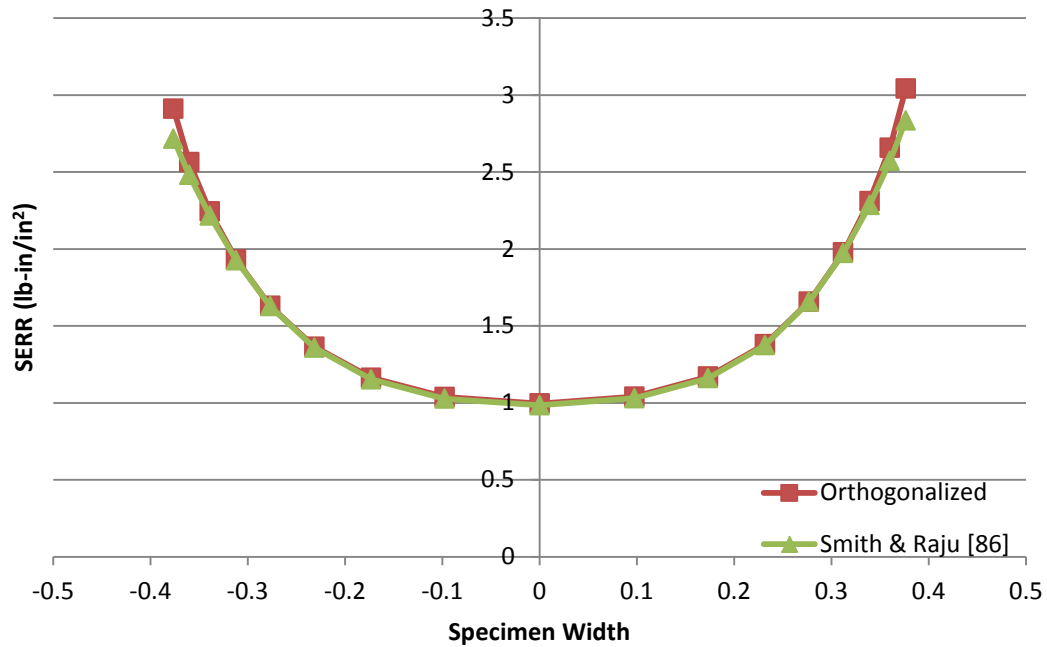


Figure 7-33 Orthogonalized Mesh vs Smith and Raju Method for pre-crack region

As shown, both methods show decent agreement in the middle section of the specimen. However, Smith method does start to deviate as we get closer to the specimen edges. This is in line with the conclusion of his work as well as figures 22 and 29 in [90], where the calculation by Smith starts deviating from those values obtained from an orthogonal mesh as we get closer to the edge of the specimen.

Straight vs Curved Crack Fronts

After modeling both the straight and curved crack fronts, the results were compared to observe the difference in mode I SERR distribution, if any, between both crack front shapes. First, the evolve from the straight crack front to the curved was investigated by applying a gain factor to the crack-front curve. We start from the straight

crack front observed experimentally using the high-definition camera system. Then, gradually, we morph that straight crack front to the measured curved shape obtained from the CT scan for the same crack length step. This is achieved by applying a weighting factor to the overall crack front shape. That weighting factor starts at zero (straight crack front) and grows to 1 (100% curved crack front) using a step of 0.11, resulting in 10 steps in total. The SERR across the specimen width is recorded during each of those steps and plotted against the normalized width in Figure X.

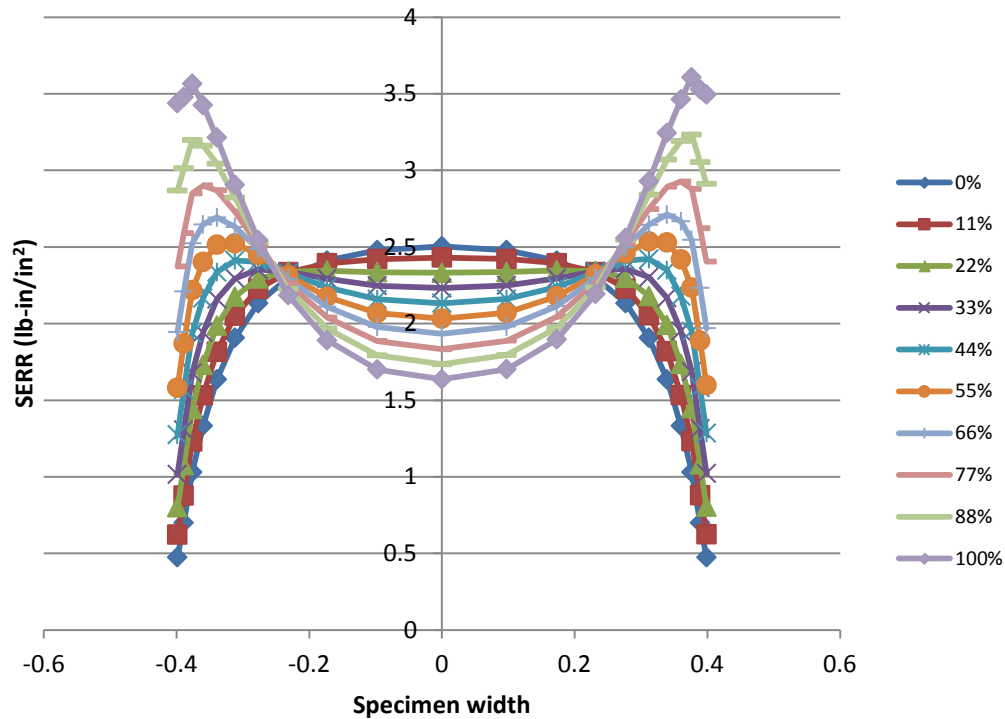


Figure 7-34 The effect of the curved crack front on the SERR distribution across the specimen width for a 5mm crack length.

The above figure shows that as the crack front changes its shape from the straight (assumed) to the curved crack front (observed). The SERR distribution across the specimen width changes dramatically. Curved crack fronts were observed by ultrasonic ex-situ scans or using visual observation after specimen total failure (post mortem) by C.T. Sun [64], Krueger [91], Davidson [63], [69], [92], Budzik [68], Shokrieh [73], [74], and others. However, none of those attempts involved measuring and modeling the actual curved crack front for DCB specimens made from composite materials, either ex-situ or in-situ.

Davidson, Krueger and few others concluded that the curved crack front is a result from the material compensating for the non-uniform SERR distribution across the width of a straight crack front. However, that was never supported by actual measurement and calculation of the SERR across the specimen width for the curved crack front. Budzik, did perform a 'post-mortem' measurement and modeling for the curved crack front in an Isotropic, Single Cantilever Beam (SCB) test. And while his work is not directly comparable to the work performed here, because of the different material selection (Isotropic vs Composite) and the different test type (SCB vs DCB), some of the observed SERR behavior due to the modeling of the actual crack curvatures can be compared.

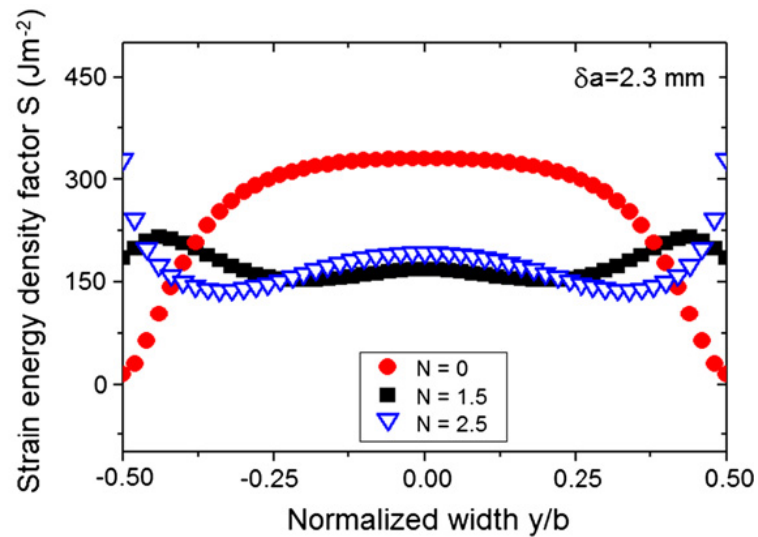


Figure 7-35 Strain energy across specimen width for straight ($N=0$) and curved crack front ($N=1.5$) by Budzik et al [68]

As shown in Figure 7-34, Budzik reported that going from the straight crack front to the curved one, changed the SEDF (strain Energy Density factor) dropping the section in the middle of the specimen, and raising the edges. The final drop towards the specimen edges could be artificial due to the lack of use of orthogonal mesh for these models (there was no mention of an orthogonal, or special mesh used). Or it could be a result of the mode mixity in the failure of SCB specimens, unlike DCB specimens.

Table 7-8 shows CT scans of different crack progression lengths, and the corresponding SERR distribution across specimen width for both the straight and curved crack fronts for all the crack lengths in a vertical DCB specimen.

Table 7-8 Sample CT scans and FEA results

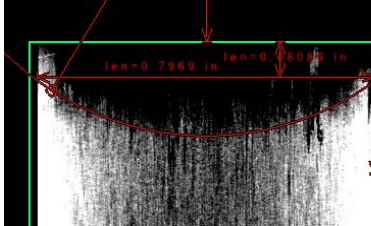
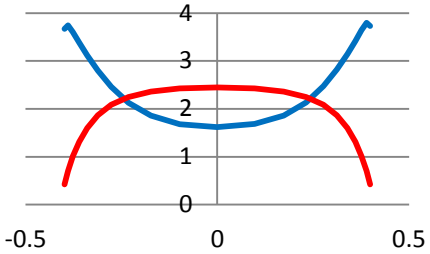
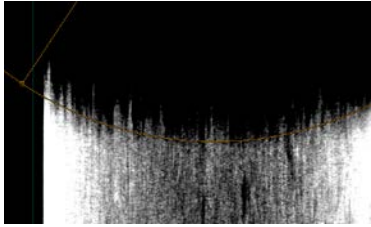
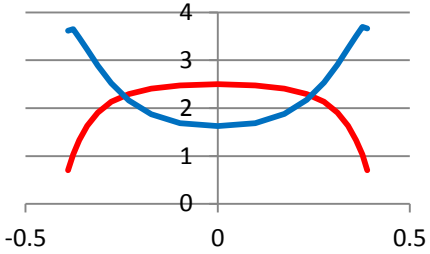
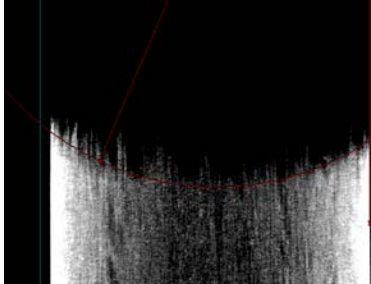
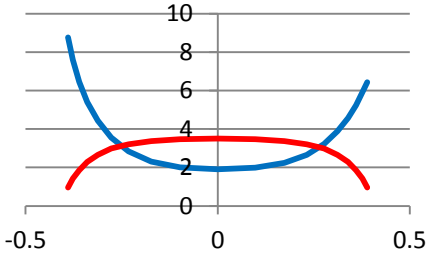
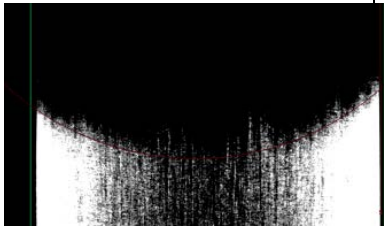
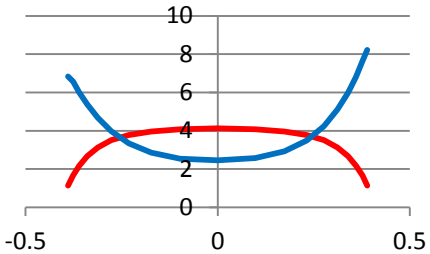
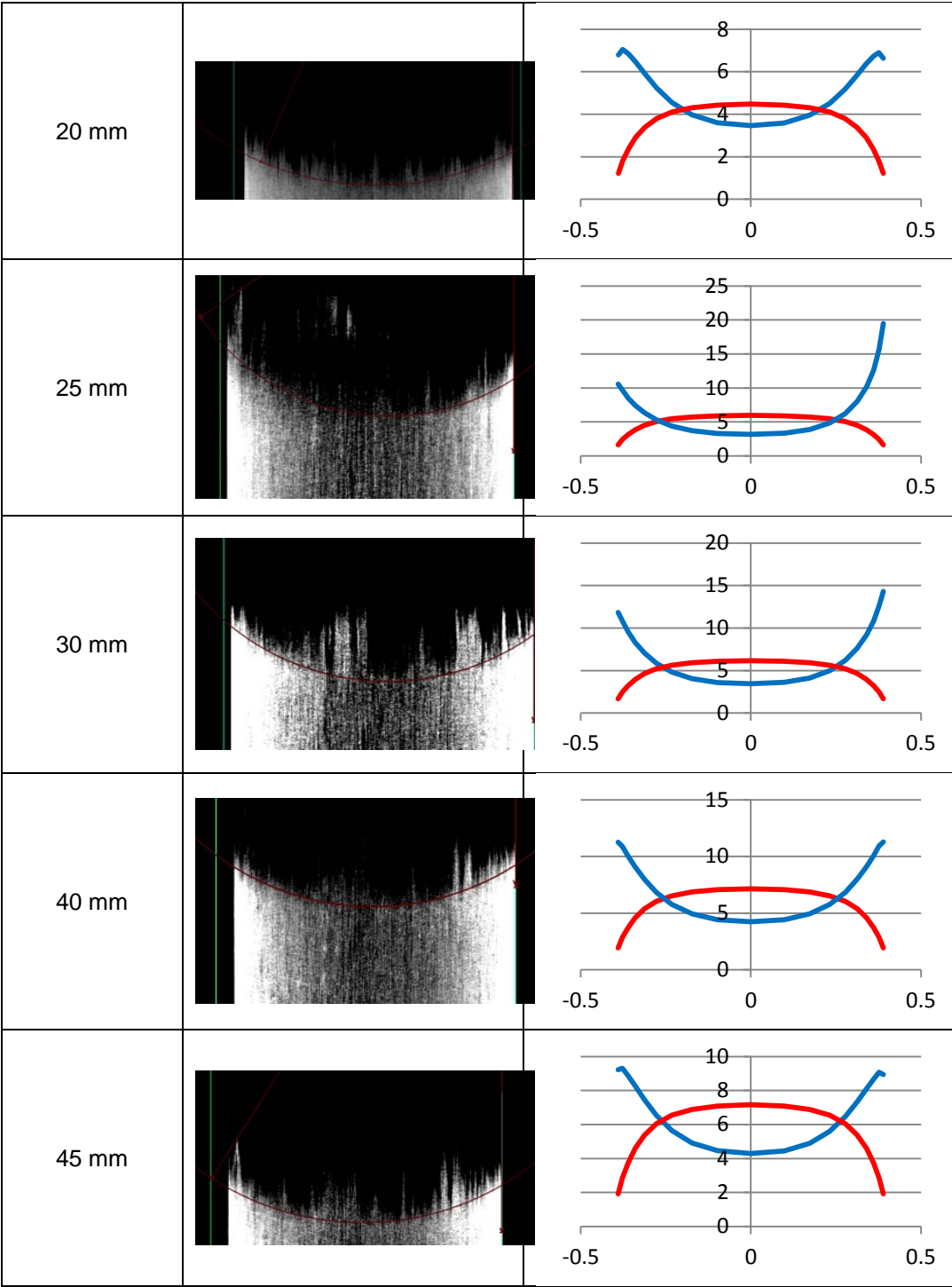
Crack Extension	CT Image	SERR across width
Pre-crack		
5 mm		
10 mm		
15 mm		

Table 7-8 – Continued



Chapter 8

Conclusions and Recommendations for Future Work

Conclusion

A system for computed tomography (CT) scanning, in-situ mechanical testing for standard (full) size specimens used in characterization of stiffness, strength, and toughness properties of composite materials was developed. The system is designed, built and validated using ASTM standards. The capabilities of the new system are discussed and compared to those of existing systems. The system parts as well as the different configurations are described in detail including the advantages and disadvantages of each configuration.

The developed system was then used to investigate damage in various composite structures demonstrating better damage detection and the ability to observe the progress of damage in the specimen while loading. The system was used to validate newly developed numerical models that predict failure mechanisms for notched (open hole) compression specimens. As well as in on-going research that investigates mode-mixity in the failure of open hole tension (OHT) specimens.

The system was then used to investigate mode I crack progression in double cantilever beam specimens using a newly designed vertical double cantilever beam fixture. CT scans of the tested vertical DCB specimens were conducted using a technique specifically developed for DCB tests that allows for accurate results in a short scan time. Three dimensional volumes of the scanned specimens were reconstructed from the scanned parts and accurate measurements of the curved crack fronts were conducted.

Finite element based models were developed to investigate the strain energy release rates in the DCB specimens. Three main models were developed. The first was to validate the modeling technique and was used to compare the results to those obtained experimentally for the conventional DCB test. And two more to model the vertical tests for the straight and curved crack fronts. A new meshing technique across the specimen width is used that utilizes variable size elements across the width of the specimen allowing for an equally distributed SERR across the specimen width to better capture the non-linear distribution of SERR across the specimen width.

This model depicting the horizontal DCB experiments showed very good correlation of only 0.9% difference from the experimental results. Two more FEM models are created to model the vertical test. One for the straight crack front and another for the curved crack front observed from the CT scans.

The third model was created to investigate the effect of the curved crack front observed from the CT scans, on the calculated SERR across the specimen width. This third model used a newly developed technique to allow for the use of orthogonal mesh around the curved crack front, without any special or virtual elements being created. This method uses a polynomial mesh morphing function that decays using an n^{th} order polynomial toward the edges of the specimen. This methodology is discussed and validated using several techniques showing that for DCB models where the crack front meets a free surface, orthogonalized mesh can indeed be used.

The decaying orthogonal model was also used to investigate the contribution of mode II and mode III fracture toughness on the overall SERR for DCB specimens. This was found to be negligible and hence the mode I is still the only mode of failure in DCB specimen regardless of whether the crack front is straight or curved. The same model was then used to calculate the SERR for the actual curved crack front and it was found to be significantly different from the one calculated for the straight crack front. And since curved crack fronts for DCB specimens have also been observed by other researchers, this might indicate the need for a more comprehensive work to validate or revise current methods used to test for mode I fracture toughness in materials in general, and composites in specific.

Recommendations for Future Work

In-situ system

There are several recommendations that could improve the performance of the in-situ system. A dedicated alignment fixture could be used to streamline the alignment process of the machine which would simplify assembly, repeatability and maintenance. Also, a wireless load transmitter-receiver system could prove useful in avoiding over-winding the data cables and potentially damaging the cables or the load cell.

As for future work, there are virtually unlimited used for the in-situ system developed in this work. The developed system can be used, along with techniques like Digital volumetric Correlation (DVC), to achieve a better insight in the deformation and failure mechanisms inside any structure, especially composite ones. Also, the system could be used, along with numerical models, to predict -> validate -> monitor fractures and failures in composite structures.

Vertical DCB fixture

The current vertical DCB fixture could be redesigned so that it imposes identical loads on the specimen to those of the conventional (horizontal) DCB tests. A pin jointed car-jack lever mechanism connected using a rod and a tube to the moving cross-head and another, smaller, load cell fixed to the top frame of the machine.

It could then be utilized to have a more comprehensive study on a much larger scale in order to investigate actual fracture modes in some, or all, currently used standard tests. Offering either validations or recommendations on how to have a more practical way to measure different fracture modes for different materials, especially composite ones.

FEM models

Different Fem modeling techniques could be investigated in order to see if any improvement over the newly developed methodology could be achieved. One promising technique could be using 100% orthogonal mesh throughout the crack front by using local-meshing / mesh stitching techniques.

Also, the FEM modeling techniques developed in this work could be utilized to model failure in more complex structures like notched (open hole) specimens.

References

- [1] G. Seon, "Finite Element Based Methodology for Prediction of Matrix-Dominated Failure in Composites.," Ph. D. Thesis, University of Texas at Arlington., 2014.
- [2] B. Djordjevic, "Nondestructive test technology for the composites," ... *Slov. Soc. non-destructive Test.*, pp. 259–265, 2009.
- [3] GREGORY LINKERT, "Nondestructive Testing, Then, Now and in the Future - AviationPros.com," *Website*. [Online]. Available: <http://www.aviationpros.com/article/11281754/nondestructive-testing-then-now-and-in-the-future>. [Accessed: 19-Mar-2014].
- [4] L. Salvo, P. Cloetens, E. Maire, S. Zabler, J. . Blandin, J. . Buffière, W. Ludwig, E. Boller, D. Bellet, and C. Jossierond, "X-ray micro-tomography an attractive characterisation technique in materials science," *Nucl. Instruments Methods Phys. Res. Sect. B Beam Interact. with Mater. Atoms*, vol. 200, pp. 273–286, Jan. 2003.
- [5] "Shanghai Synchrotron Radiation Facility." [Online]. Available: <http://ssrf.sinap.ac.cn/english/1/Introduction.htm>. [Accessed: 13-Apr-2014].
- [6] "The European Synchrotron Radiation Facility in Grenoble, Fr." [Online]. Available: <http://www.esrf.eu/about>. [Accessed: 31-Mar-2014].
- [7] X. Wu and H. Liu, "X-Ray cone-beam phase tomography formulas based on phase-attenuation duality," *Opt. Express*, vol. 13, no. 16, p. 6000, 2005.
- [8] Y. Nikishkov, L. Airoidi, and A. Makeev, "Measurement of voids in composites by X-ray Computed Tomography," *Compos. Sci. Technol.*, vol. 89, pp. 89–97, Dec. 2013.
- [9] "How Computed Tomography works | X-view CT." [Online]. Available: <http://www.xviewct.com/computed-tomography-technology/how-ct-works>. [Accessed: 03-Apr-2014].
- [10] "X5000 Computed Tomography System | X-view CT." [Online]. Available: <http://xviewct.com/industrial-ct-systems/x-view-computed-tomography/m5000-series>. [Accessed: 03-Apr-2014].
- [11] "X-Ray Worx - Reflection Tubes." [Online]. Available: <http://www.x-ray-worx.com/joomla/index.php/en/microfocus-x-ray-tubes-for-non-destructive-material-testing-of-x-ray-worx/types-of-microfocus-x-ray-tubes.html?showall=&start=2>. [Accessed: 03-Apr-2014].

- [12] "The Inverse Square Law, Radiation." [Online]. Available: http://www.cyberphysics.co.uk/general_pages/inverse_square/inverse_square.htm. [Accessed: 03-Apr-2014].
- [13] T. S. Curry, J. E. Dowdey, and R. C. Murry, *Christensen's Physics of Diagnostic Radiology*. Lippincott Williams & Wilkins, 1990.
- [14] "Technical details of microfocus X-ray tubes." [Online]. Available: <http://www.x-ray-worx.com/joomla/index.php/en/microfocus-x-ray-tubes-for-non-destructive-material-testing-of-x-ray-worx/types-of-microfocus-x-ray-tubes.html?showall=1&limitstart=>. [Accessed: 03-Apr-2014].
- [15] W. Chan, "Fracture and Damage Mechanics in Laminated Composites," in *Composites Engineering Handbook*, vol. 4, P. K. Mallick, Ed. CRC Press, 1997, pp. 309–371.
- [16] M. W. Czabaj and J. G. Ratcliffe, "Comparison of intralaminar and interlaminar mode I fracture toughnesses of a unidirectional IM7/8552 carbon/epoxy composite," *Compos. Sci. Technol.*, vol. 89, pp. 15–23, Dec. 2013.
- [17] T. K. O'Brien, "Interlaminar fracture toughness: the long and winding road to standardization," *Compos. Part B Eng.*, vol. 29, no. 1, pp. 57–62, Jan. 1998.
- [18] M. H. Heydari, N. Choupani, and M. Shamel, "Experimental and Numerical Investigation of Mixed-Mode Interlaminar Fracture of Carbon-Polyester Laminated Woven Composite by Using Arcan Set-up," *Appl. Compos. Mater.*, vol. 18, no. 6, pp. 499–511, Aug. 2011.
- [19] A. Griffith, "VI. The Phenomena of Rupture and Flow in Solids.," *Phil. Trans. Roy. Soc. (Lon.) A*, 1920.
- [20] W. Chow and S. Atluri, "Finite element calculation of stress intensity factors for interfacial crack using virtual crack closure integral," *Comput. Mech.*, 1995.
- [21] P. Camanho and C. Dávila, "Mixed-mode decohesion finite elements for the simulation of delamination in composite materials," *NASA-Technical Pap.*, no. June, 2002.
- [22] A. Standard, "D5528-01 2001. Standard Test Method for Mode I Interlaminar Fracture Toughness of Unidirectional Fiber-Reinforced Polymer Matrix Composites," *Am. Soc. Test. Mater.*, vol. 01, no. Reapproved 2007, pp. 1–12, 2010.
- [23] R. Krueger, "Virtual crack closure technique: History, approach, and applications," *Appl. Mech. Rev.*, vol. 57, no. 2, p. 109, 2004.

- [24] R. Krueger and T. O'Brien, "A shell/3D modeling technique for the analysis of delaminated composite laminates," *Compos. Part A Appl. Sci.* ..., no. June, 2001.
- [25] P. Elisa, "Virtual Crack Closure Technique and Finite Element Method for Predicting the Delamination Growth Initiation in Composite Structures," in *Advances in Composite Materials - Analysis of Natural and Man- Made Materials*, 2011, pp. 463–480.
- [26] A. A. User, "11.4.2 Contour integral evaluation Products: Abaqus/Standard Abaqus/CAE," vol. i, pp. 1–11, 2014.
- [27] T. M. Breunig, S. R. Stock, and R. C. Brown, "Simple load frame for in situ computed tomography and X-ray tomographic microscopy," *Mater. Eval.*, vol. 51, no. 5, pp. 596–600, Apr. 1993.
- [28] A. Guvenilir, T. Breunig, J. Kinney, and S. Stock, "Direct observation of crack opening as a function of applied load in the interior of a notched tensile sample of Al-Li 2090," *Acta Materialia*, vol. 45, no. 5. pp. 1977–1987, 1997.
- [29] J. Buffière, E. Maire, and P. Cloetens, "Characterization of internal damage in a MMC p using X-ray synchrotron phase contrast microtomography," *Acta Mater.*, vol. 47, no. 5, pp. 1613–1625, 1999.
- [30] J.-Y. Buffière, H. Proudhon, E. Ferrie, W. Ludwig, E. Maire, and P. Cloetens, "Three dimensional imaging of damage in structural materials using high resolution micro-tomography," *Nucl. Instruments Methods Phys. Res. Sect. B Beam Interact. with Mater. Atoms*, vol. 238, no. 1–4, pp. 75–82, Aug. 2005.
- [31] E. Maire, C. Bordreuil, L. Babout, and J. Boyer, "Damage initiation and growth in metals. Comparison between modelling and tomography experiments," *J. Mech. Phys. Solids*, vol. 53, no. 11, pp. 2411–2434, Nov. 2005.
- [32] H. Van Swygenhoven, B. Schmitt, P. M. Derlet, S. Van Petegem, A. Cervellino, Z. Budrovic, S. Brandstetter, A. Bollhalder, and M. Schild, "Following peak profiles during elastic and plastic deformation: A synchrotron-based technique," *Rev. Sci. Instrum.*, vol. 77, no. 1, p. 013902, Jan. 2006.
- [33] "In-situ mechanical testing during x-ray powder diffraction." [Online]. Available: <http://www.psi.ch/mss/in-situ-x-ray-powder-diffraction>. [Accessed: 14-Apr-2014].
- [34] H. Van Swygenhoven and S. Van Petegem, "In-situ mechanical testing during X-ray diffraction," *Mater. Charact.*, vol. 78, pp. 47–59, Apr. 2013.
- [35] E. Maire, V. Carmona, J. Courbon, and W. Ludwig, "Fast X-ray tomography and acoustic emission study of damage in metals during continuous tensile tests," *Acta Mater.*, vol. 55, no. 20, pp. 6806–6815, Dec. 2007.

- [36] E. Bayraktar, K. Bessri, and C. Bathias, "Deformation behaviour of elastomeric matrix composites under static loading conditions," *Eng. Fract. Mech.*, vol. 75, no. 9, pp. 2695–2706, Jun. 2008.
- [37] A. Germaneau, P. Doumalin, and J.-C. Dupré, "Comparison between X-ray micro-computed tomography and optical scanning tomography for full 3D strain measurement by digital volume correlation," *NDT E Int.*, vol. 41, no. 6, pp. 407–415, Sep. 2008.
- [38] P. a Hulme, S. J. Ferguson, and S. K. Boyd, "Determination of vertebral endplate deformation under load using micro-computed tomography," *J. Biomech.*, vol. 41, no. 1, pp. 78–85, Jan. 2008.
- [39] "Quadrant: ERTACETAL C, POM." [Online]. Available: http://www.quadrantplastics.com/fileadmin/quadrant/documents/QEPP/EU/Product_Data_Sheets_PDF/GEP/Ertacetal_C_PDS_E_04042012.pdf. [Accessed: 10-Apr-2014].
- [40] "XtremeCT : HRpQCT : Systems & Solutions : Scanco Medical: micro CT scanners, image analysis software, microtomography scan services." [Online]. Available: <http://www.scanco.ch/en/systems-solutions/clinical-microct/xtremect.html>. [Accessed: 10-Apr-2014].
- [41] E. Maire, O. Bouaziz, M. Di Michiel, and C. Verdu, "Initiation and growth of damage in a dual-phase steel observed by X-ray microtomography," *Acta Mater.*, vol. 56, no. 18, pp. 4954–4964, Oct. 2008.
- [42] Y. Barranger, P. Doumalin, J.-C. Dupre, A. Germaneau, S. Hedan, and V. Valle, "Evaluation of three-dimensional and two-dimensional full displacement fields of a single edge notch fracture mechanics specimen, in light of experimental data using X-ray tomography," *Eng. Fract. Mech.*, vol. 76, no. 15, pp. 2371–2383, Oct. 2009.
- [43] J.-Y. Buffiere, E. Maire, J. Adrien, J.-P. Masse, and E. Boller, "In Situ Experiments with X ray Tomography: an Attractive Tool for Experimental Mechanics," *Exp. Mech.*, vol. 50, no. 3, pp. 289–305, Jan. 2010.
- [44] W. Hufenbach, R. Böhm, M. Gude, M. Berthel, A. Hornig, S. Ručevskis, and M. Andrich, "A test device for damage characterisation of composites based on in situ computed tomography," *Compos. Sci. Technol.*, vol. 72, no. 12, pp. 1361–1367, Jul. 2012.
- [45] J. Réthoré, N. Limodin, J.-Y. Buffière, S. Roux, and F. Hild, "Three-dimensional Analysis of Fatigue Crack Propagation using X-Ray Tomography, Digital Volume Correlation and Extended Finite Element Simulations," *Procedia IUTAM*, vol. 4, pp. 151–158, Jan. 2012.

- [46] A. E. Scott, I. Sinclair, S. M. Spearing, A. Thionnet, and A. R. Bunsell, "Damage accumulation in a carbon/epoxy composite: Comparison between a multiscale model and computed tomography experimental results," *Compos. Part A Appl. Sci. Manuf.*, vol. 43, no. 9, pp. 1514–1522, Sep. 2012.
- [47] A. E. Scott, M. Mavrogordato, P. Wright, I. Sinclair, and S. M. Spearing, "In situ fibre fracture measurement in carbon–epoxy laminates using high resolution computed tomography," *Compos. Sci. Technol.*, vol. 71, no. 12, pp. 1471–1477, Aug. 2011.
- [48] H. a Bale, A. Haboub, A. a MacDowell, J. R. Nasiatka, D. Y. Parkinson, B. N. Cox, D. B. Marshall, and R. O. Ritchie, "Real-time quantitative imaging of failure events in materials under load at temperatures above 1,600 °C.," *Nat. Mater.*, vol. 12, no. 1, pp. 40–6, Jan. 2013.
- [49] D. Fabrègue, C. Landron, O. Bouaziz, and E. Maire, "Damage evolution in TWIP and standard austenitic steel by means of 3D X ray tomography," *Mater. Sci. Eng. A*, vol. 579, pp. 92–98, Sep. 2013.
- [50] A. Hosokawa, D. S. Wilkinson, J. Kang, and E. Maire, "Onset of void coalescence in uniaxial tension studied by continuous X-ray tomography," *Acta Mater.*, vol. 61, no. 4, pp. 1021–1036, Feb. 2013.
- [51] C. Landron, O. Bouaziz, E. Maire, and J. Adrien, "Experimental investigation of void coalescence in a dual phase steel using X-ray tomography," *Acta Mater.*, vol. 61, no. 18, pp. 6821–6829, Oct. 2013.
- [52] F. Bron, J. Besson, and A. Pineau, "Ductile rupture in thin sheets of two grades of 2024 aluminum alloy," *Mater. Sci. Eng. A*, vol. 380, no. 1–2, pp. 356–364, Aug. 2004.
- [53] J. J. Williams, K. E. Yazzie, E. Padilla, N. Chawla, X. Xiao, and F. De Carlo, "Understanding fatigue crack growth in aluminum alloys by in situ X-ray synchrotron tomography," *Int. J. Fatigue*, vol. 57, pp. 79–85, Dec. 2013.
- [54] X. Hu, L. Wang, F. Xu, T. Xiao, and Z. Zhang, "In situ observations of fractures in short carbon fiber/epoxy composites," *Carbon N. Y.*, vol. 67, pp. 368–376, Feb. 2014.
- [55] J. Lachambre, J. Réthoré, A. Weck, and J.-Y. Buffiere, "Extraction of stress intensity factors for 3D small fatigue cracks using digital volume correlation and x-ray tomography," *Int. J. Fatigue*, Apr. 2014.
- [56] J. Lachambre, A. Weck, and J. Réthoré, "3D Analysis of a Fatigue Crack in Cast Iron Using Digital Volume Correlation of X-ray Tomographic Images," *Imaging Methods ...*, 2013.

- [57] "BAM Federal Institute for Materials Research and Testing." [Online]. Available: <http://www.bam.de/en/index.htm>. [Accessed: 15-Apr-2014].
- [58] "BAM | Fatigue testing, failure analysis, damage mechanics." [Online]. Available: http://www.bam.de/en/kompetenzen/fachabteilungen/abteilung_5/fg53/fb53_betriebsfestigkeit.htm. [Accessed: 14-Apr-2014].
- [59] "CT5000 5KN in-situ tensile stage for μ XCT applications | Deben UK – the microscopy accessory experts." [Online]. Available: <http://deben.co.uk/products/mxct-in-situ-holders-testing-stages/tensile-stages-for-x-ray-ct-tomography/>. [Accessed: 13-Apr-2014].
- [60] F. Cowlard and J. Lewis, "Vitreous carbon—a new form of carbon," *J. Mater. Sci.*, 1967.
- [61] Instron, "Instron: 5940 Series Specifications." [Online]. Available: <http://www.instron.us/wa/library/streamFile2.aspx?sdoc=1226>.
- [62] "INSTRON : 5960 Series, Dual Column Tabletop Test Machine." [Online]. Available: file:///C:/Users/Michael/Downloads/POD_5960SeriesDualColumnTabletop_rev6_0113.pdf. [Accessed: 16-Apr-2014].
- [63] B. Davidson, "Two new techniques for predicting delamination growth in laminated plates," 1988.
- [64] C. T. Sun and S. Zheng, "Delamination characteristics of double-cantilever beam and end-notched flexure composite specimens," *Compos. Sci. Technol.*, vol. 56, no. 4, pp. 451–459, Jan. 1996.
- [65] J. Schön, T. Nyman, A. Blom, and H. Ansell, "A numerical and experimental investigation of delamination behaviour in the DCB specimen," *Compos. Sci. Technol.*, vol. 60, no. 2, pp. 173–184, Feb. 2000.
- [66] B. D. Davidson and R. a. Schapery, "Effect of Finite Width on Deflection and Energy Release Rate of an Orthotropic Double Cantilever Specimen," *J. Compos. Mater.*, vol. 22, no. 7, pp. 640–656, Jan. 1988.
- [67] R. Krüger, "Three dimensional finite element analysis of multidirectional composite DCB, SLB and ENF specimens," *Inst. Statics Dyn. Aerosp. ...*, no. 94, 1994.
- [68] M. K. Budzik, J. Jumel, and M. E. R. Shanahan, "On the crack front curvature in bonded joints," *Theor. Appl. Fract. Mech.*, vol. 59, no. 1, pp. 8–20, Jun. 2012.

- [69] B. D. Davidson, R. Krüger, and M. König, "Effect of stacking sequence on energy release rate distributions in multidirectional dcb and enf specimens," *Eng. Fract. Mech.*, vol. 55, no. 4, pp. 557–569, Nov. 1996.
- [70] A. C. Orifici and R. Krueger, "Benchmark assessment of automated delamination propagation capabilities in finite element codes for static loading," *Finite Elem. Anal. Des.*, vol. 54, pp. 28–36, Jul. 2012.
- [71] J. Andersons and M. König, "Dependence of fracture toughness of composite laminates on interface ply orientations and delamination growth direction," *Compos. Sci. Technol.*, vol. 64, no. 13–14, pp. 2139–2152, Oct. 2004.
- [72] R. M. Jones, I. Daniel, and O. Ishai, *Mechanics of composite materials*. CRC Press, 1994.
- [73] M. M. Shokrieh, M. Heidari-Rarani, and M. R. Ayatollahi, "Calculation of for a multidirectional composite double cantilever beam on two-parametric elastic foundation," *Aerosp. Sci. Technol.*, vol. 15, no. 7, pp. 534–543, Oct. 2011.
- [74] M. M. Shokrieh, M. Heidari-Rarani, and S. Rahimi, "Influence of curved delamination front on toughness of multidirectional DCB specimens," *Compos. Struct.*, vol. 94, no. 4, pp. 1359–1365, Mar. 2012.
- [75] R. Krueger, M. K. Cvitkovich, T. K. O'Brien, and P. J. Minguet, "Testing and Analysis of Composite Skin/Stringer Debonding under Multi-Axial Loading," *J. Compos. Mater.*, vol. 34, no. 15, pp. 1263–1300, Aug. 2000.
- [76] R. Krueger, "Computational fracture mechanics for composites—State of the art and challenges," *NAFEMS Nord. Semin. Predict. Model. ...*, 2006.
- [77] R. Krueger and D. Goetze, *Influence of finite element software on energy release rates computed using the virtual crack closure technique*. 2006.
- [78] A. Makeev, "A System for Accurate Three Dimensional Material Characterization. Defense University Research Instrumentation Program (DURIP) Proposal to the Office of Naval Research (ONR).," 2011.
- [79] Instron, "Instron: 5960 Series Specifications." [Online]. Available: <http://www.instron.us/wa/library/streamFile2.aspx?sdoc=1225>.
- [80] Kinematics Engineering Manufacturing, "SE9C-61M-24H01-RC Catalog."
- [81] MITSUBISHI ELECTRIC, "Melservo J3 servo motors and controllers." .
- [82] "Interface: 2816 Axial Torsion Load Cell For Force & Torque (Fz & Tz)." [Online]. Available: <http://www.interfaceforce.com/index.php?2816-Axial-Torsion-Load-Cell-Force-and-Torque-Fz-and-Tz&mod=product&show=12>. [Accessed: 24-Apr-2014].

- [83] ASTM International, "ASTM E1012-14, Standard Practice for Verification of Testing Frame and Specimen Alignment Under Tensile and Compressive Axial Force Application," 2014.
- [84] G. Murri, "Effect of embedded piezoelectric sensors on fracture toughness and fatigue resistance of composite laminates under mode I loading," pp. 1–30, 2006.
- [85] and Y. N. Makeev, A., Y. He, B. Shonkwiler, E. Lee, H. Schreier, "A method for measurement of three-dimensional constitutive properties for composite materials," in *Proceedings of the 18th ICCM, Jeju, Rep. Korea*, 2011.
- [86] R. Krueger, "An Approach to Assess Delamination Propagation Simulation Capabilities in Commercial Finite Element Codes," Apr. 2008.
- [87] R. Krueger, "Development and Applications of Benchmark Examples for Static Delamination Propagation Predictions," 2013.
- [88] I. S. Raju and J. C. Newman, "Three dimensional finite-element analysis of finite-thickness fracture specimens," no. May, 1977.
- [89] and I. S. R. Smith, Steven A., "Evaluation of stress-intensity factors using general finite-element models."
- [90] S. A. Smith and I. S. Raju, "Evaluation of Stress-Intensity Factors Using General Finite-Element Models," *ASTM STP 1321*, vol. 29, pp. 176–200, 1998.
- [91] R. Krueger, M. Koenig, and T. Schneider, "Computation of local energy release rates along straight and curved delamination fronts of unidirectionally laminated DCB and ENF-specimens," in *AIAA/ASME/ASCE/AHS/ASC Structures, Structural Dynamics, and Materials Conference, 34th*, 1993, pp. 1332–1342.
- [92] B. D. Davidson, "An Analytical Investigation of Delamination Front Curvature in Double Cantilever Beam Specimens," *J. Compos. Mater.*, vol. 24, no. 11, pp. 1124–1137, Nov. 1990.

Biographical Information

Mr. Tadros has more than a decade in the design and manufacturing industry specializing in multidisciplinary engineering projects. He graduated with a bachelor in 'production and design' in 2004 and held several positions in the industry since then including lead design engineer, production manager, chief quality engineer and chief technology officer. Over the years he designed and helped manufacture a myriad of engineering systems, ranging from industrial production systems to orthopedic tools and bone implants for veterinary use. He also designed several special robotic systems for manufacturing, autonomous locomotion and medical uses, as well as several structural testing systems for exotic materials and special applications. He also has experience in factory planning and the development and implementation of Quality Control / Quality Assurance (QA/QC) routines and processes.